

NASA Technical Paper 1642

# Wind Tunnel Investigation of an All Flush Orifice Air Data System for a Large Subsonic Aircraft

Terry J. Larson, Stuart G. Flechner,  
and Paul M. Siemers III

MAY 1980



NASA Technical Paper 1642

# Wind Tunnel Investigation of an All Flush Orifice Air Data System for a Large Subsonic Aircraft

Terry J. Larson  
*Dryden Flight Research Center  
Edwards, California*

Stuart G. Flechner and Paul M. Siemers III  
*Langley Research Center  
Hampton, Virginia*



National Aeronautics  
and Space Administration

**Scientific and Technical  
Information Office**

1980

WIND TUNNEL INVESTIGATION OF AN ALL FLUSH ORIFICE AIR DATA SYSTEM  
FOR A LARGE SUBSONIC AIRCRAFT

Terry J. Larson  
Dryden Flight Research Center

and

Stuart G. Flechner and Paul M. Siemers III  
Langley Research Center

INTRODUCTION

In the past, the measurement of such air data quantities as stagnation pressure or flow angle has usually involved the use of sensors mounted on booms or probes that protrude from the aircraft. Obviously, the direct measurement of stagnation pressure or measurement of flow angularity with vanes requires the use of such devices. However, mounting sensors in that way has measurement disadvantages: Accuracy may be adversely affected by boom bending and vibration, probe size and geometry, and the flow interference due to the probes themselves.

The structural and thermal loading (ref. 1) that probe- or boom-mounted sensors undergo make them unsuitable for use on the space shuttle orbiter at high supersonic and hypersonic speeds. The same problem was encountered in the design of the X-15 air data system, so the measurement of the flow angles and of stagnation pressure was made with a null-seeking spherical sensor (referred to as a ball nose) that was always aligned with the local flow (refs. 2 to 4). The system being developed to support aerodynamic and aerothermodynamic testing on the space shuttle orbiter (ref. 1) consists of an array of pressure orifices mounted flush with the vehicle's surface and located on the vehicle's nose cap (ref. 5). The configuration of the system described in reference 5 was tested in a wind tunnel with a 0.10 scale model of the space shuttle to investigate its potential at subsonic speeds (refs. 6 and 7).

Because of the accuracy of the resulting data, the desire for more experience with the shuttle entry air data system (SEADS) before orbiter installation, and the inherent advantages of any flush air data system, NASA initiated a program with the twofold purpose of acquiring flight experience with SEADS and of evaluating the usefulness of flush air data systems for conventional subsonic and transonic aircraft. Therefore, an array of pressure ori-

fices was installed in a 0.035 scale model of the KC-135A airplane, and the model was tested in the 8-Foot Transonic Pressure Tunnel at the Langley Research Center. With some additions, including orifices on the sides of the fuselage, the pressure orifice array was similar to that used in SEADS, and it was used to determine stagnation pressure, angle of attack, angle of sideslip, static pressure, and Mach number. The wind tunnel tests covered Mach numbers from 0.30 to 0.90, angles of attack from  $-2^\circ$  to  $16^\circ$ , and angles of sideslip of  $0^\circ$  and  $5^\circ$ . This report presents and analyzes the results of those tests.

## SYMBOLS

$M$	Mach number measured in wind tunnel
$p$	measured local pressure, kPa
$p_{left}$	pressure measured on left surface of nose, kPa
$p_{lower}$	pressure measured on lower surface of nose, kPa
$p_{meas}$	pressure measured on surface of nose between orifices that measure $p_{lower}$ and $p_{upper}$ , kPa
$p_{right}$	pressure measured on right surface of nose, kPa
$p_t$	stagnation pressure measured in wind tunnel, kPa
$p_{upper}$	pressure measured on upper surface of nose, kPa
$p_\infty$	static pressure measured in wind tunnel, kPa
$q$	incompressible dynamic pressure calculated from wind tunnel-measured pressures, kPa
$R$	Reynolds number
$X, Y, Z$	longitudinal, lateral, and vertical model body axes, respectively
$x, y, z$	longitudinal, lateral, and vertical model coordinates, respectively, cm
$\alpha$	angle of attack measured in wind tunnel, deg
$\alpha_{\Delta p_\alpha=0}$	angle of attack at which the differential pressure between two pressure orifices is zero (fig. 12), deg
$\beta$	angle of sideslip measured in wind tunnel, deg

$\Delta p_\alpha$	pressure differential between two orifices in angle of attack plane, kPa
$\Delta p_\beta$	pressure differential between two orifices in angle of sideslip plane, kPa
$\theta$	angular location of pressure orifice, in the plane running vertically through the model's centerline and measured from the horizontal centerline of the model to that radius of a circle with its center at $x = 1.24$ cm, $y = 0$ cm, $z = 0$ cm that intersects the location of the orifice (fig. 4(a)), deg
$\tau_\alpha$	angle of attack parameter, $\frac{p_{lower} - p_{upper}}{(p_{meas} - p_{lower}) + 0.5(p_{lower} - p_{upper})}$
$\tau_\beta$	angle of sideslip parameter, $\frac{p_{right} - p_{left}}{p_6 - p_{right} + 0.5(p_{right} - p_{left})}$
$\phi$	angular location of pressure orifice, in the plane running horizontally through the model's centerline and measured from the vertical centerline of the model to that radius of a circle with its center at $x = 1.42$ cm, $y = 0$ cm, $z = 0$ cm that intersects the location of the orifice (fig. 4(b)), deg

Subscripts:

$a$	angle of attack calculated using orifices 3, 6, and 11
$b$	angle of attack calculated using orifices 3, 6, and 12
$c$	angle of attack calculated using orifices 4, 6, and 11
$d$	angle of attack calculated using orifices 4, 6, and 12
$e$	angle of sideslip calculated using orifices 6, 15, and 16
$f$	angle of sideslip calculated using orifices 6, 14, and 17
$g$	angle of sideslip calculated using orifices 6, 13, and 18
$i, j$	dummy variables
1 to 22	orifice (fig. 3)

## EXPERIMENTAL APPARATUS AND PROCEDURES

### Model Description

The test article was a 0.035 scale model of the KC-135A aircraft. The basic dimensions of the model are presented in figure 1. Figure 2 shows the sting-mounted model in the wind tunnel. This full-span model was equipped with winglets for the investigation of their use on jet transport wings to reduce drag at high subsonic Mach numbers. It was assumed that the effects of the winglets on the pressure measurements of this investigation would be negligible.

The arrangement of the 18 pressure orifices on the model nose and the four orifices on the sides of the fuselage are shown in figure 3. The arrangement of the nose orifices is similar (although not identical) to that of SEADS. That is, the orifices are in a cruciform design, with one row of orifices in the vertical plane of symmetry (that is, in the X-Z plane) and the other row in the horizontal plane of symmetry (the X-Y plane). All the orifices have a diameter of 0.076 centimeter.

The locations of the orifices in the vertical plane of symmetry can be described as being at points where radii emanating from a circle centered at  $x = 1.24$  cm,  $y = 0$  cm, and  $z = 0$  cm intersect the model's surface (fig. 4(a)). The location of each of these orifices can be specified by using an angular measurement,  $\theta$ , defined as shown in figure 4(a). The dashed curve in the figure is an arc of the circle. The model's nose contour closely follows this arc over the region of probable stagnation pressure.

As in the SEADS orifice arrangement, most of the orifices in the vertical plane of symmetry are below the horizontal centerline of the nose. An arrangement of this type is optimum for the determination of stagnation pressure and angle of attack when the prevailing velocity vector intersects the vehicle below the horizontal centerline. Unlike the SEADS design, the arrangement also includes three orifices placed well above the centerline to facilitate the determination of Mach number.

The location of the orifices in the X-Y plane can be described as being like the location of the orifices in the vertical plane of symmetry. Again, the positions of the orifices can be specified by an angular measurement,  $\phi$  in this case (fig. 4(b)). Except for orifice 6, these orifices can be thought of as operating in pairs for the determination of angle of sideslip. Specifically, the orifice pairs are 13, 18; 14, 17; and 15, 16.

Four other pressure orifices were also included in the orifice array. They were in front of the wing on the sides of the fuselage, two on each side, and were used for the measurement of static pressure (fig. 3(b)). The coordinates of these orifices as well as those of the nose orifices are given in figure 3(c). Orifices 19 and 20 are in the same locations as the pitot-static probes used in the air data system of the production KC-135A aircraft. Similarly, orifices 21 and 22 are in the same locations as the flush static pressure orifices used on the production aircraft.

## Test Facility

The model was tested in the Langley 8-Foot Transonic Pressure Tunnel (ref. 8), which is a continuous flow, single-return tunnel with a slotted, rectangular test section. The facility permits the independent variation of Mach number, stagnation pressure, temperature, and dewpoint.

## Test Conditions

Measurements were taken at Mach numbers of 0.30, 0.50, 0.70, 0.78, and 0.90 at model angles of attack ranging from  $-2^\circ$  to  $16^\circ$ , and at angles of sideslip of  $0^\circ$  and  $5^\circ$ . Stagnation temperature was kept at 322 K throughout the tests, and the air was dried until the dewpoint was low enough to prevent condensation effects.

Because the slotted wind tunnel test section is designed to reduce wall effects on lift, no correction was made to the data for these effects. In addition, the wingspan and model frontal area were small enough to make it unnecessary to correct Mach number for wind tunnel blockage (ref. 9). Reynolds number varied from  $5.8 \times 10^6$  per meter to  $9.8 \times 10^6$  per meter. A complete tabulation of the test conditions is given in table 1.

Data were not obtained at the higher angles of attack for Mach numbers of 0.78 and 0.90 because of excessive model vibration. Model vibration increased with both Mach number and angle of attack.

## Accuracy of Measurements

The difference between the local (orifice) and stagnation (tunnel) pressures was measured with an accuracy of  $\pm 0.2$  kPa. Stagnation pressure was measured with an accuracy of  $\pm 0.003$  kPa. The uncertainties in wind tunnel Mach number and dynamic pressure were  $\pm 0.003$  and  $\pm 0.02$  kPa, respectively. The uncertainties in wind tunnel angle of attack and angle of sideslip were  $\pm 0.05^\circ$  and  $\pm 0.1^\circ$ , respectively.

## PRESENTATION OF RESULTS

The basic data from the wind tunnel facility are presented in figures 5 to 10. Figures 5 and 6 show ratios of local pressure to stagnation pressure plotted against angle of attack for  $0^\circ$  and  $5^\circ$  of sideslip, respectively. The local pressures are those measured at nose orifices located in the plane of the model's vertical centerline. The data are presented to evaluate their use for the determination of stagnation pressure and angle of attack. Figures 7 and 8 present a pressure parameter for selected orifices in the same orifice group for the determination of angle of attack at  $0^\circ$  and  $5^\circ$  of sideslip, respectively. Figures 9 and 10 present the static pressure correction for position error plotted against angle of attack for the four fuselage static pressure orifices. The data are again shown at  $0^\circ$  and  $5^\circ$  of sideslip.

After these data were inspected, data orifices favorable to the acquisition of accurate air data were selected and further investigated. The investigation also included an evaluation of sideslip determination using orifices in the horizontal plane of the nose. (Those data are not shown in the preceding figures.) The RESULTS AND DISCUSSION section discusses the results of the investigation and includes additional data figures.

## RESULTS AND DISCUSSION

The data were analyzed to determine whether certain combinations of orifices from the test array could function as complete air data systems for subsonic use. "Complete" means a system that provides all the quantities provided by a conventional pitot-static air data system and, in addition, flow angularity measurements (that is, angle of attack and sideslip). It was made a requirement that the desired air data quantities be derived solely from empirical calibration curves and not be dependent on theoretical or mathematical models. The functional behavior of the curves (for example, the linearity, sensitivity, and consistency of families of curves) was to be used to judge their adequacy for the determination of air data quantities.

In addition, one of the objectives of the analysis was to minimize the number of orifices required to determine the air data quantities. The only exception to this was using two orifices on opposite sides of the fuselage for the determination of static pressure in order to minimize angle of sideslip effects. If several combinations of measurements were acceptable, the optimum combination was to be selected on the basis of functional characteristics, such as the sensitivity of the derived air data quantity to the pressure measurement. The results of the analysis were to be used to decide whether to evaluate the system in a full scale flight program, which would include a comparison of the accuracy of this system with the accuracy of standard air data systems.

A complete description is not given herein of the data reduction methods used to determine air data quantities from the functional relationships that are graphically presented, but one may be found in reference 7.

### Stagnation Pressure

Ratios of measured local pressure to wind tunnel stagnation pressure for orifices in the vertical plane of symmetry are plotted against angle of attack in figure 5 for  $0^\circ$  of sideslip and in figure 6 for  $5^\circ$  of sideslip. In general, increasing sideslip from  $0^\circ$  to  $5^\circ$  decreases the pressure ratio no more than 1 percent.

Measurements from orifices 6, 7, 8, and 9 result in the least variation of pressure ratio with angle of attack and the smallest deviation of the ratio from unity. Hence, these orifices can be calibrated the most accurately for



determining stagnation pressure. Orifices 6 and 7 would be best for measurements at low angles of attack, and orifices 8 and 9 would be best at high angles of attack. The optimum orifice for the entire angle of attack and angle of sideslip ranges is orifice 8. Pressures measured from this orifice are within 3 percent of the stagnation pressure for all Mach numbers. Although this variation is significantly greater than that obtained from a well designed pitot probe (ref. 10), the variation is gradual and consistent with angle of attack, allowing for accurate corrections.

### Angle of Attack

A pressure parameter for the determination of angle of attack is shown in figures 7 and 8 for sideslip angles of  $0^\circ$  and  $5^\circ$ , respectively. This parameter was also used in references 6 and 7. The upper plots present data for orifice pairs in the vertical plane of symmetry, with each pair having orifice 6 in common. The lower figures also present data for orifice pairs in the vertical plane of symmetry, but each pair has orifice 3 in common. Although many other common orifices could have been selected, the matrix provided by those used produces results with both a wide range of sensitivity (slope) and, for some pairs, good linearity.

Although orifice pairs with orifice 3 in common provide pressure parameters that are more sensitive to changes in angle of attack than pairs with orifice 6 in common, the parameters are less linear. The orifice pairs judged to be best for the determination of angle of attack are orifice pairs 6, 11 and 6, 12. These orifices provide both satisfactory linearity, and, as is shown below, adequate sensitivity.

A convenient method for determining angle of attack from the data in figures 7 and 8 is to use equations that define straight lines that are fitted through the data (ref. 11). Figures 11 and 12 show slope and intercept values, respectively, plotted against Mach number for straight lines generated for the data presented in figures 7 and 8 from orifice pairs 6, 11 and 6, 12. If Mach number and dynamic pressure are known, angle of attack is easily attained using these plots. Usually, however, the pressure measurements used to determine Mach number and dynamic pressure are themselves dependent on angle of attack; therefore, an iterative calculation must be used to solve for the three quantities.

The slope values shown in figure 11(a) were taken from the straight lines drawn between the end points of the curves shown in figures 7 and 8. The accuracy of the angle of attack found from the straight lines is affected by the linearity of the actual data curve and by the range of angle of attack for which the slopes were calculated. The slopes were calculated for an angle of attack range of only  $-2^\circ$  to  $8^\circ$  or  $10^\circ$  for Mach numbers of 0.78 and 0.90 (figs. 7(d), 7(e), 8(d), and 8(e)), as opposed to an angle of attack range from  $-2^\circ$  to  $16^\circ$  for Mach numbers from 0.30 to 0.70 (figs. 7(a) to 7(c) and 8(a) to 8(c)). The angle of attack intercepts shown in figure 12 vary with

Mach number because of the asymmetry of the nose in the vertical plane. Of the two orifice pairs, orifice pair 6, 11 produces less variation of the intercept with Mach number.

To determine angle of attack with the desired precision with the  $\Delta p_\alpha/q$  parameter, a certain degree of resolution in the pressure measurement  $\Delta p_\alpha$ , which is dictated by the minimum expected dynamic pressure, must be attained. For example, if orifices 6 and 11 are used, a resolution of 0.01 kPa must be achieved to attain an angle of attack precision of  $0.1^\circ$  over the flight envelope of the KC-135A airplane. Although it is reasonable to assume that this resolution can be achieved, the resolution is significantly more precise than that required to obtain this precision in angle of attack with the YF-12A hemispherical flow direction sensor (ref. 11). This is because the sensitivity of the YF-12A flow direction sensor is approximately 60 percent higher than that of orifice pair 6, 11, as shown in figure 11, and because the YF-12A aircraft is flown at higher dynamic pressures.

The use of a three-orifice pressure parameter designated  $\tau_\alpha$  (which has also been called RAX) was also investigated for angle of attack determination. This parameter, which is discussed in reference 7, requires an additional orifice but does not depend explicitly on dynamic pressure. Four different combinations of orifices in the vertical plane of symmetry were chosen to permit an evaluation of  $\tau_\alpha$ . The resulting parameters, designated  $(\tau_\alpha)_a$ ,  $(\tau_\alpha)_b$ ,  $(\tau_\alpha)_c$ , and  $(\tau_\alpha)_d$ , are plotted against angle of attack for  $0^\circ$  of sideslip in figure 13. The curves of  $(\tau_\alpha)_a$  and  $(\tau_\alpha)_b$  versus angle of attack are much more linear than those for  $(\tau_\alpha)_c$  and  $(\tau_\alpha)_d$ . It can be shown that they also provide ample sensitivity to angle of attack. The variations of  $(\tau_\alpha)_a$  and  $(\tau_\alpha)_b$  with Mach number at a constant angle of attack are shown in figure 14. Variations with Mach number are almost insignificant up to an angle of attack of  $8^\circ$ . Figures 15(a) and 15(b) show that  $(\tau_\alpha)_a$  and  $(\tau_\alpha)_b$  generally exhibit small variations with angle of sideslip. In these figures the variation of  $\tau_\alpha$  with sideslip was assumed to be linear.

It was concluded that both the  $\Delta p_\alpha/q$  parameter and the  $\tau_\alpha$  parameter could be used for the accurate determination of angle of attack for the KC-135A aircraft.

#### Angle of Sideslip

Pressure parameter relationships similar to those evaluated for the determination of angle of attack were evaluated for ascertaining angle of sideslip and are shown in figures 16 to 19. The sideslip parameters were determined by using pairs or triads of orifices located in the horizontal plane of the model nose. Figures 16 and 17 present data using the  $\Delta(\Delta p_\beta/q)/\Delta\beta$  parameter, and figures 18 and 19 present data using  $\tau_\beta$ . The relationships are presented only to indicate the potential of the various combinations of orifices for determining angle of sideslip. To be accurate, relationships to be used for such purposes as calibration curves would have to be based on more than two sideslip angles, especially for  $\tau_\beta$ , which is expected to have nonlinear variations with changes in angle of sideslip, as  $\tau_\alpha$  does with changes in angle of attack.

Figures 16 and 17 present the slopes  $\Delta(\Delta p_\beta/q)/\Delta\beta$  versus angle of attack and Mach number, respectively, assuming a linear relationship between  $0^\circ$  and  $5^\circ$  of sideslip. As expected, the greater the orifice separation, the greater the slope value or pressure sensitivity. For the most part, the sensitivities do not change with changes in angle of attack. The orifices that provide the most consistent set of data and the least variation with changes in angle of attack are orifices 15 and 16. Although the associated pressure sensitivities are smaller than for the other orifice pairs, they are larger than the sensitivities exhibited by orifices 6 and 11 for angle of attack determination. Thus, they are adequate to provide precise sideslip determination.

In figures 18(a), 18(b), and 18(c),  $\tau_\beta$  is shown plotted against angle of sideslip for three sets of orifices. Because there were only two values of sideslip to work with, a linear relationship was assumed in order to evaluate the sensitivity of  $\tau_\beta$  to changes in sideslip. In general, the greater the sensitivity of  $\tau_\beta$  to sideslip, the more it varies with angle of attack. This is somewhat more obvious in figure 19, which shows  $\tau_\beta$  plotted against angle of attack. The most promising  $\tau_\beta$  parameter is considered to be  $(\tau_\beta)_g$ . Although it is the least sensitive of the three  $\tau_\beta$  parameters, its sensitivity is similar to that of  $(\tau_\alpha)_a$  and  $(\tau_\alpha)_b$ , and it is almost constant with changes in angle of attack.

#### Static Pressure

The obvious approach to the measurement of static pressure with an all flush orifice air data system is to utilize the flush orifices at the locations that correspond to the pitot-static probes in the standard air data system. Orifices 19, 20, 21, and 22 (fig. 3(b)) are in such locations.

Corrections to static pressure as a function of angle of attack for the four static pressure orifices are shown in figures 9 and 10 at  $0^\circ$  and  $5^\circ$  of sideslip, respectively. The upper figures present corrections for the individual orifices, and the lower figures present the corrections for the average pressure of orifices 19 and 20 as well as from orifices 21 and 22.

The average pressures from these orifices, which are in diametrically opposed positions on either side of the fuselage, closely approximate the pressures that would result at small angles of sideslip if the pressures from these orifices were manifolded. Manifolding the pressures from such orifices generally results in pressure measurements that are less sensitive to changes in sideslip than the results from individual orifices. Figures 9 and 10 show that this is also true for the subject orifices. The static pressure corrections generally vary less than 2 percent over the angle of attack range for both sets of averaged pressures and at both angles of sideslip. Because of this low sensitivity to changes in angle of attack and the gradual variation of the correction with Mach number, either set of orifices offers an accurately calibratable source for static pressure determination, although the aft set of orifices (orifices 21 and 22) performs slightly better than orifices 19 and 20.

Included in figures 9(b) to 9(e) are flight-determined static pressure corrections corresponding to the position errors for orifices in the same locations as orifices 21 and 22 (ref. 12). The correction at a Mach number of 0.30 (not shown in fig. 9(a)) is essentially zero. These corrections were defined only as a function of Mach number (not angle of attack or sideslip). The discrepancies between the flight-determined corrections for the standard ship system and those derived from the wind tunnel for the all flush orifice system are not excessive, and cause a maximum difference of 0.012 in Mach number when Mach number is derived from the ratio of stagnation pressure to static pressure (see below).

### Mach Number

The previous discussion has shown that various combinations of flush orifices can be used to determine stagnation pressure, static pressure, angle of attack, and angle of sideslip. In general, conventional procedures can be employed for flush orifice systems to determine such air data quantities as Mach number and pressure altitude.

For example, Mach number can be determined by measuring stagnation pressure and static pressure, correcting both for position error, and then using the ratio of the corrected pressures in the well known adiabatic equation that relates the ratio to Mach number. For this method, the best results would be obtained by using orifice 8 to measure stagnation pressure and by averaging the pressures from orifices 21 and 22 to arrive at a measurement for static pressure. The selection of these orifices is based on the previous discussion. However, for flush orifice systems that do not provide pressure measurements that can be considered measurements of stagnation pressure or static pressure, other methods may be more suitable.

One alternative is to determine Mach number through calibration, using the ratio of any two suitable pressures. The suitability of the selected pressures would depend on the behavior of the corresponding pressure ratio when plotted against Mach number (the magnitude, slope, and linearity of the curve) and the insensitivity of the pressure ratio to changes in angle of attack and sideslip. Reference 4 describes the data reduction procedures for both methods.

Figures 20 to 25 show how the appropriate pressure orifice combination might be chosen if Mach number were to be determined using the second method. The figures present pressure ratios for various combinations of pressure orifices at both 0° and 5° of sideslip. In each case, one of the pressures on the nose was used for the higher pressure (which is put in the numerator) and an average of two static pressures was used for the lower pressure (which is put in the denominator). Curves are shown for three angles of attack. The ratios of those pressures are very close to the stagnation-to-static pressure ratio, as shown in figure 20(a), which includes the values of the stagnation-to-static pressure ratio. Hence, the sensitivity of the pressure ratio to Mach number is quite satisfactory. In addition, the curves are quite smooth

and only slightly nonlinear. The major differences in the measurements from the different combinations of orifices are due to angle of attack sensitivity; variations with angle of attack for the various orifice combinations are shown in figures 26 to 31. The combination that varies least with changes in angle of attack is the combination of orifices 7, 19, and 20 (fig. 21). This combination was judged to be the best combination for Mach number determination despite the greater insensitivity of pressure ratios that include pressures from orifices 21 and 22 to changes in sideslip (fig. 27).

An evaluation was also made of the feasibility of using an air data system consisting of flush orifices confined to the nose section. In this evaluation the orifices were confined to those in the vertical plane of symmetry. The results of this evaluation for Mach number determination are presented in figure 32. Compared with pressure ratios that include pressures measured on the fuselage, the pressure ratios for all nose orifices vary considerably with angle of attack. The variations with angle of sideslip, however, are relatively small (figs. 33 and 34). The ratio using orifice 6 has less variation with angle of attack than that using orifice 7. Although the variations are large for both pressure ratios, they are systematic, indicating that they could be used--admittedly with less accuracy than pairs including orifice pairs 19, 20 or 21, 22--for Mach number determination.

#### CONCLUDING REMARKS

A wind tunnel study was made to investigate the feasibility of using an all flush pressure orifice system as a complete subsonic air data system for a conventional aircraft. The study used a 0.035 scale model of the KC-135A airplane (a subsonic cruise aircraft) and covered a Mach number range of 0.30 to 0.90, an angle of attack range of  $-2^{\circ}$  to  $16^{\circ}$ , and angles of sideslip of  $0^{\circ}$  and  $5^{\circ}$ . The orifices were in fixed locations on the forebody and fuselage.

The test data indicated that the system could be used as a complete air data system at subsonic speeds. An optimum system would utilize orifices on the nose of the aircraft in a configuration similar to that described for the measurements necessary to determine stagnation pressure, angle of attack, and angle of sideslip. Flush orifices on the sides of the fuselage at locations corresponding to standard pitot-static system sensors can be used for static pressure measurements. At some sacrifice of accuracy, orifices located only on the aircraft nose can be used as a complete air data system. A full scale flight evaluation of flush orifice systems, including a comparison with the accuracy of conventional pitot-static air data systems, is recommended.

*Dryden Flight Research Center  
National Aeronautics and Space Administration  
Edwards, Calif., July 16, 1979*

## REFERENCES

1. Siemers, Paul M. III: Shuttle Entry Technology Payloads. AAS Paper 75-251, Am. Astronaut. Soc., Aug. 1975.
2. Webb, Lannie D.: Characteristics and Use of X-15 Air-Data Sensors. NASA TN D-4597, 1968.
3. Wolowicz, Chester H.; and Gossett, Terrence D.: Operational and Performance Characteristics of the X-15 Spherical, Hypersonic Flow-Direction Sensor. NASA TN D-3070, 1965.
4. Cary, John P.; and Keener, Earl R.: Flight Evaluation of the X-15 Ball-Nose Flow-Direction Sensor as an Air-Data System. NASA TN D-2923, 1965.
5. Siemers, Paul M. III; and Larson, Terry J.: The Space Shuttle Orbiter and Aerodynamic Testing. AIAA Paper 78-790, Apr. 1978.
6. Larson, Terry J.; and Schweikhard, William G.: Use of the Shuttle Entry Air Data Pressure System at Subsonic Speeds. Proc. 1978 Air Data Systems Conference, May 1978. (Available from Dept. Aeronaut., U.S. Air Force Academy, Colorado Springs, Colo.)
7. Larson, Terry J.; and Siemers, Paul M. III: Use of Nose Cap and Fuselage Pressure Orifices for Determination of Air Data for Space Shuttle Orbiter Below Supersonic Speeds. NASA TP-1643, 1980.
8. Schaefer, William T., Jr.: Characteristics of Major Active Wind Tunnels at the Langley Research Center. NASA TM X-1130, 1965.
9. Brooks, Joseph D.: Some Anomalies Observed in Wind-Tunnel Tests of a Blunt Body at Transonic and Supersonic Speeds. NASA TN D-8237, 1976.
10. Gracey, William: Wind-Tunnel Investigation of a Number of Total-Pressure Tubes at High Angles of Attack. Subsonic, Transonic, and Supersonic Speeds. NACA Rept. 1303, 1957.
11. Montoya, Earl J.: Wind-Tunnel Calibration and Requirements for In-Flight Use of Fixed Hemispherical Head Angle-of-Attack and Angle-of-Sideslip Sensors. NASA TN D-6986, 1973.
12. Yancey, Marion H., Jr.; and Martin, Reese S.: KC-135A Performance Test. AFFTC-TR-58-26, Air Force Flight Test Center, Edwards AFB, July 1958.

TABLE 1.--TEST CONDITIONS

(a)  $\beta = 5^\circ$ 

M	$\alpha$ , deg	$\beta$ , deg	R, per m	$P_t$ , kPa	$P_\infty$ , kPa	q, kPa
.900	-2.14	5.4	$9.80 \times 10^6$	76.16	45.02	25.5
.900	-.11	5.4	9.79	76.16	45.02	25.5
.901	1.96	5.3	9.79	76.15	44.98	25.6
.900	3.88	5.3	9.78	76.12	45.02	25.5
.901	5.96	5.3	9.79	76.15	44.99	25.5
.900	7.95	5.3	9.79	76.16	45.03	25.5
.899	-.07	5.4	9.78	76.14	45.08	25.5
.781	-2.15	5.3	9.18	76.16	50.93	21.7
.780	-.10	5.4	9.17	76.13	50.94	21.7
.779	1.85	5.3	9.17	76.13	50.96	21.7
.780	3.91	5.3	9.18	76.15	50.93	21.7
.780	5.93	5.3	9.17	76.15	50.94	21.7
.780	7.88	5.3	9.17	76.13	50.94	21.7
.780	-.18	5.4	9.18	76.14	50.95	21.7
.700	-2.15	5.3	8.65	76.12	54.87	18.8
.700	-.10	5.3	8.64	76.13	54.87	18.8
.700	1.96	5.3	8.63	76.12	54.86	18.8
.700	3.97	5.3	8.62	76.09	54.88	18.8
.700	5.87	5.2	8.63	76.12	54.87	18.8
.700	7.94	5.2	8.63	76.11	54.87	18.8
.700	9.95	5.2	8.63	76.12	54.87	18.8
.700	11.90	5.2	8.64	76.12	54.87	18.8
.700	13.98	5.1	8.63	76.12	54.88	18.8
.700	15.93	5.1	8.63	76.11	54.86	18.8
.700	-.11	5.3	8.64	76.12	54.87	18.8
.499	-2.14	5.2	9.09	101.49	85.60	14.9
.500	-.10	5.2	9.05	101.51	85.57	15.0
.500	1.94	5.2	9.10	101.53	85.59	15.0
.500	3.90	5.2	9.10	101.52	85.59	15.0
.500	5.95	5.2	9.10	101.54	85.60	15.0
.500	7.94	5.2	9.08	101.50	85.55	15.0
.499	9.91	5.1	9.06	101.45	85.57	14.9
.499	11.93	5.1	9.06	101.45	85.59	14.9
.499	13.96	5.1	9.07	101.47	85.60	14.9
.499	15.98	5.0	9.07	101.47	85.58	14.9
.499	-.12	5.2	9.07	101.46	85.59	14.9
.299	-2.13	5.1	5.84	101.45	95.37	6.0
.298	-.12	5.1	5.83	101.46	95.39	5.9
.298	1.93	5.1	5.83	101.46	95.39	5.9
.298	3.95	5.1	5.82	101.45	95.40	5.9
.298	5.92	5.1	5.82	101.46	95.40	5.9
.298	7.93	5.0	5.81	101.46	95.41	5.9
.296	9.89	5.0	5.81	101.46	95.40	5.9
.298	11.93	5.0	5.81	101.46	95.40	5.9
.298	13.95	4.9	5.81	101.46	95.39	5.9
.298	-.11	5.1	5.80	101.45	95.39	5.9

TABLE 1.--Concluded

(b)  $\beta = 0^\circ$ 

M	$\alpha$ , deg	$\beta$ , deg	R, per m	$p_t$ , kPa	$p_\infty$ , kPa	q, kPa
.901	-2.14	0.0	$9.79 \times 10^6$	76.15	45.00	25.5
.899	-.07	0.0		76.12	45.03	25.5
.900	1.94	0.0		76.12	44.99	25.5
.901	3.89	0.0		76.12	44.98	25.5
.900	5.93	0.0		76.12	45.03	25.5
.900	7.91	0.0		76.13	45.00	25.5
.901	-.17	0.0		76.14	44.95	25.6
.780	-2.12	0.0	9.18	76.14	50.95	21.7
.779	-.09	0.0		76.13	50.97	21.7
.780	1.94	0.0		76.12	50.96	21.7
.780	3.88	0.0		76.12	50.93	21.7
.780	5.88	0.0		76.13	50.92	21.7
.780	7.87	0.0		76.12	50.95	21.7
.780	9.91	0.0		76.13	50.93	21.7
.780	-.09	0.0	9.18	76.13	50.94	21.7
.700	-2.10	0.0	8.65	76.12	54.87	18.8
.700	-.07	0.0		76.13	54.87	18.8
.700	1.90	0.0		76.13	54.87	18.8
.700	3.91	0.0		76.12	54.87	18.8
.700	5.88	0.0		76.12	54.88	18.8
.700	7.90	0.0		76.13	54.87	18.8
.700	9.87	0.0		76.12	54.87	18.8
.700	11.90	0.0	8.64	76.13	54.87	18.8
.702	13.91	0.0	8.64	76.13	54.82	18.9
.700	15.90	0.0	8.63	76.12	54.86	18.8
.700	-.11	0.0	8.64	76.13	54.87	18.8
.500	-2.11	0.0	9.09	101.51	85.58	15.0
.500	-.12	0.0		101.51	85.57	15.0
.500	1.89	0.0		101.53	85.57	15.0
.500	3.90	0.0		101.52	85.58	15.0
.500	5.92	0.0		101.52	85.57	15.0
.500	7.89	0.0		101.51	85.58	15.0
.500	9.85	0.0		101.51	85.56	15.0
.500	11.87	0.0	9.08	101.51	85.59	15.0
.500	13.91	0.0	9.09	101.51	85.57	15.0
.500	15.91	0.0	9.08	101.51	85.58	15.0
.500	-.14	0.0	9.09	101.51	85.57	15.0
.300	-2.14	0.0	5.87	101.52	95.37	6.0
.300	-.13	0.0		101.54	95.39	6.0
.301	1.89	0.0		101.55	95.36	6.0
.300	3.86	0.0		101.55	95.39	6.0
.300	5.88	0.0		101.55	95.40	6.0
.300	7.87	0.0		101.55	95.39	6.0
.300	9.91	0.0		101.55	95.41	6.0
.300	11.88	0.0	5.84	101.54	95.39	6.0
.301	13.88	0.0	5.85	101.54	95.36	6.0
.300	15.91	0.0	5.85	101.52	95.37	6.0
.301	-.12	0.0	5.87	101.55	95.35	6.1



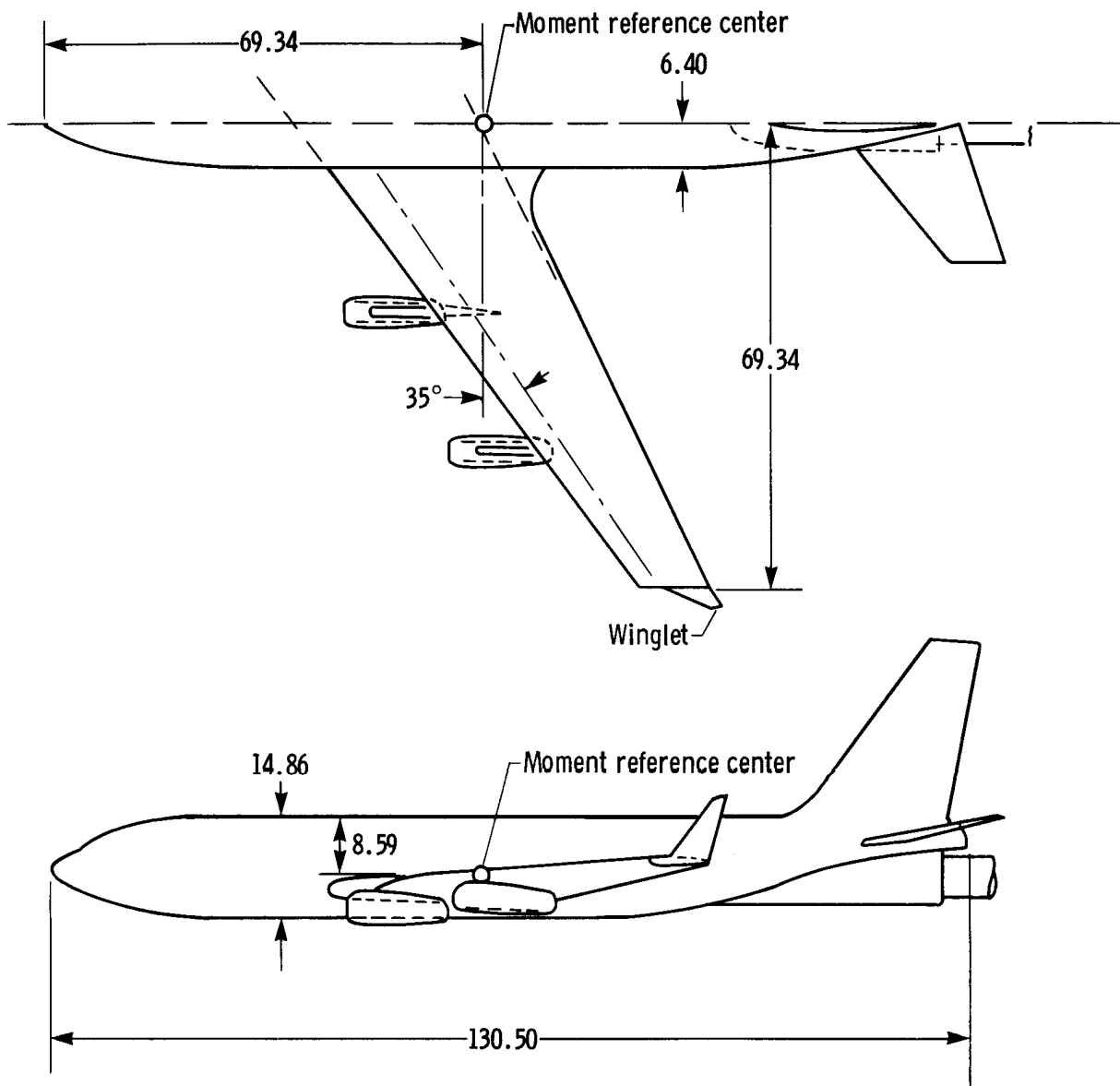
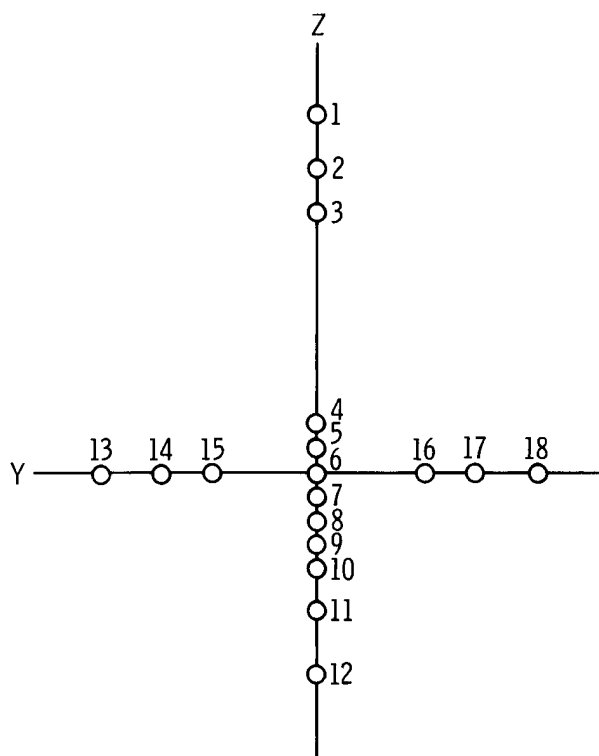


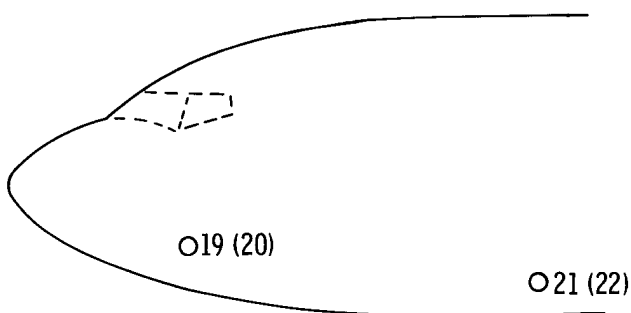
Figure 1. Drawing of 0.035 scale KC-135A model. Dimensions are in centimeters.



Figure 2. Photograph of 0.035 scale model in 8-Foot Transonic Pressure Tunnel.



(a) Nose pressure orifice arrangement relative to Y-Z axes of model.

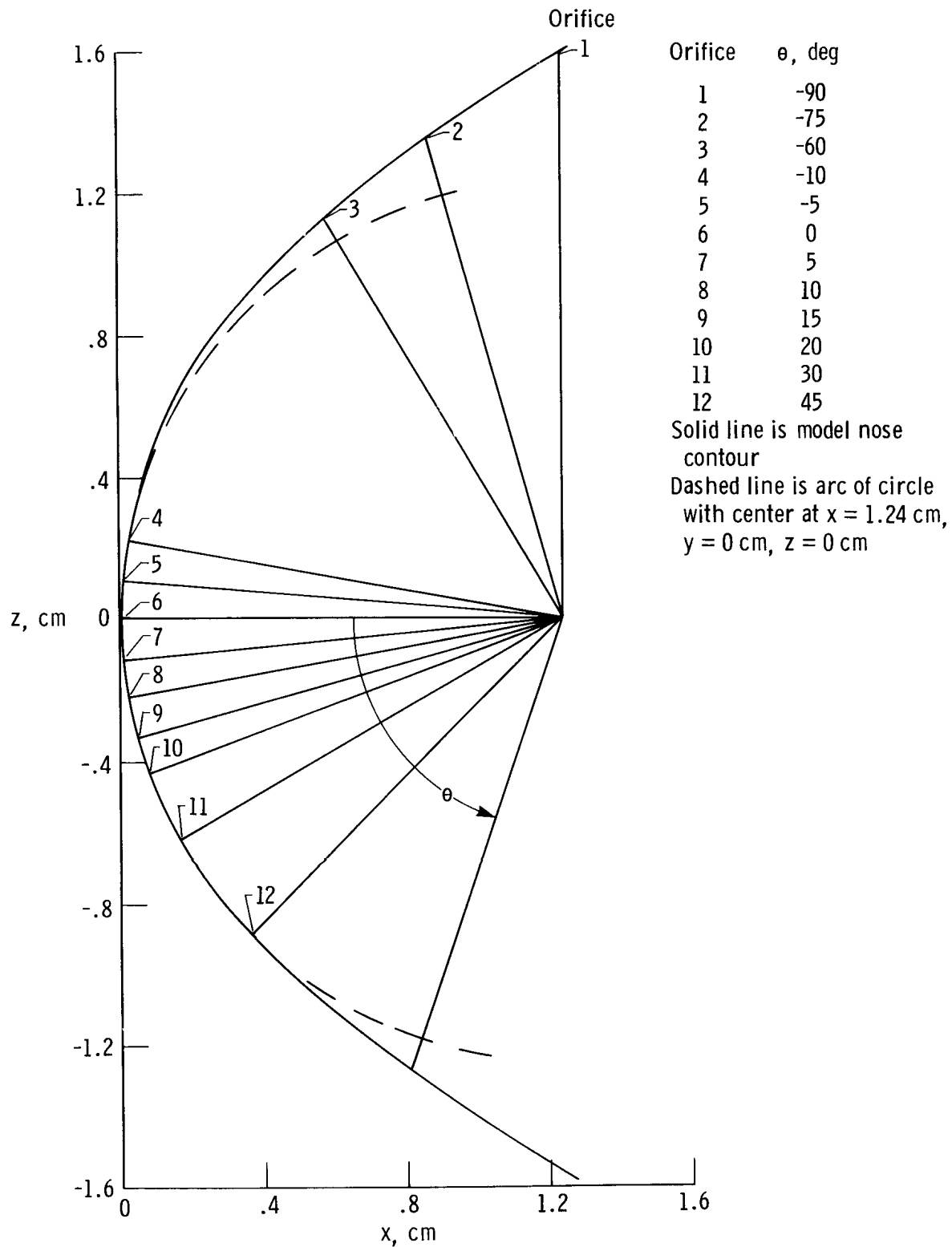


(b) Arrangement of static pressure orifices on fuselage of model. Not to scale. Numbers in parentheses refer to orifices on opposite side of vehicle.

	Model coordinate, cm		
	x	y	z
Nose orifices			
1	1.24	0	1.60
2	0.87	0	1.36
3	0.57	0	1.14
4	0.03	0	0.22
5	0.01	0	0.11
6	0	0	0
7	0.01	0	-0.11
8	0.03	0	-0.22
9	0.05	0	-0.33
10	0.09	0	-0.43
11	0.17	0	-0.62
12	0.37	0	-0.89
13	0.40	-1.01	0
14	0.18	-0.72	0
15	0.07	-0.49	0
16	0.07	0.49	0
17	0.18	0.72	0
18	0.40	1.01	0
Fuselage orifices			
19	9.80	Right	1.35
20	9.80	Left	1.35
21	26.26	Right	-4.90
22	26.26	Left	-4.90

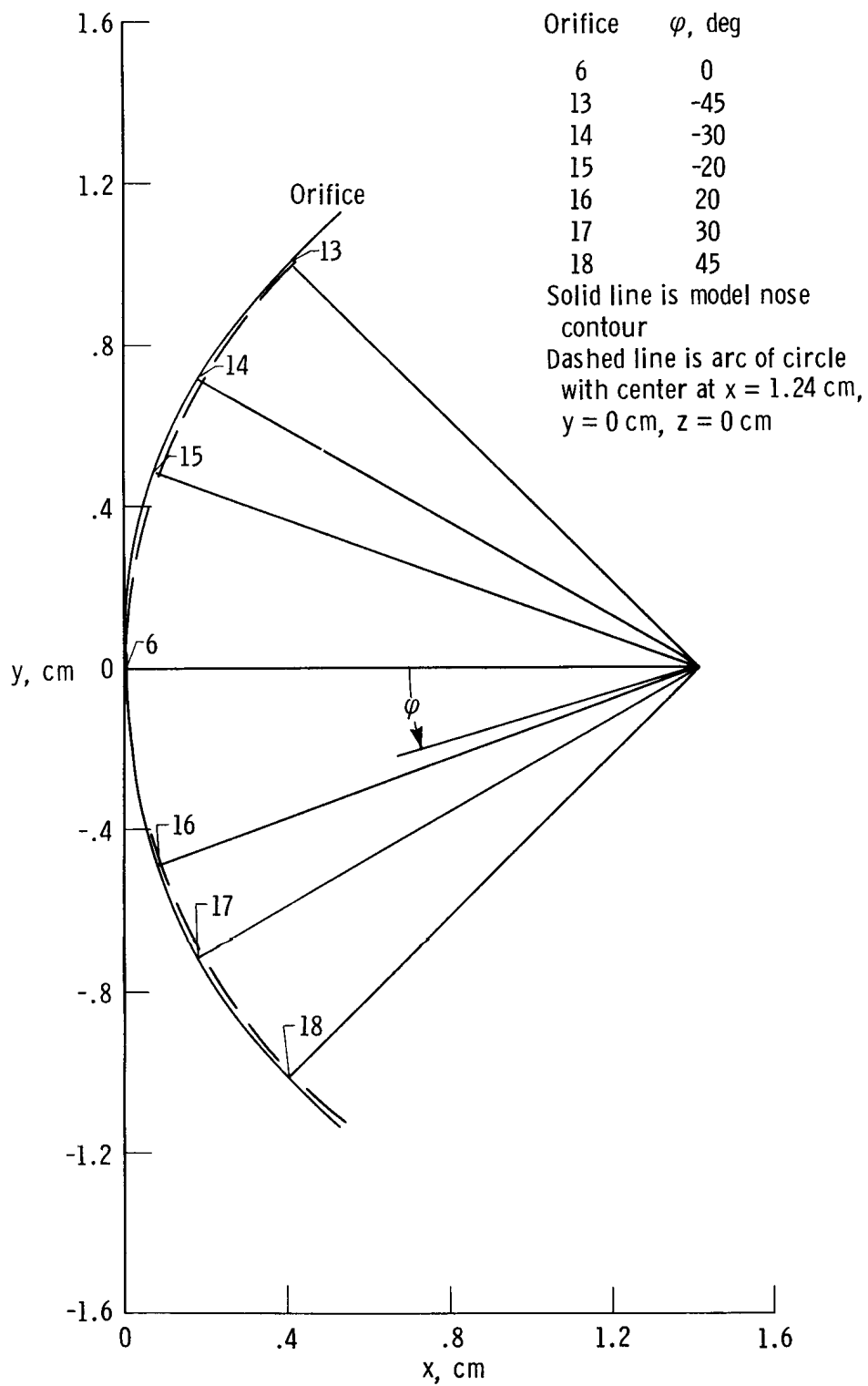
(c) Coordinates of pressure orifices on nose and fuselage.

Figure 3. Locations of pressure orifices on model.



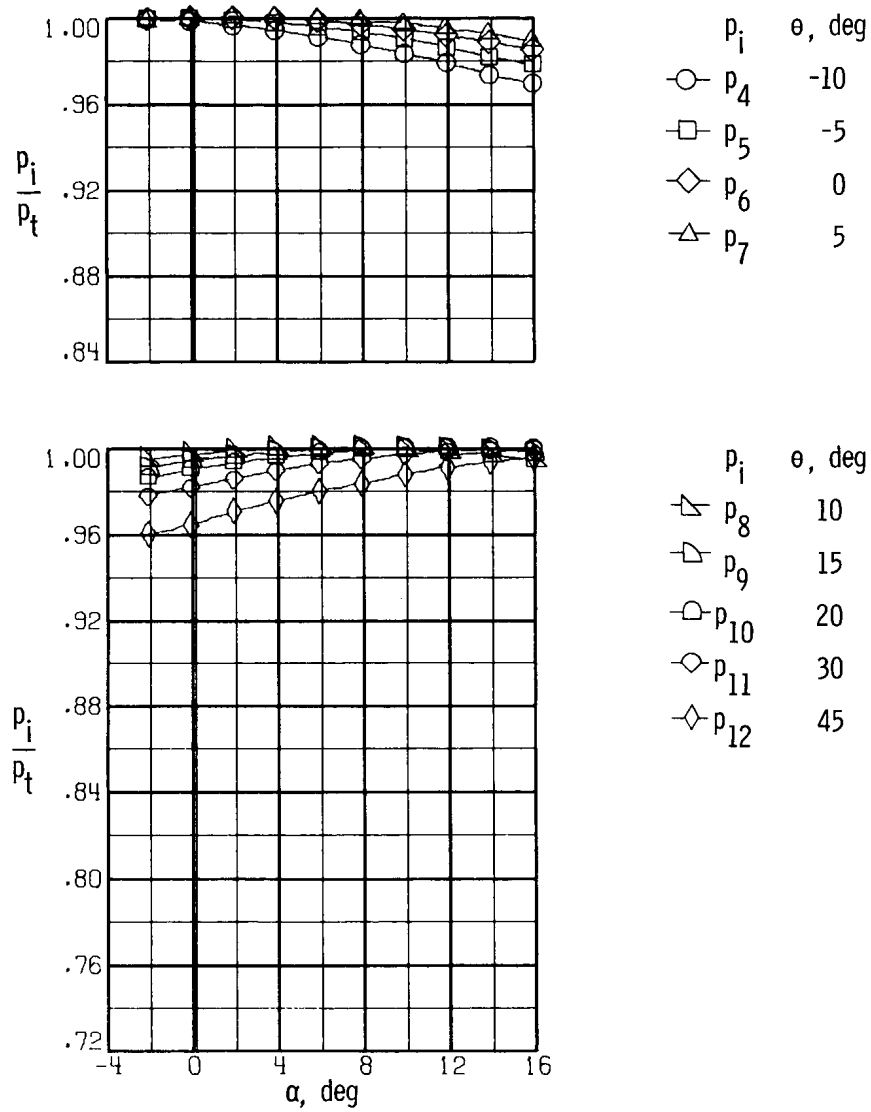
(a) Orifices in plane of vertical centerline.

Figure 4. Location of pressure orifices on nose of model plotted in  $x$ ,  $z$  coordinates.



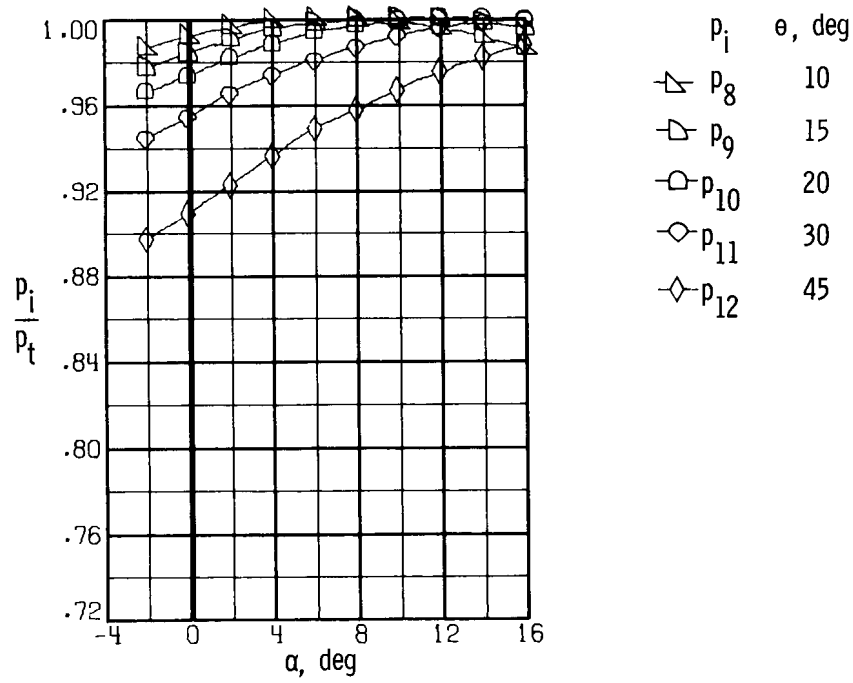
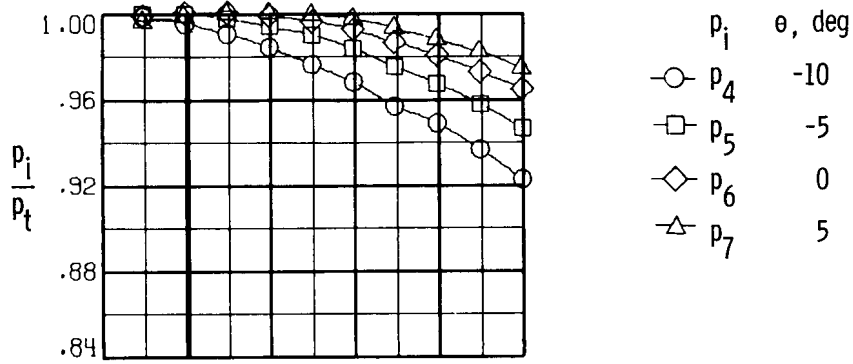
(b) Orifices in plane of horizontal centerline.

Figure 4. Concluded.



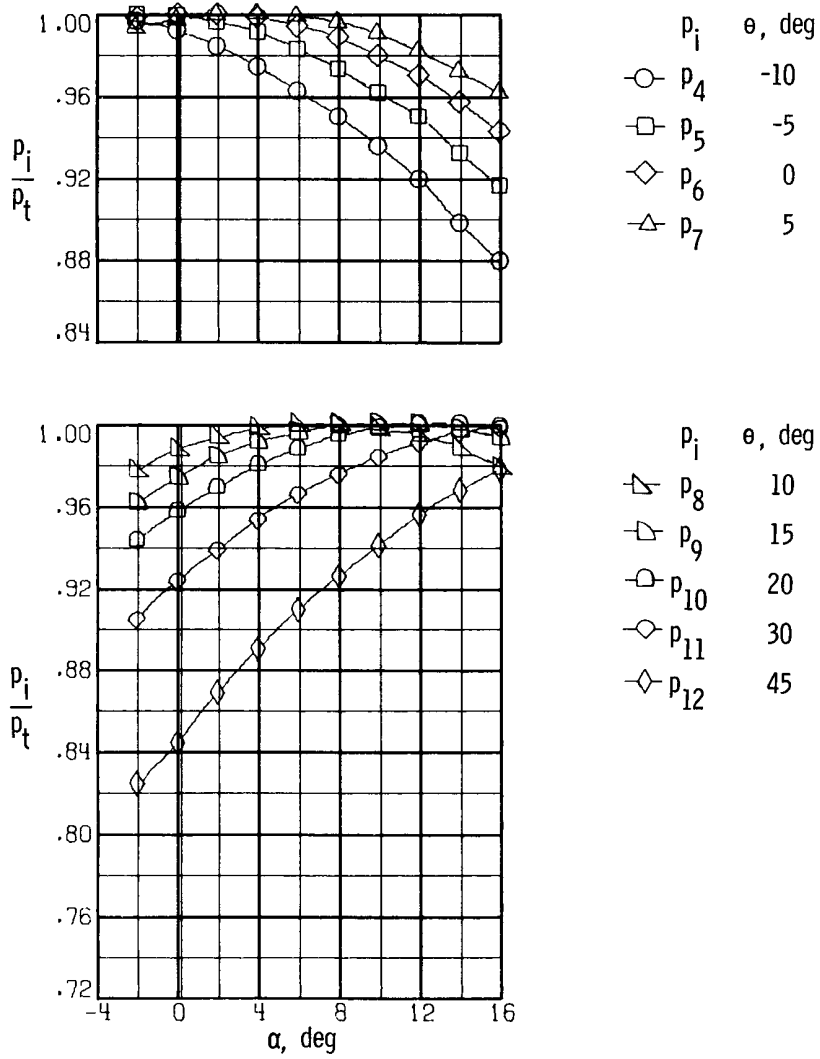
(a)  $M = 0.30$ .

Figure 5. Ratio of pressures measured on vertical centerline of nose to stagnation pressure plotted against angle of attack.  $\beta = 0^\circ$ .



(b)  $M = 0.50$ .

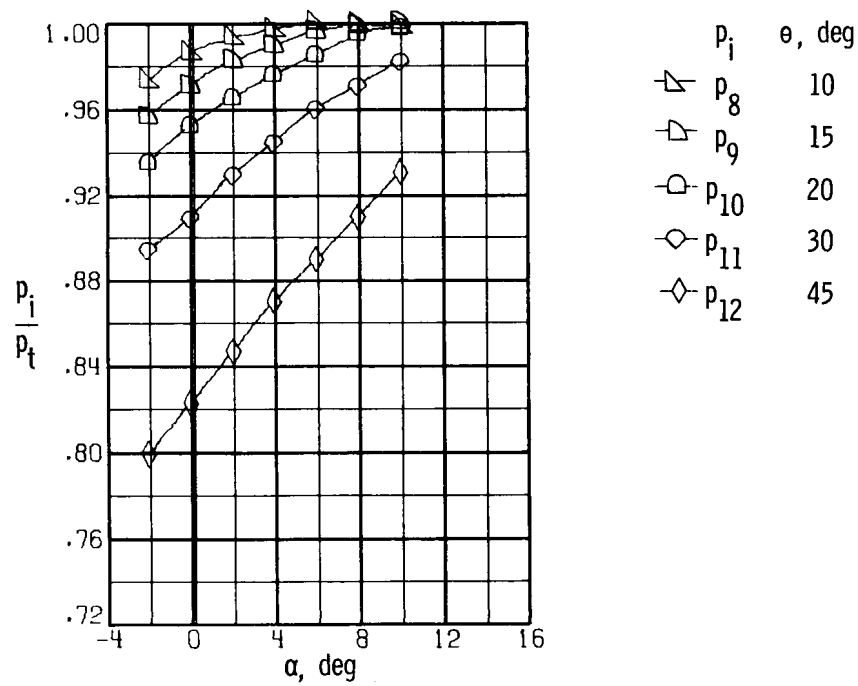
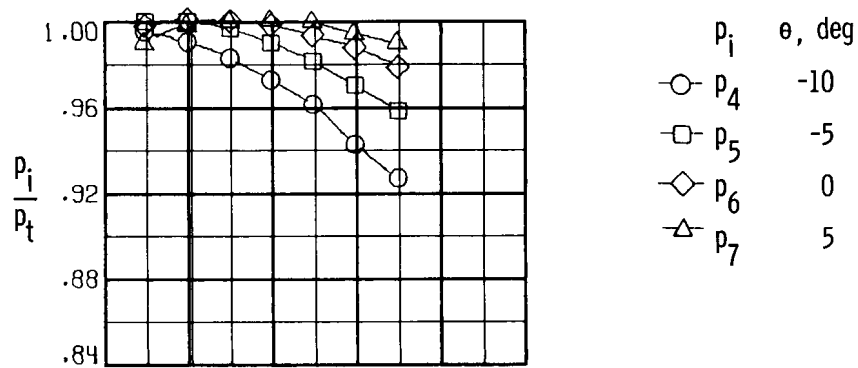
Figure 5. Continued.



(c)  $M = 0.70$ .

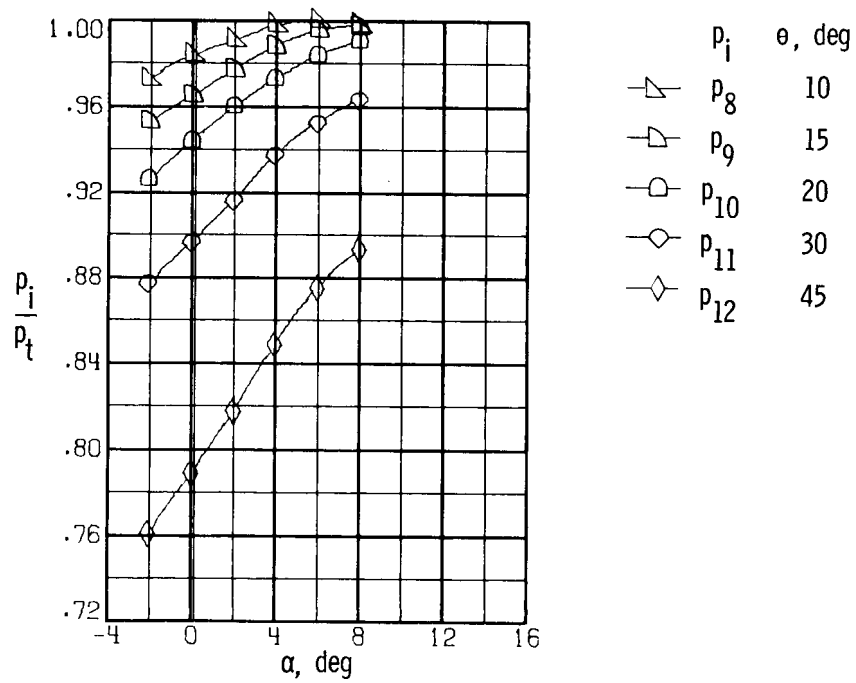
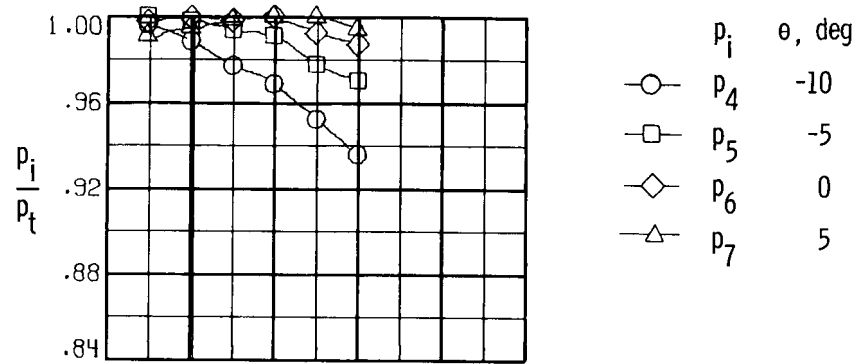
Figure 5. Continued.





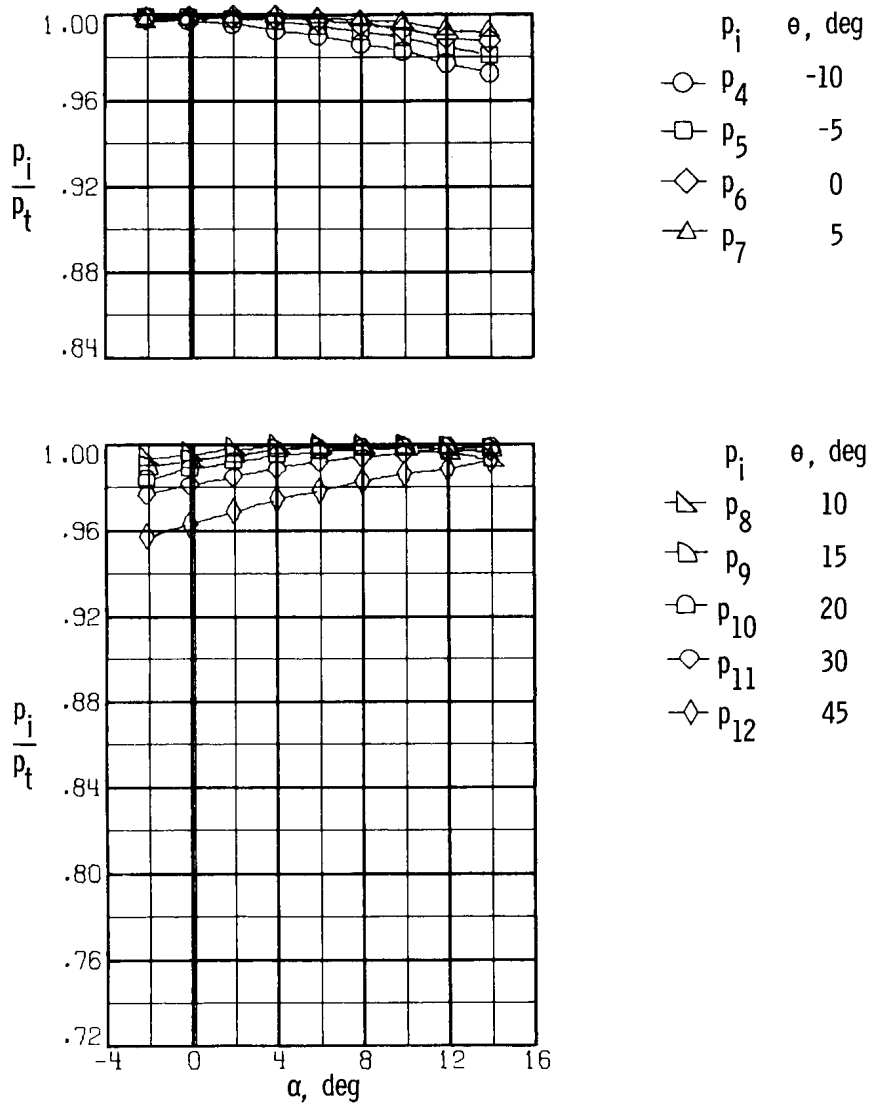
(d)  $M = 0.78$ .

Figure 5. Continued.



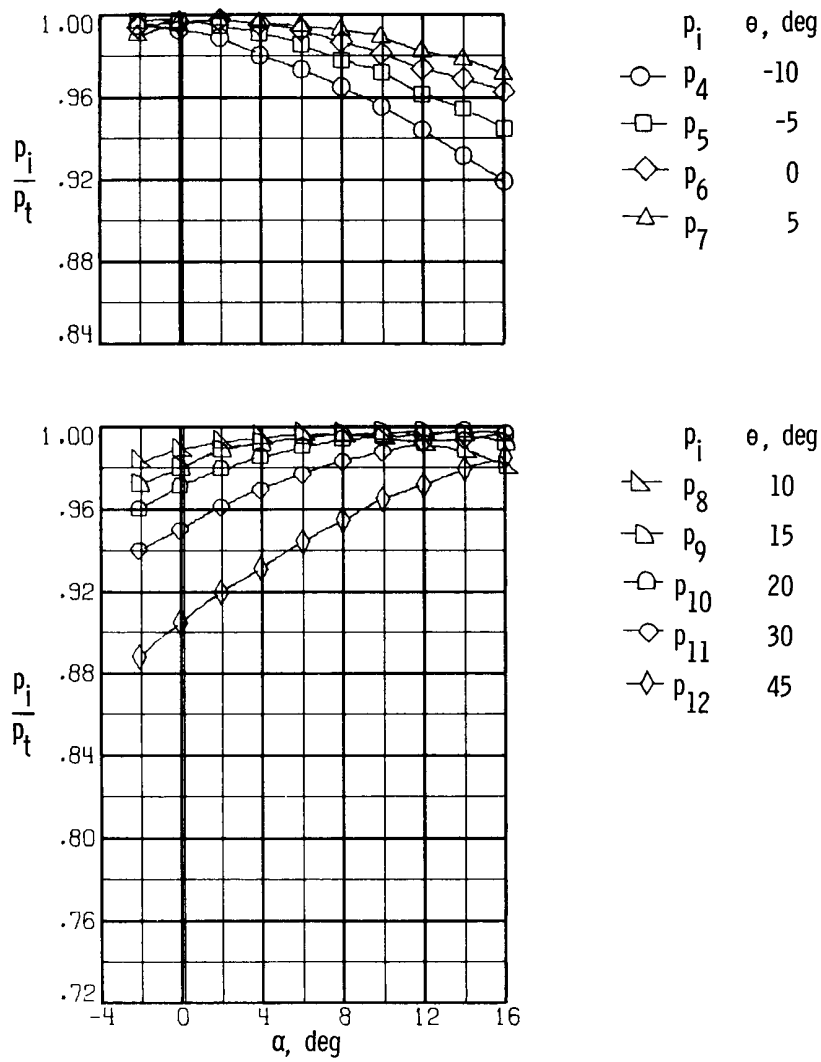
(e)  $M = 0.90$ .

Figure 5. Concluded.



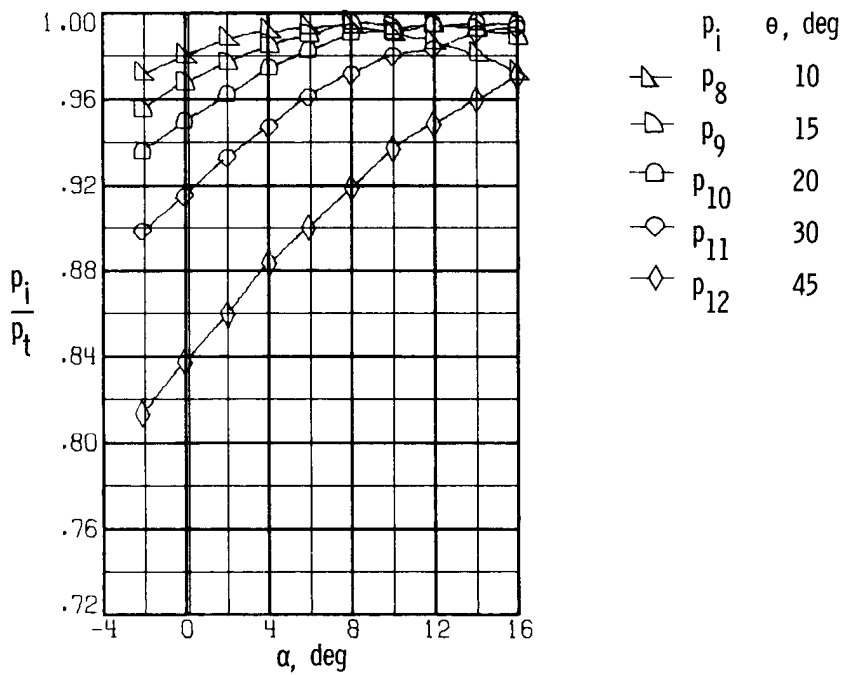
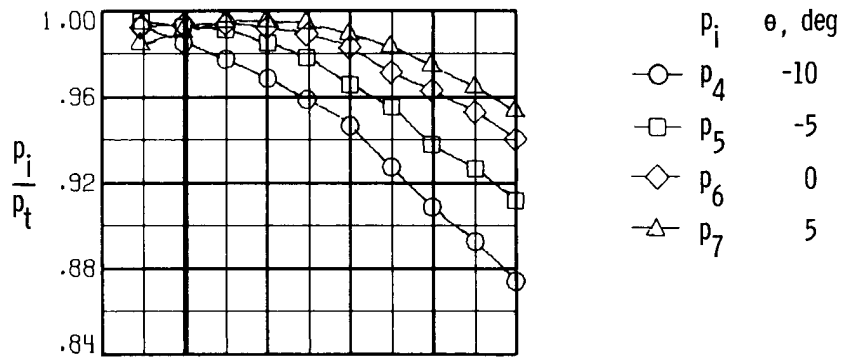
(a)  $M = 0.30$ .

Figure 6. Ratio of pressures measured on vertical centerline of nose to stagnation pressure plotted against angle of attack.  $\beta = 5^\circ$ .



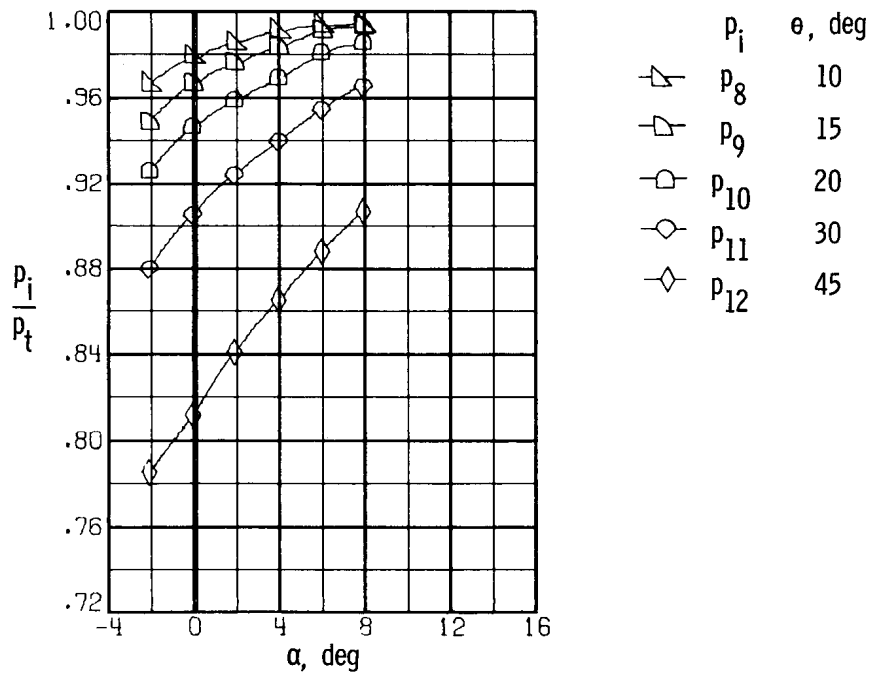
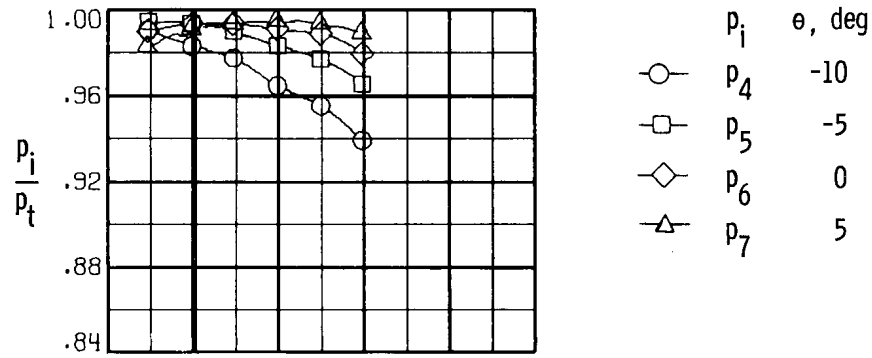
(b)  $M = 0.50$ .

Figure 6. Continued.



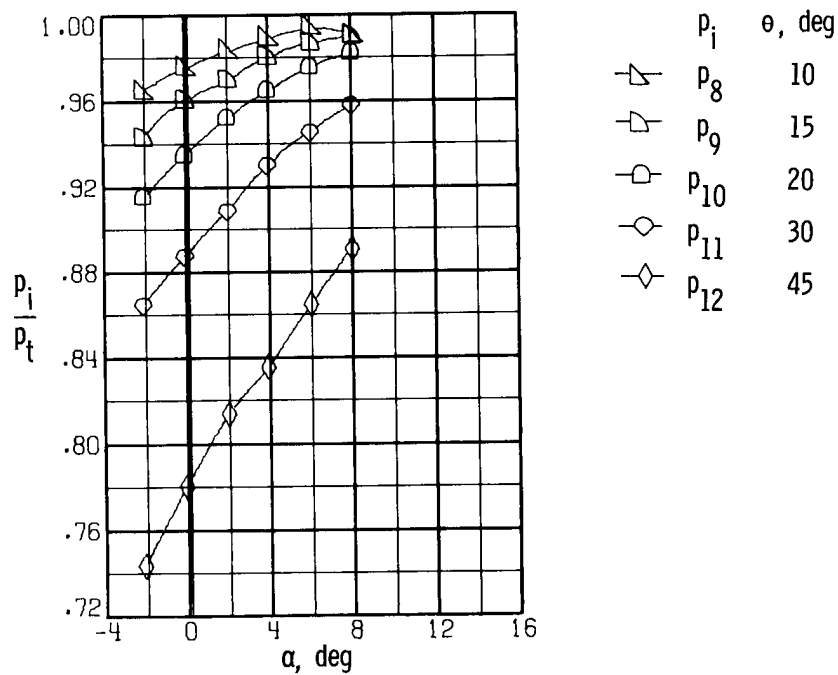
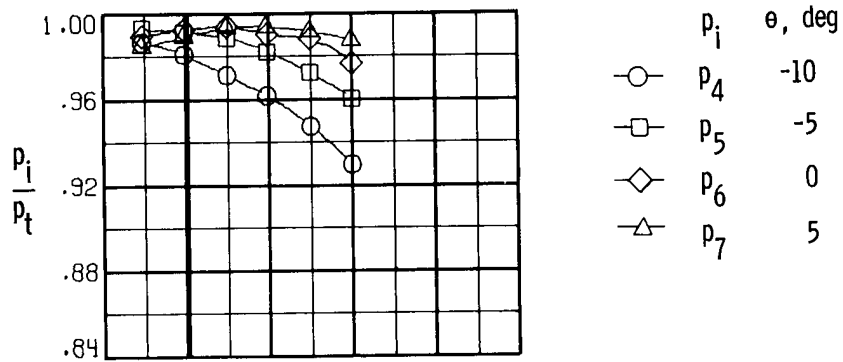
(c)  $M = 0.70$ .

Figure 6. Continued.



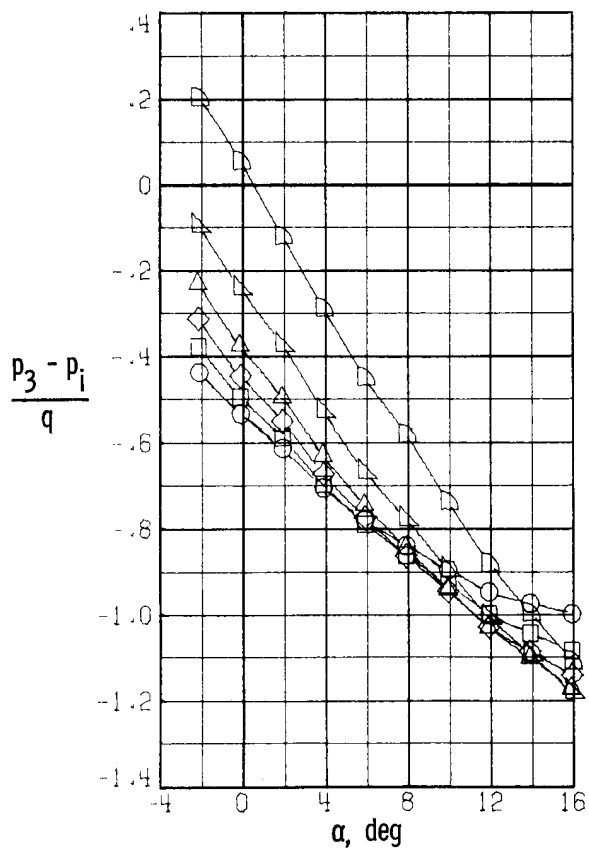
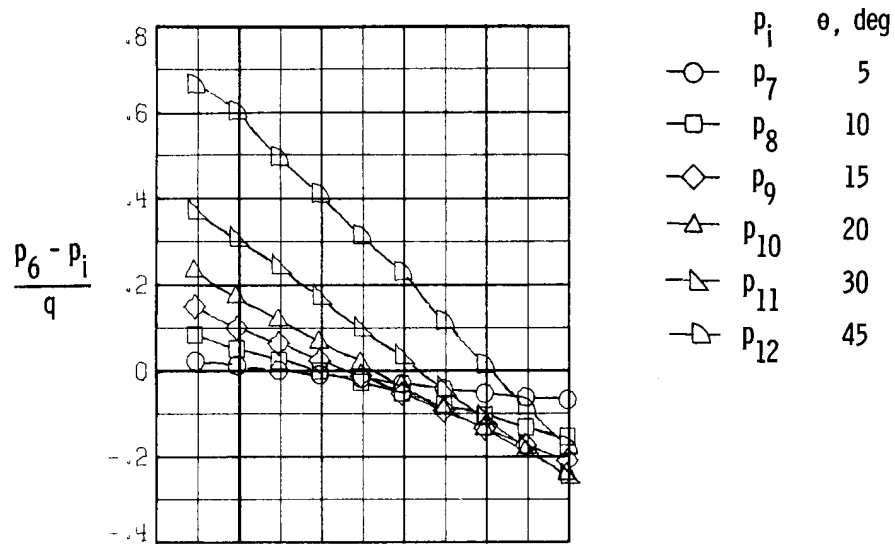
(d)  $M = 0.78$ .

Figure 6. Continued.



(e)  $M = 0.90$ .

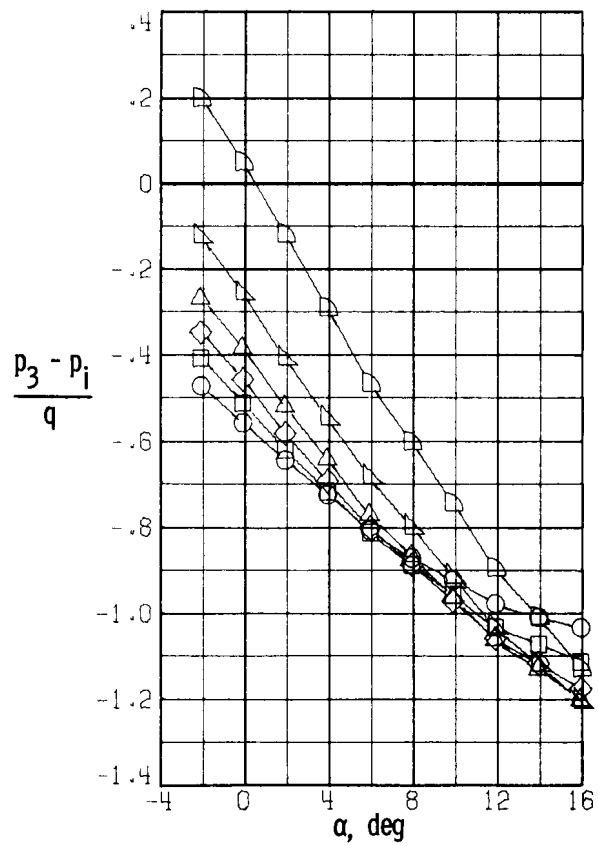
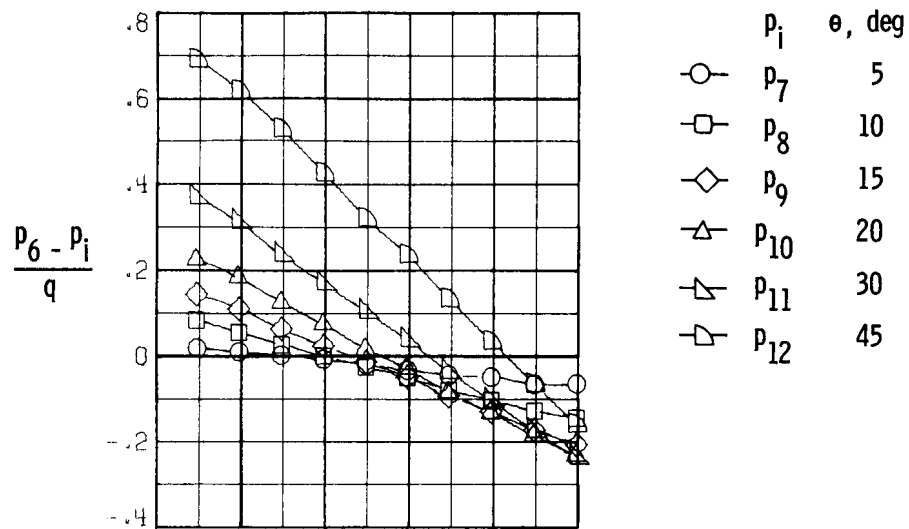
Figure 6. Concluded.



(a)  $M = 0.30$ .

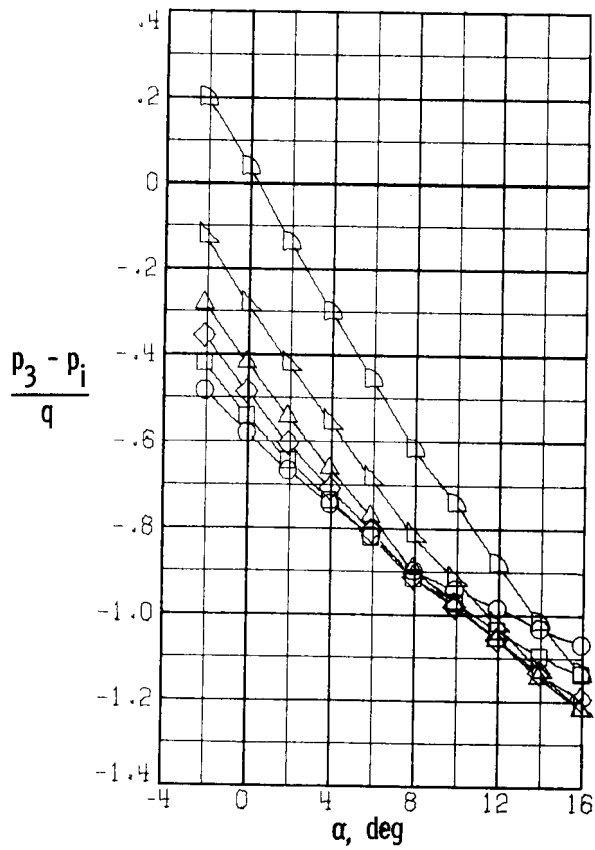
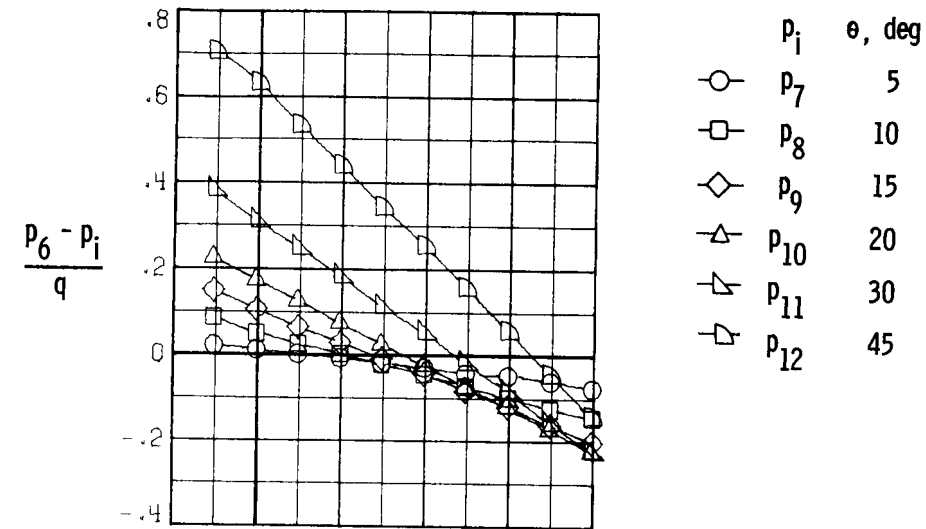
Figure 7. Pressure parameter for selected orifices plotted against angle of attack.  $\beta = 0^\circ$ .





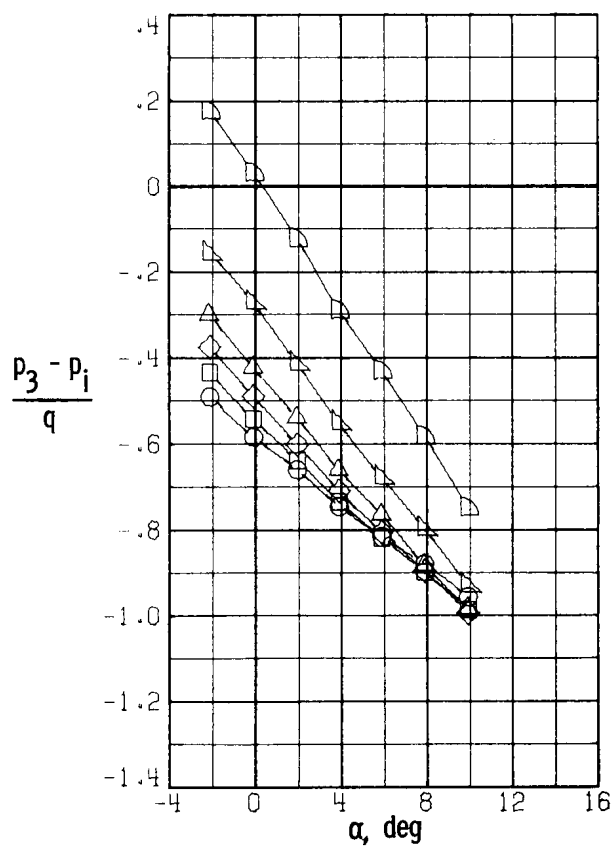
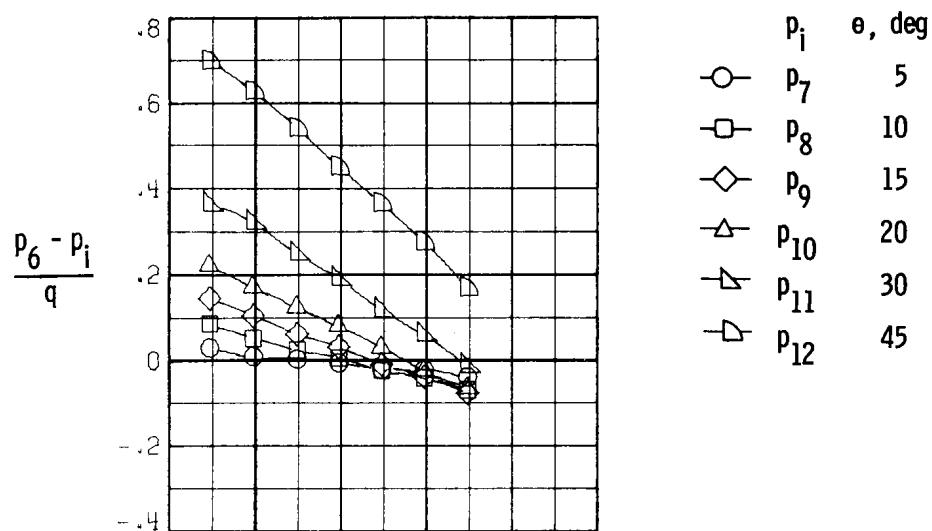
(b)  $M = 0.50$ .

Figure 7. Continued.



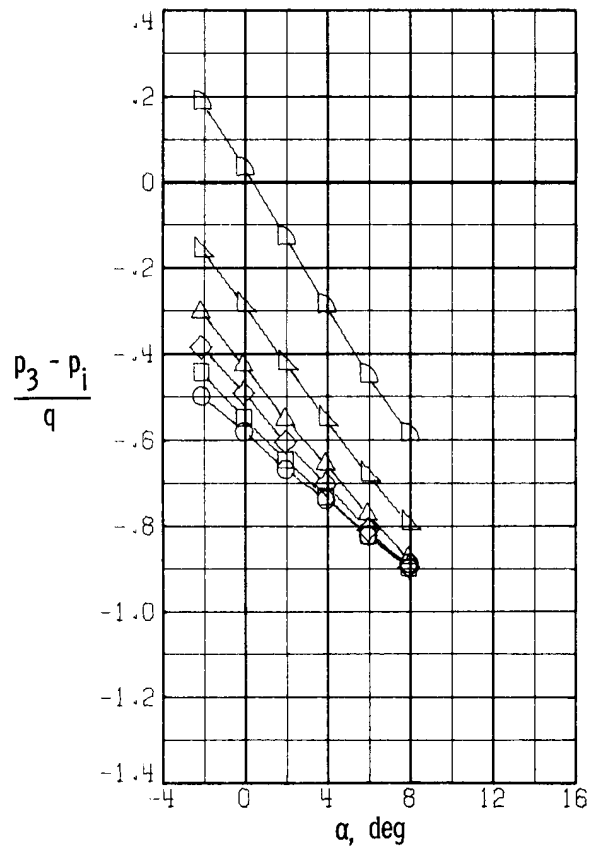
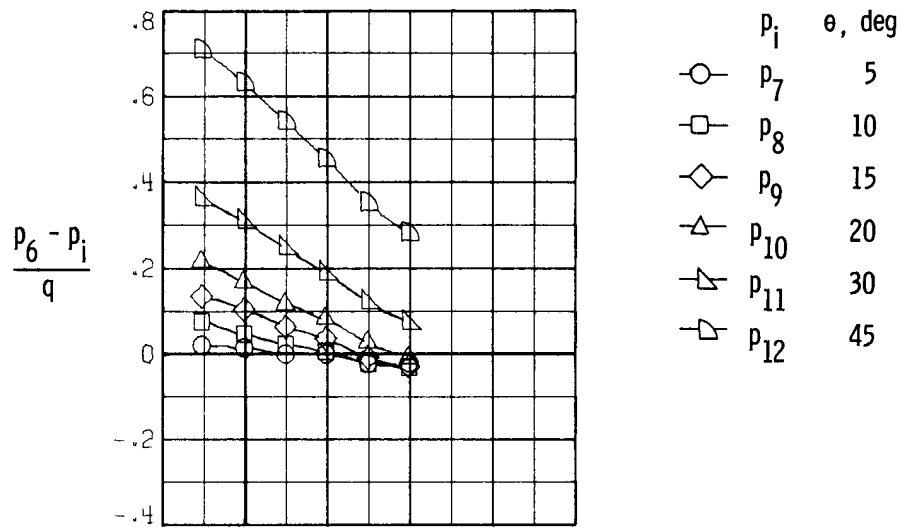
(c)  $M = 0.70$ .

Figure 7. Continued.



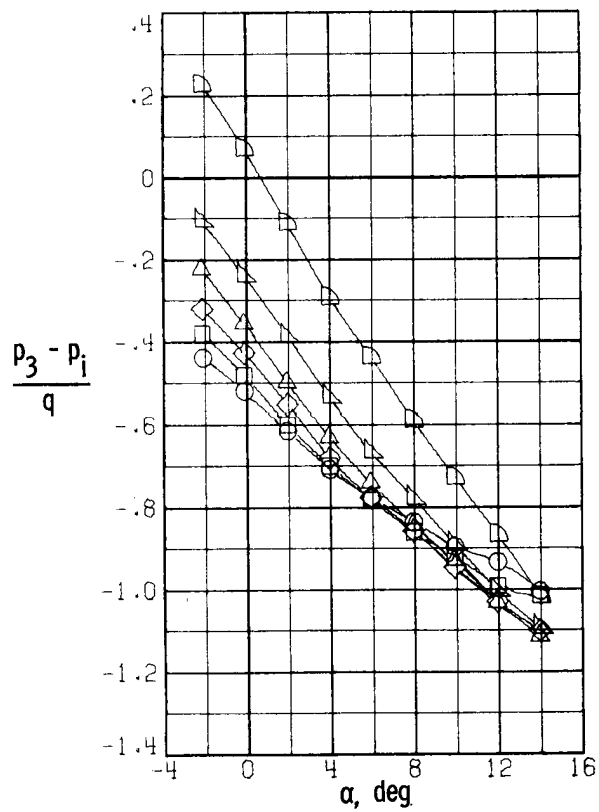
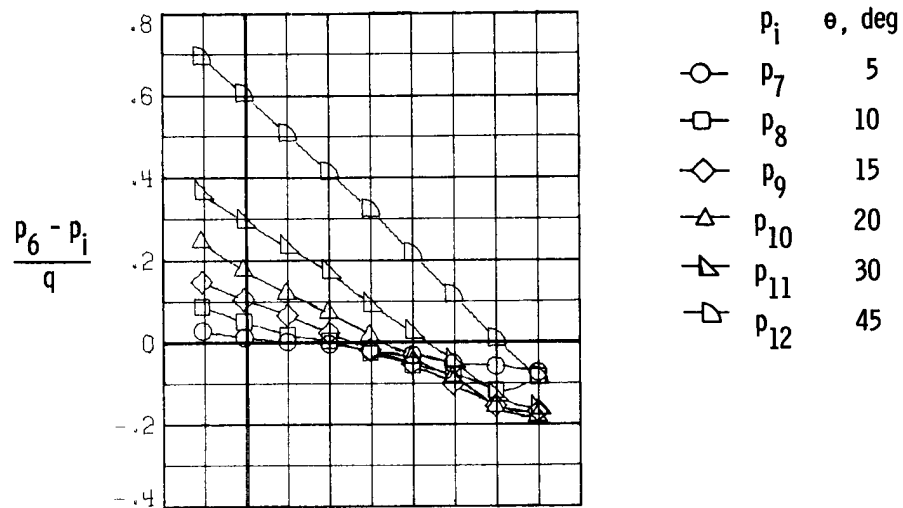
(d)  $M = 0.78$ .

Figure 7. Continued.



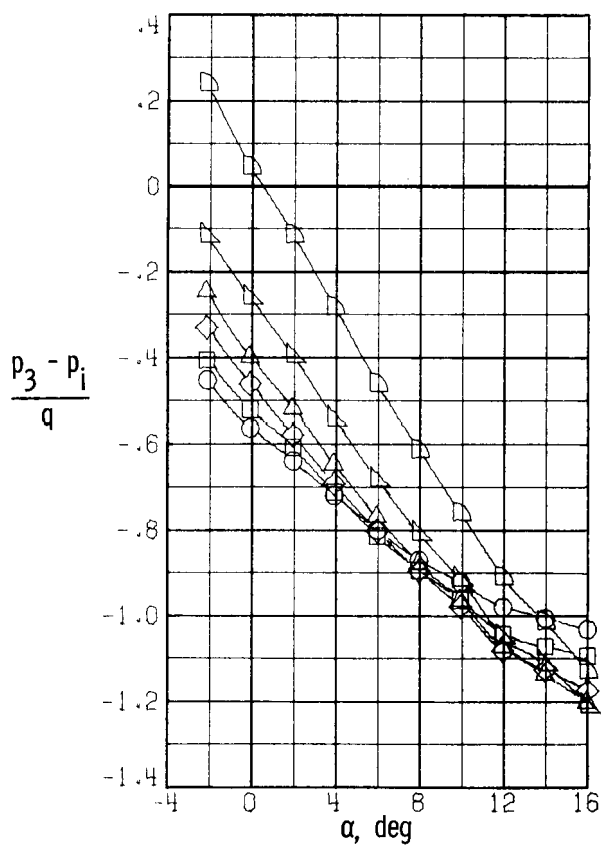
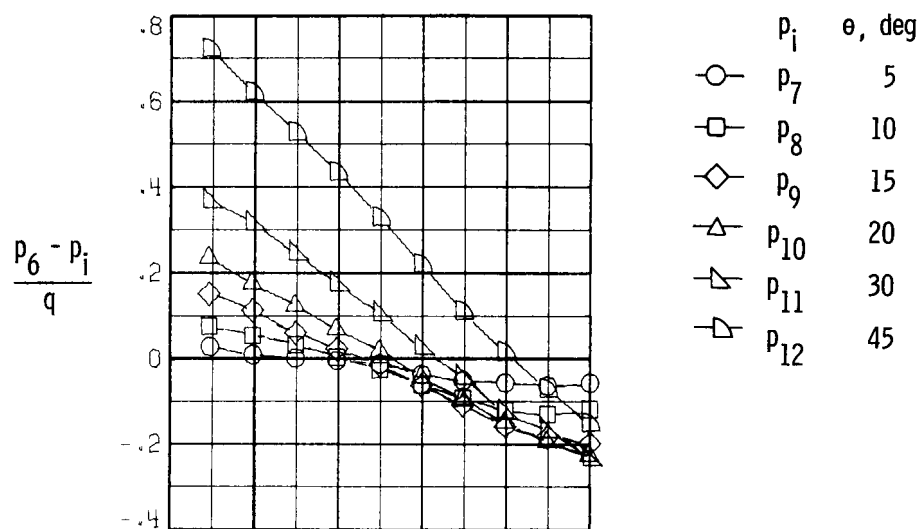
(e)  $M = 0.90$ .

Figure 7. Concluded.



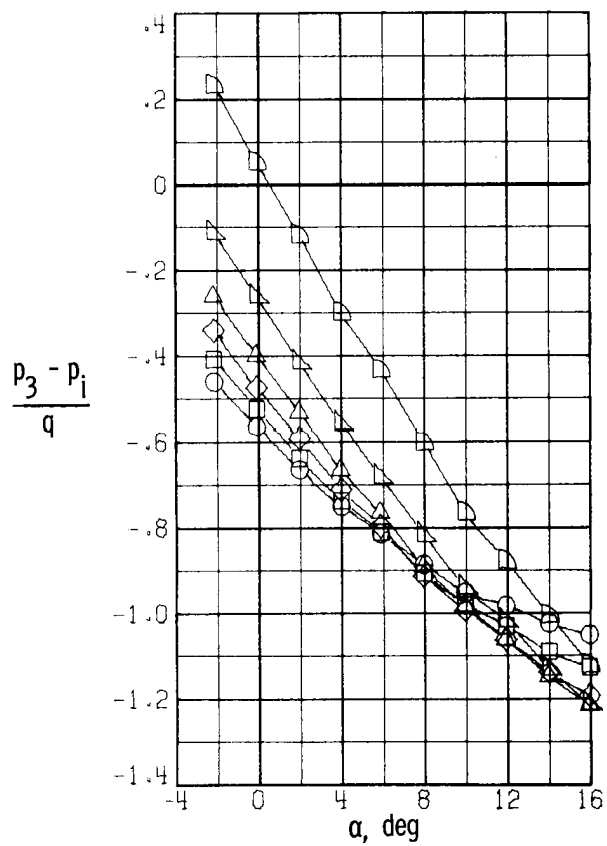
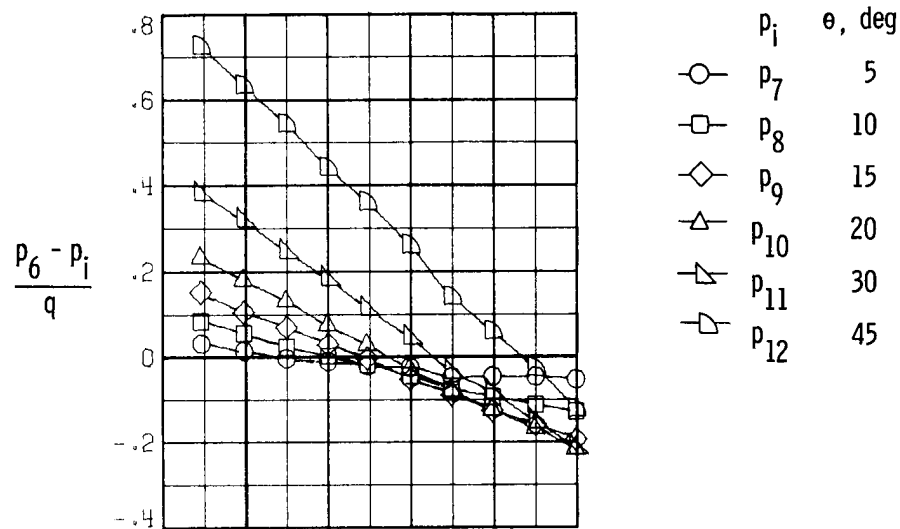
(a)  $M = 0.30$ .

Figure 8. Pressure parameter for selected orifices plotted against angle of attack.  $\beta = 5^\circ$ .



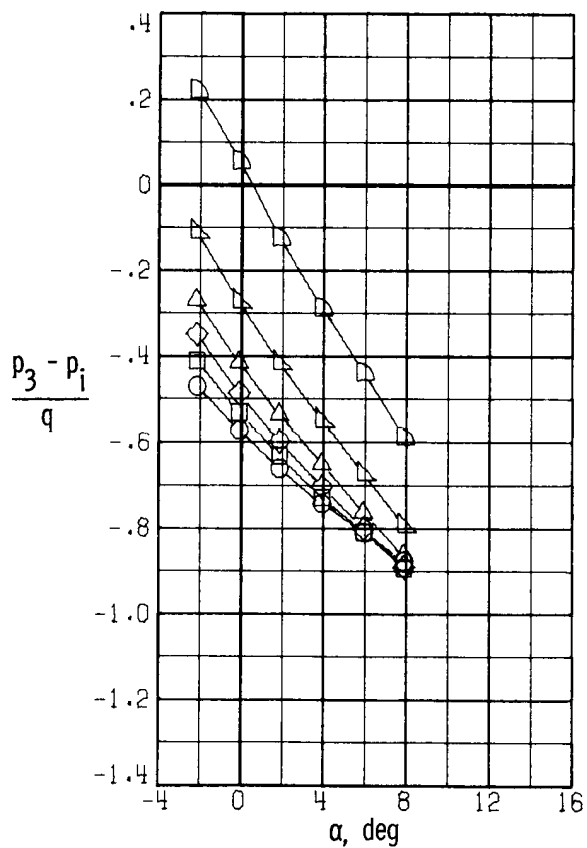
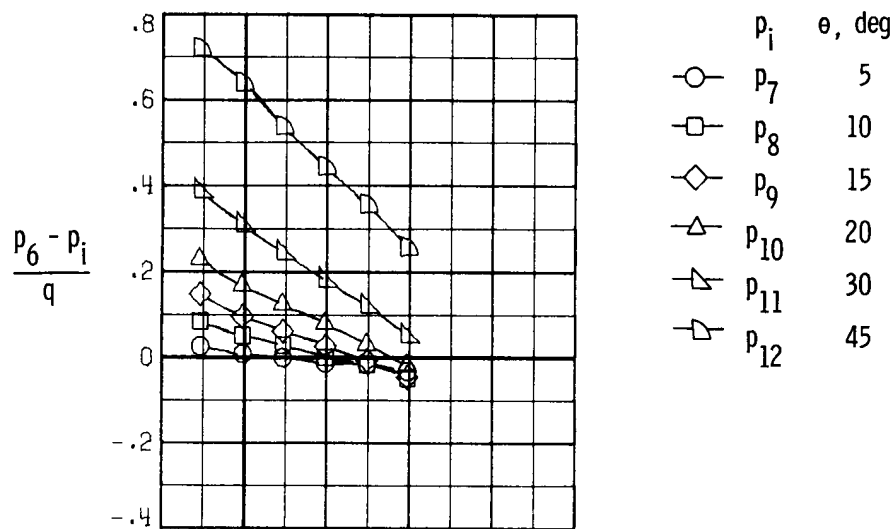
(b)  $M = 0.50$ .

Figure 8. Continued.



(c)  $M = 0.70$ .

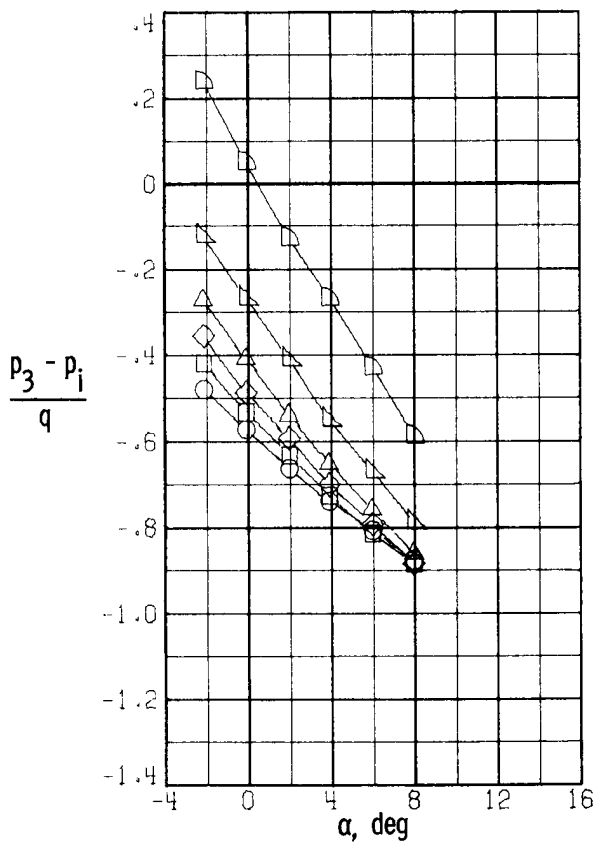
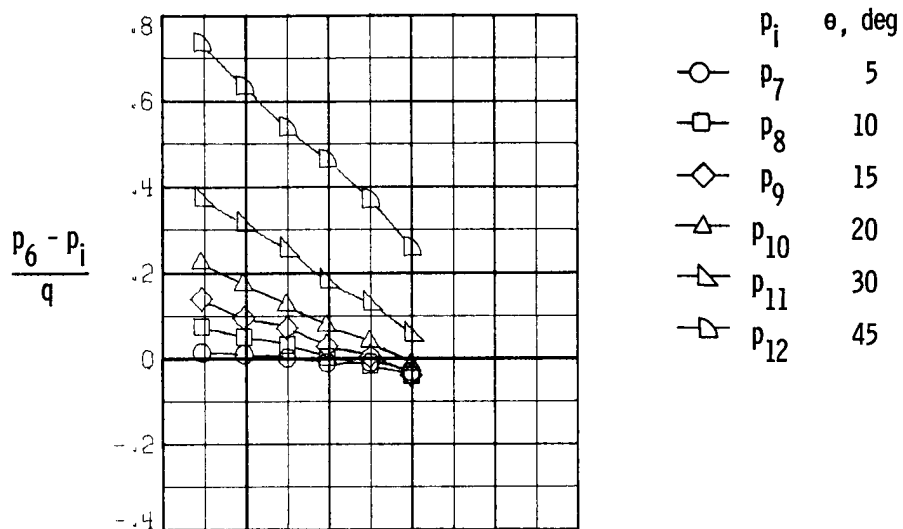
Figure 8. Continued.



(d)  $M = 0.78$ .

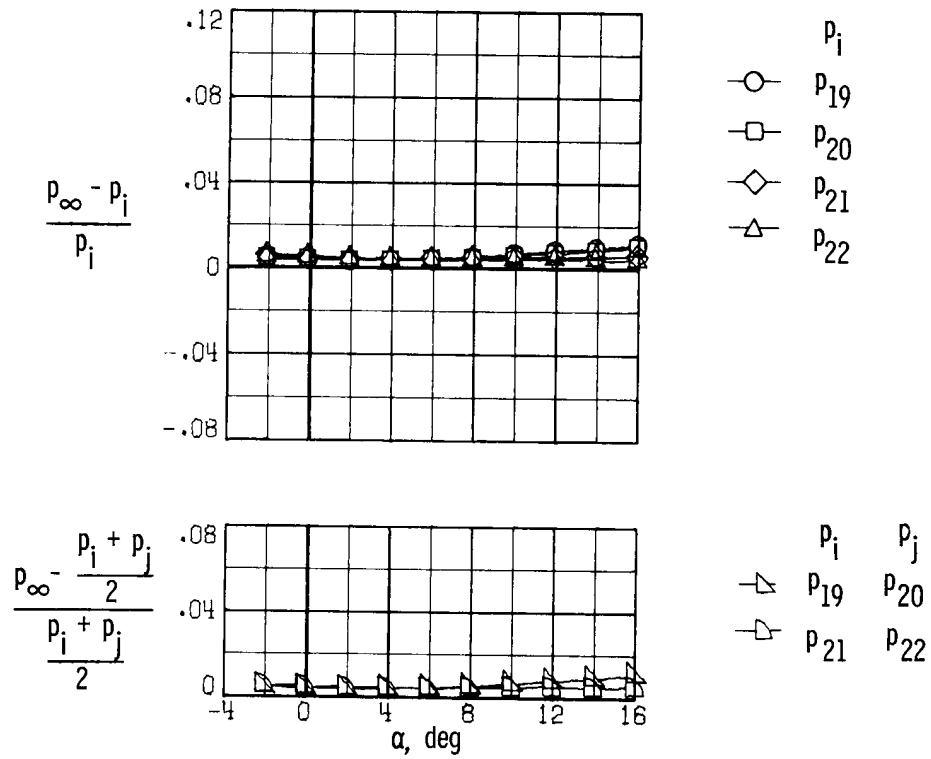
Figure 8. Continued.





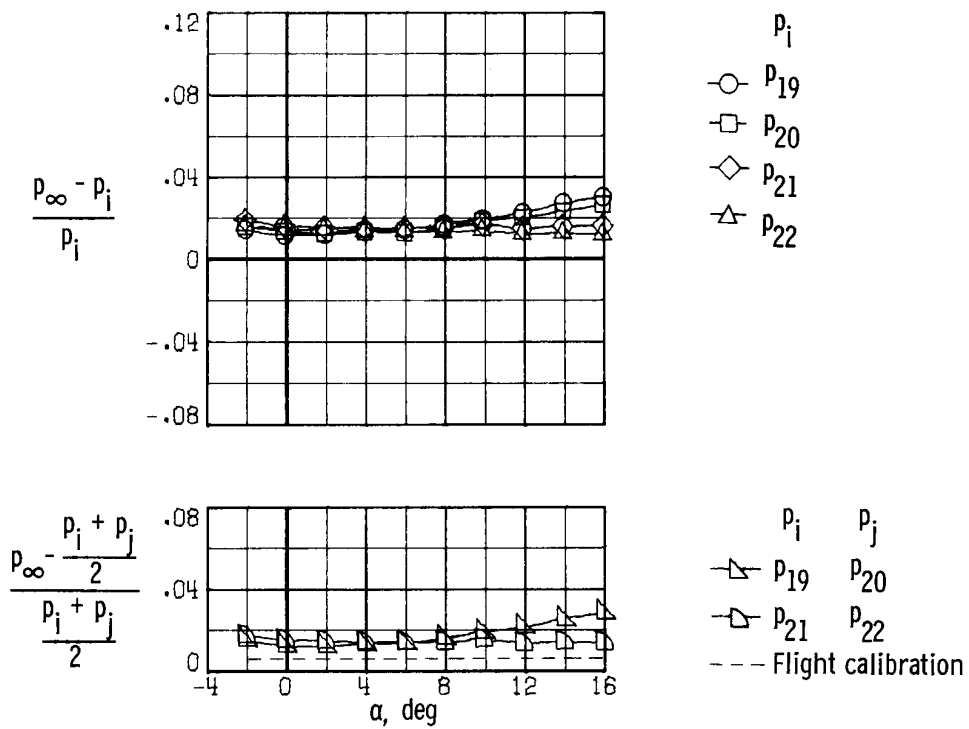
(e)  $M = 0.90$ .

Figure 8. Concluded.



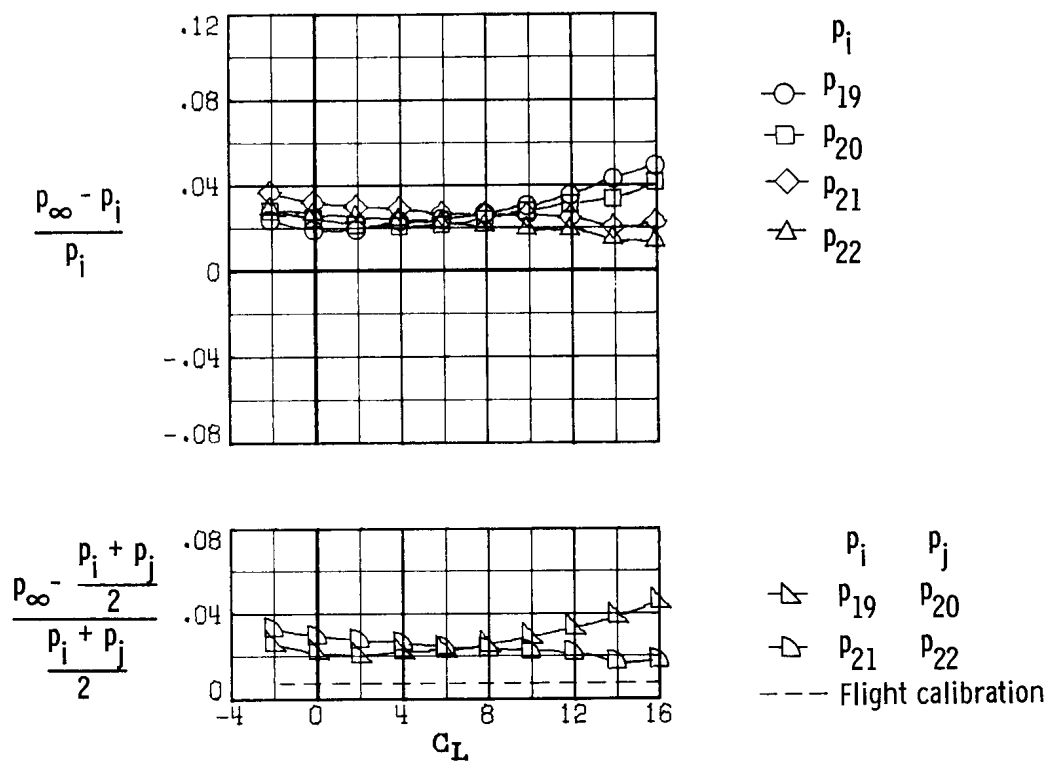
(a)  $M = 0.30$ .

Figure 9. Static pressure correction for fuselage pressure orifices plotted against angle of attack. Single orifices and averaged orifices.  $\beta = 0^\circ$ .



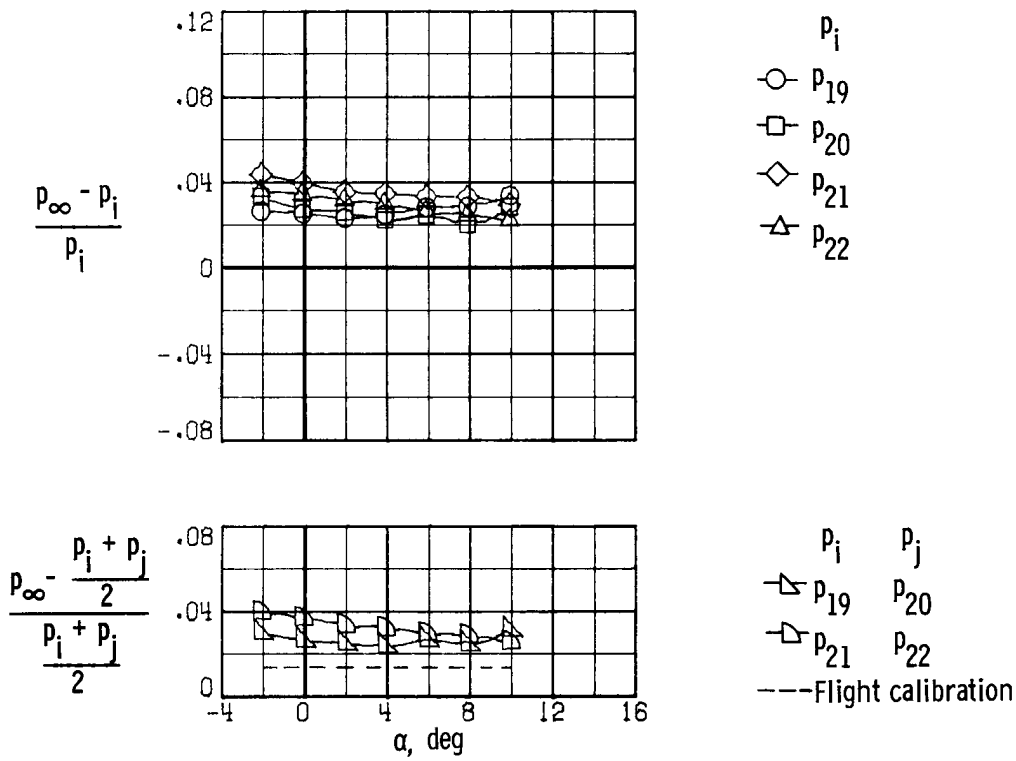
(b)  $M = 0.50$ .

Figure 9. Continued.



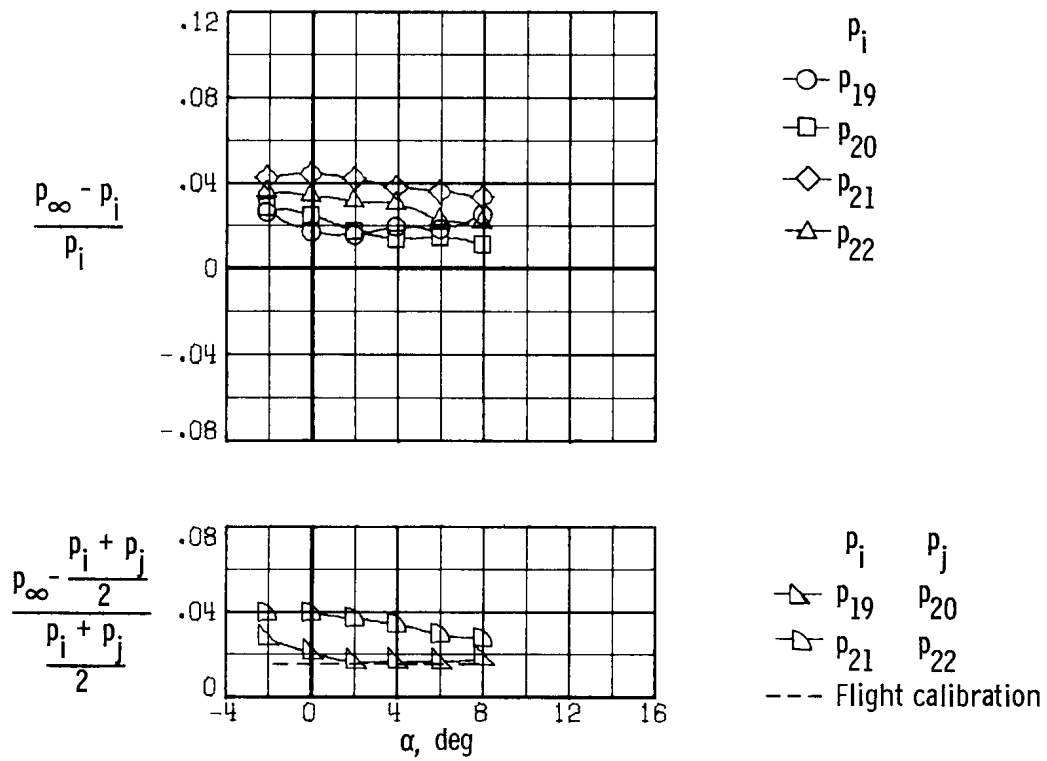
(c)  $M = 0.70$ .

Figure 9. Continued.



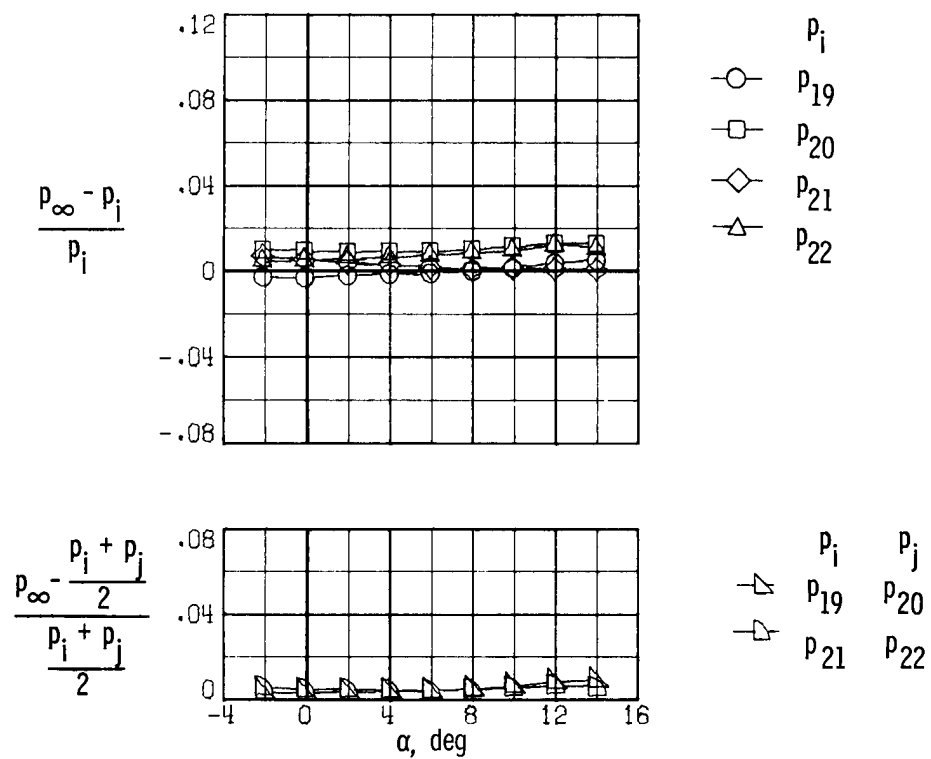
(d)  $M = 0.78$ .

Figure 9. Continued.



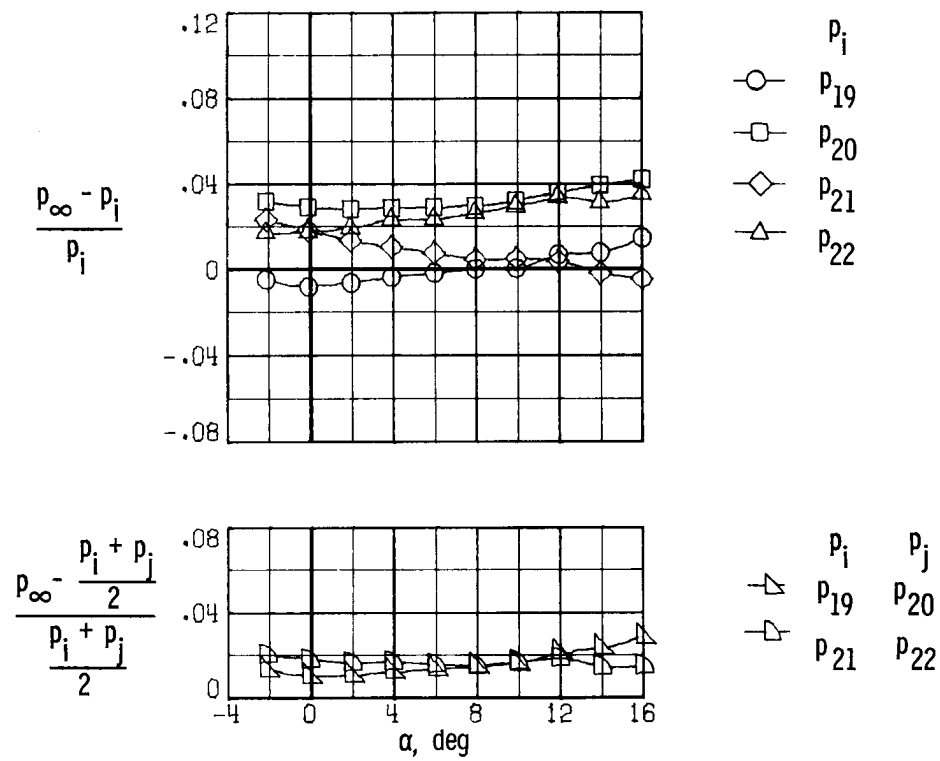
(e)  $M = 0.90$ .

Figure 9. Concluded.



(a)  $M = 0.30$ .

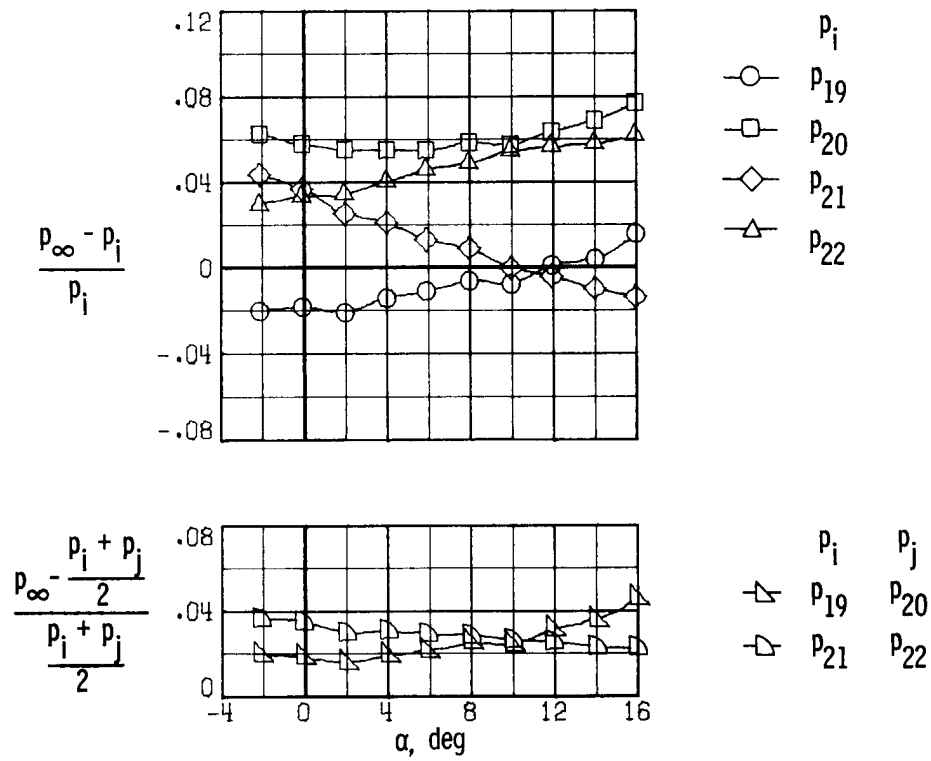
Figure 10. Static pressure correction for fuselage pressure orifices plotted against angle of attack. Single orifices and averaged orifices.  $\beta = 5^\circ$ .



(b)  $M = 0.50$ .

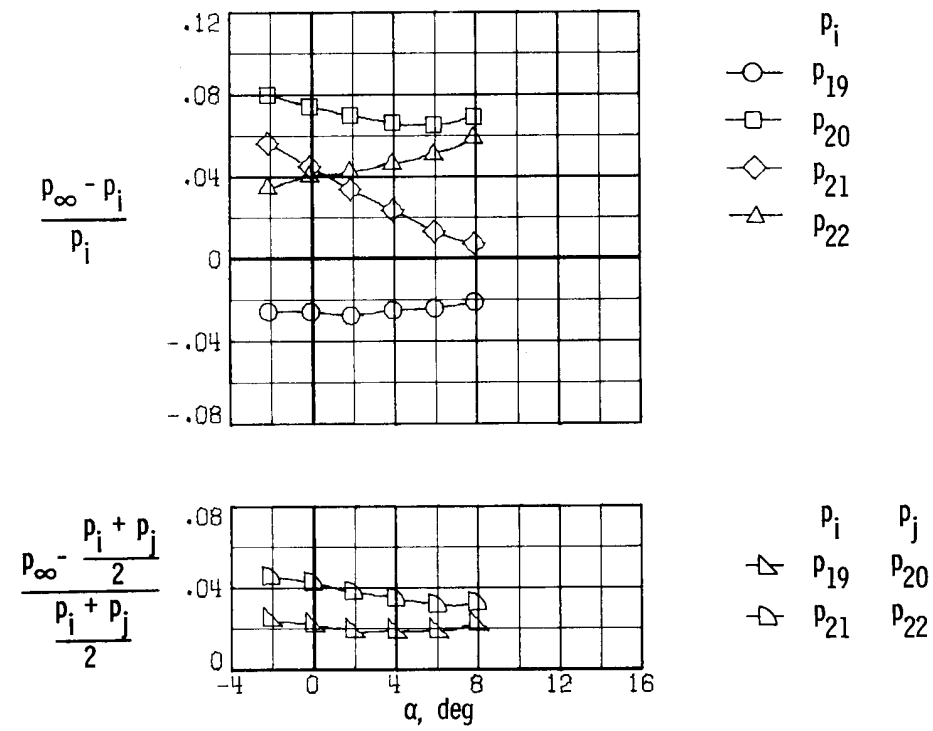
Figure 10. Continued.





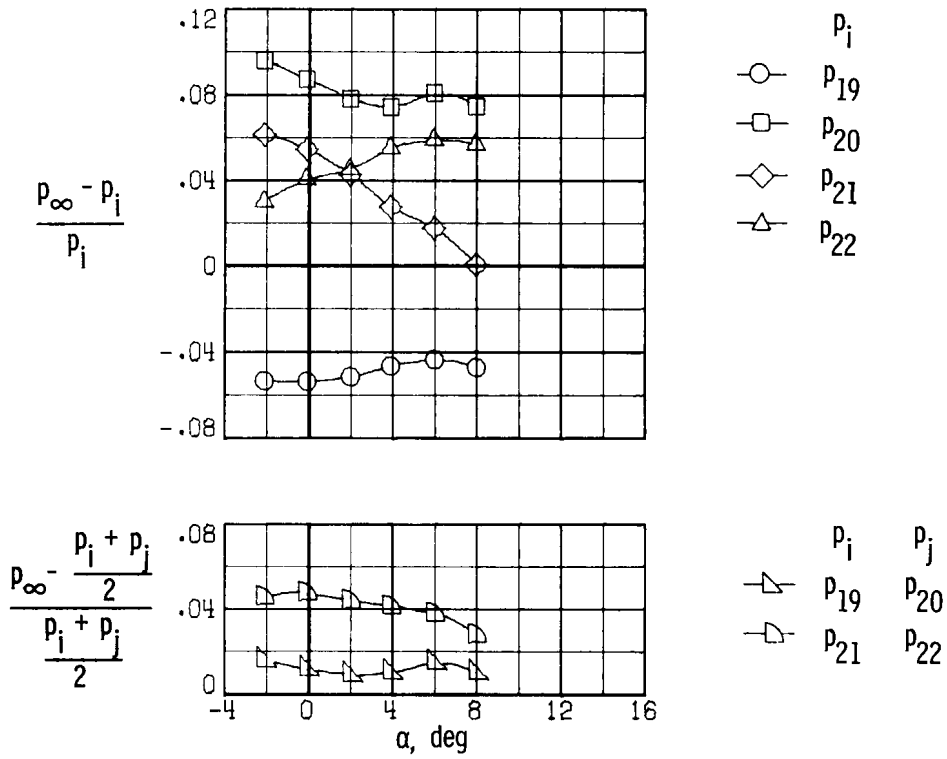
(c)  $M = 0.70$ .

Figure 10. Continued.



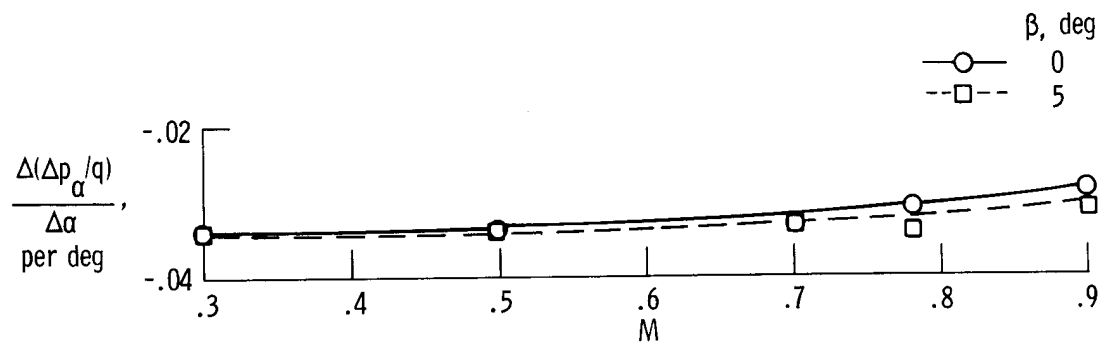
(d)  $M = 0.78$ .

Figure 10. Continued.

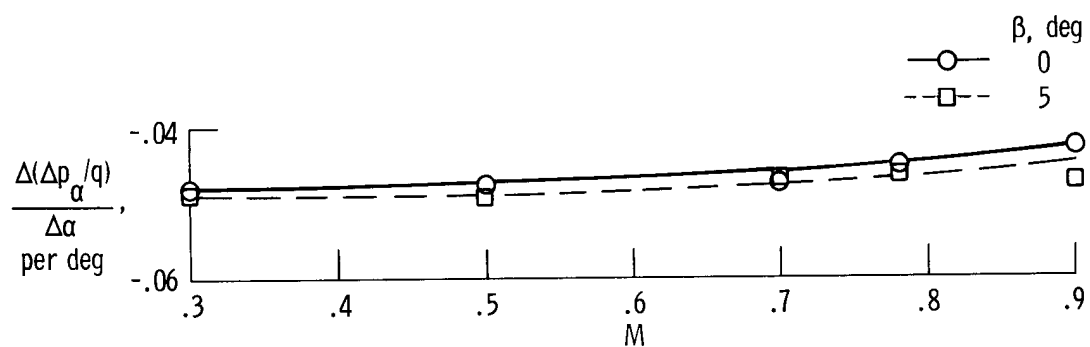


(e)  $M = 0.90$ .

Figure 10. Concluded.

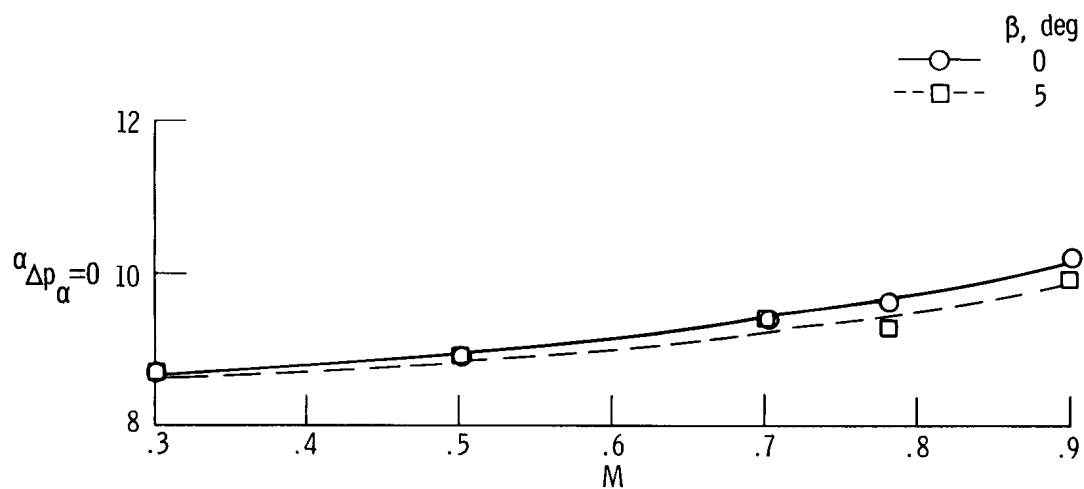


(a)  $\Delta p_\alpha = p_6 - p_{11}$ .

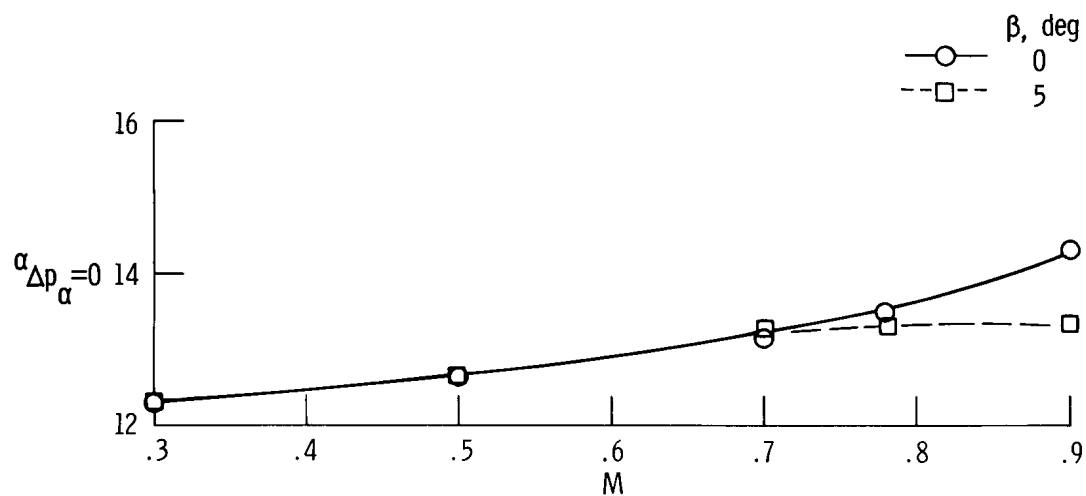


(b)  $\Delta p_\alpha = p_6 - p_{12}$ .

Figure 11. Angle of attack parameter sensitivity for two pressure orifice pairs plotted against Mach number.

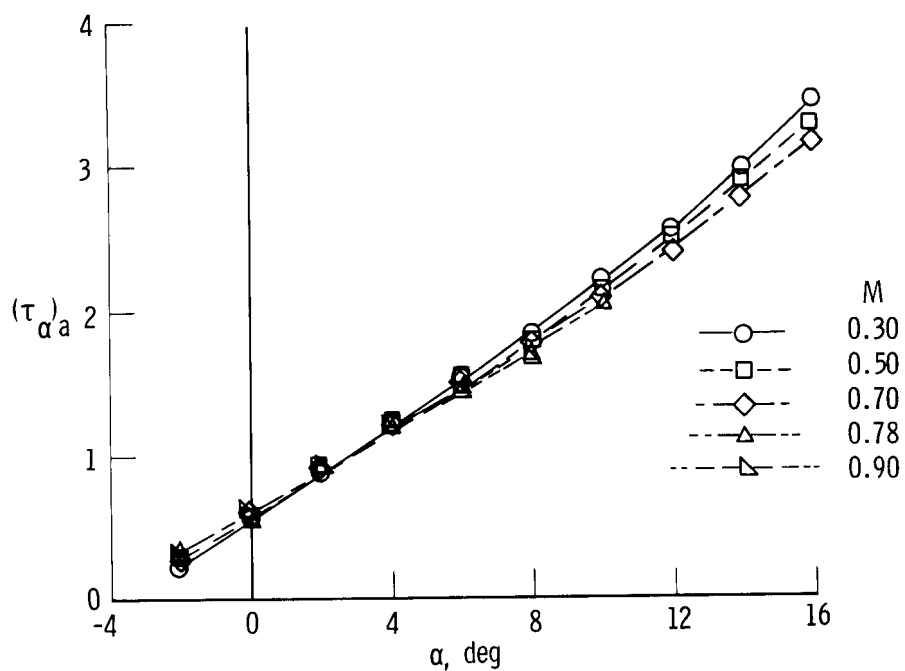


(a)  $\Delta p_\alpha = p_6 - p_{11}$ .

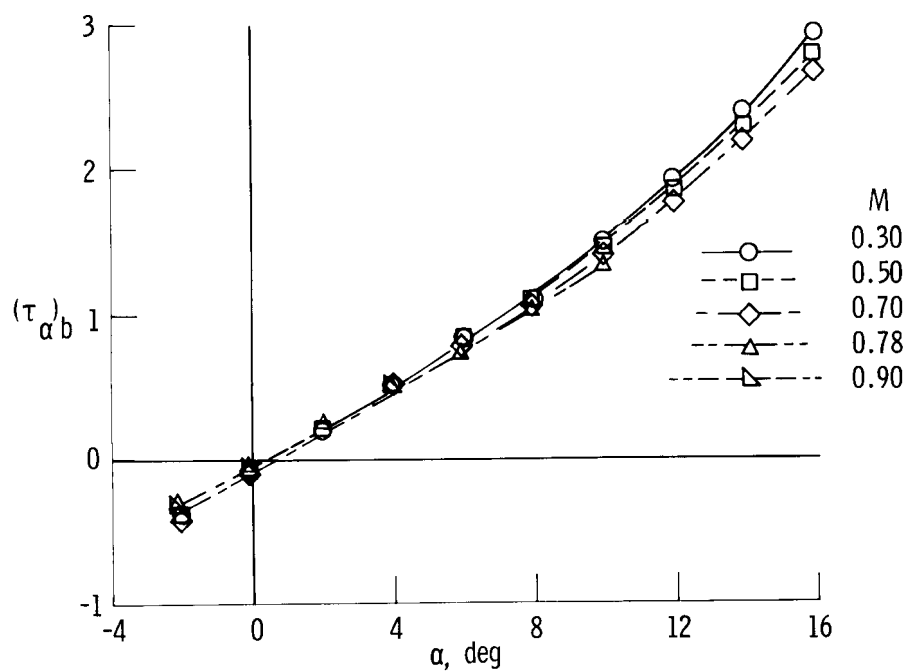


(b)  $\Delta p_\alpha = p_6 - p_{12}$ .

Figure 12. Angle of attack at which  $\Delta p_\alpha$  equals zero plotted against Mach number.

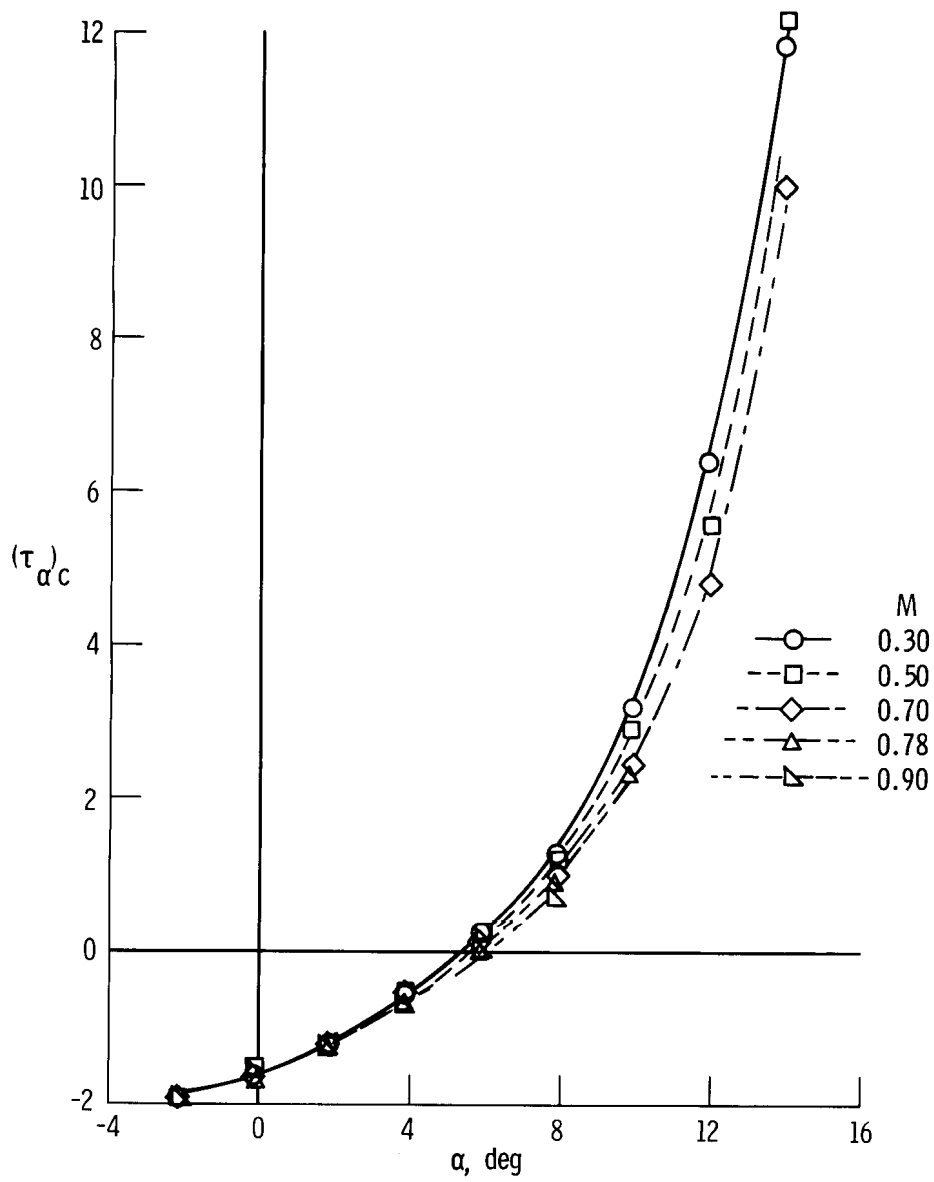


$$(a) \quad (\tau_\alpha)_a \cdot (\tau_\alpha)_a = \frac{p_{11} - p_3}{(p_6 - p_{11}) + 0.5(p_{11} - p_3)}.$$



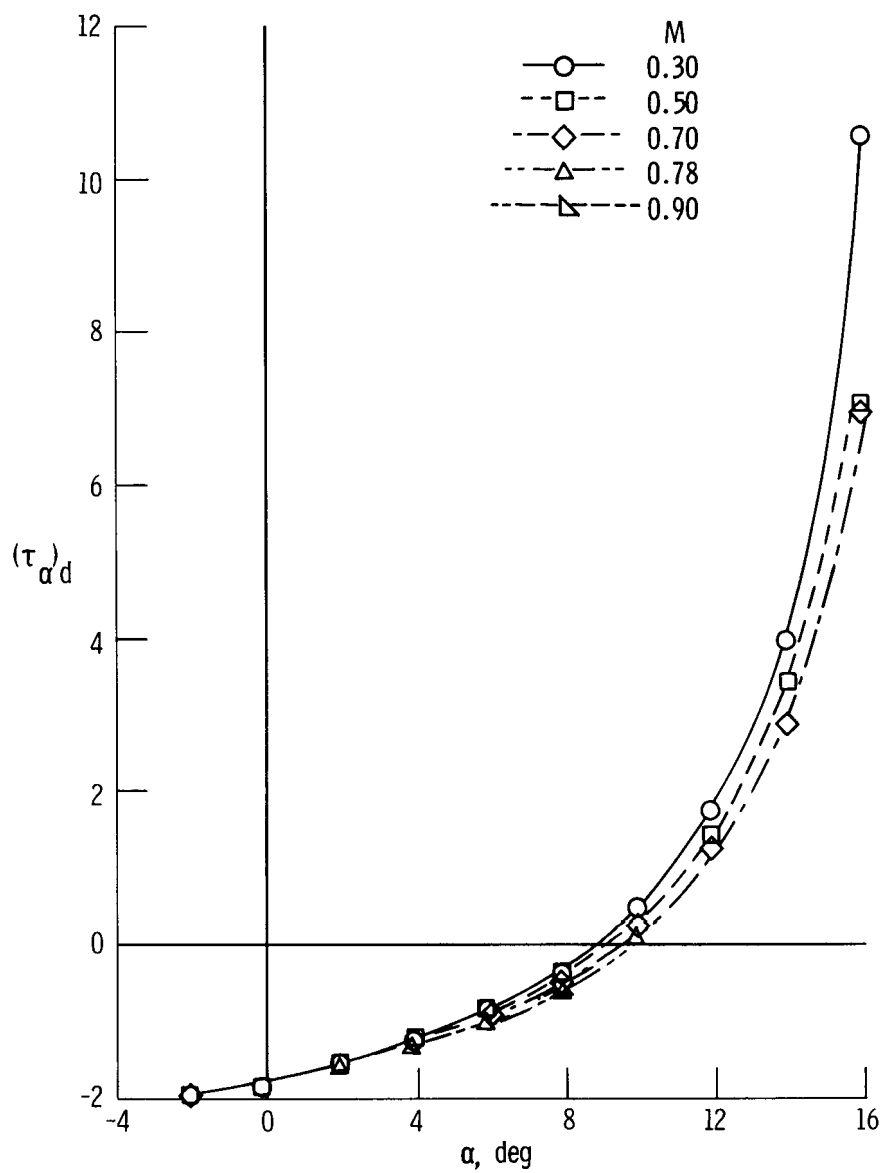
$$(b) \quad (\tau_\alpha)_b \cdot (\tau_\alpha)_b = \frac{p_{12} - p_3}{(p_6 - p_{12}) + 0.5(p_{12} - p_3)}.$$

Figure 13.  $\tau_\alpha$  pressure parameter plotted against angle of attack.  $\beta = 0^\circ$ .



$$(c) \quad (\tau_\alpha)_c \cdot (\tau_\alpha)_c = \frac{p_{11} - p_4}{(p_6 - p_{11}) + 0.5(p_{11} - p_4)}.$$

Figure 13. Continued.



$$(d) \quad (\tau_\alpha)_d \cdot (\tau_\alpha)_d = \frac{p_{12} - p_4}{(p_6 - p_{12}) + 0.5(p_{12} - p_4)}.$$

Figure 13. Concluded.



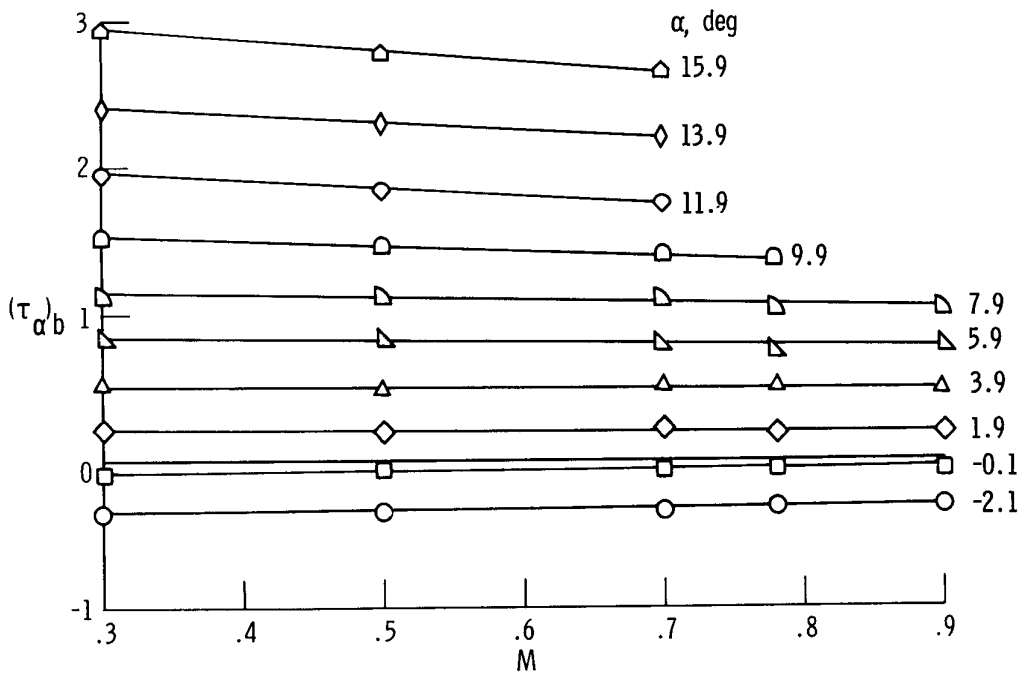
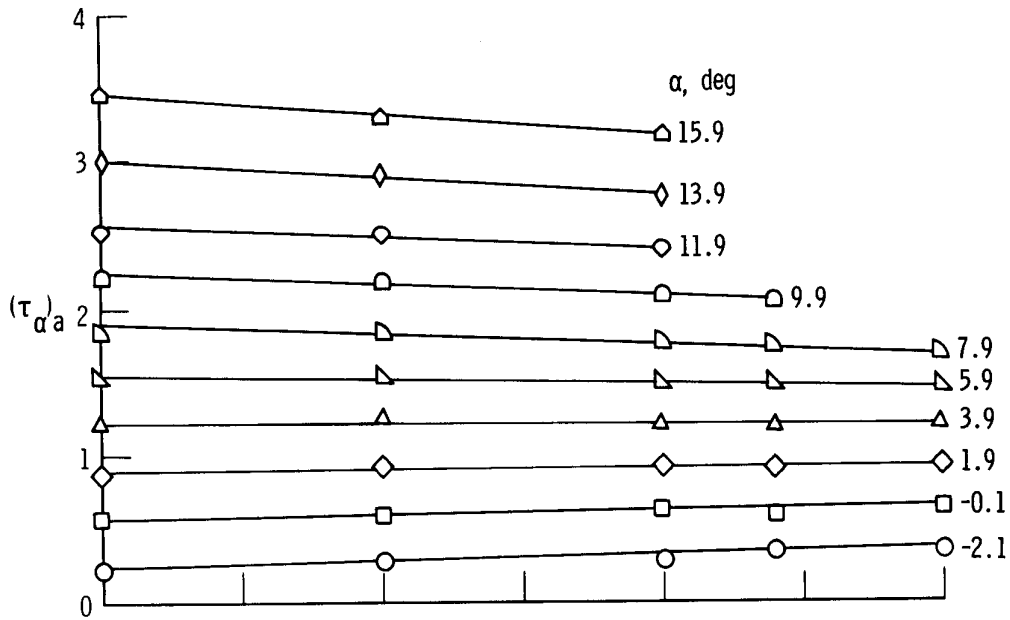


Figure 14.  $\tau_\alpha$  pressure parameters plotted against Mach number.  
 $\beta = 0^\circ$ .

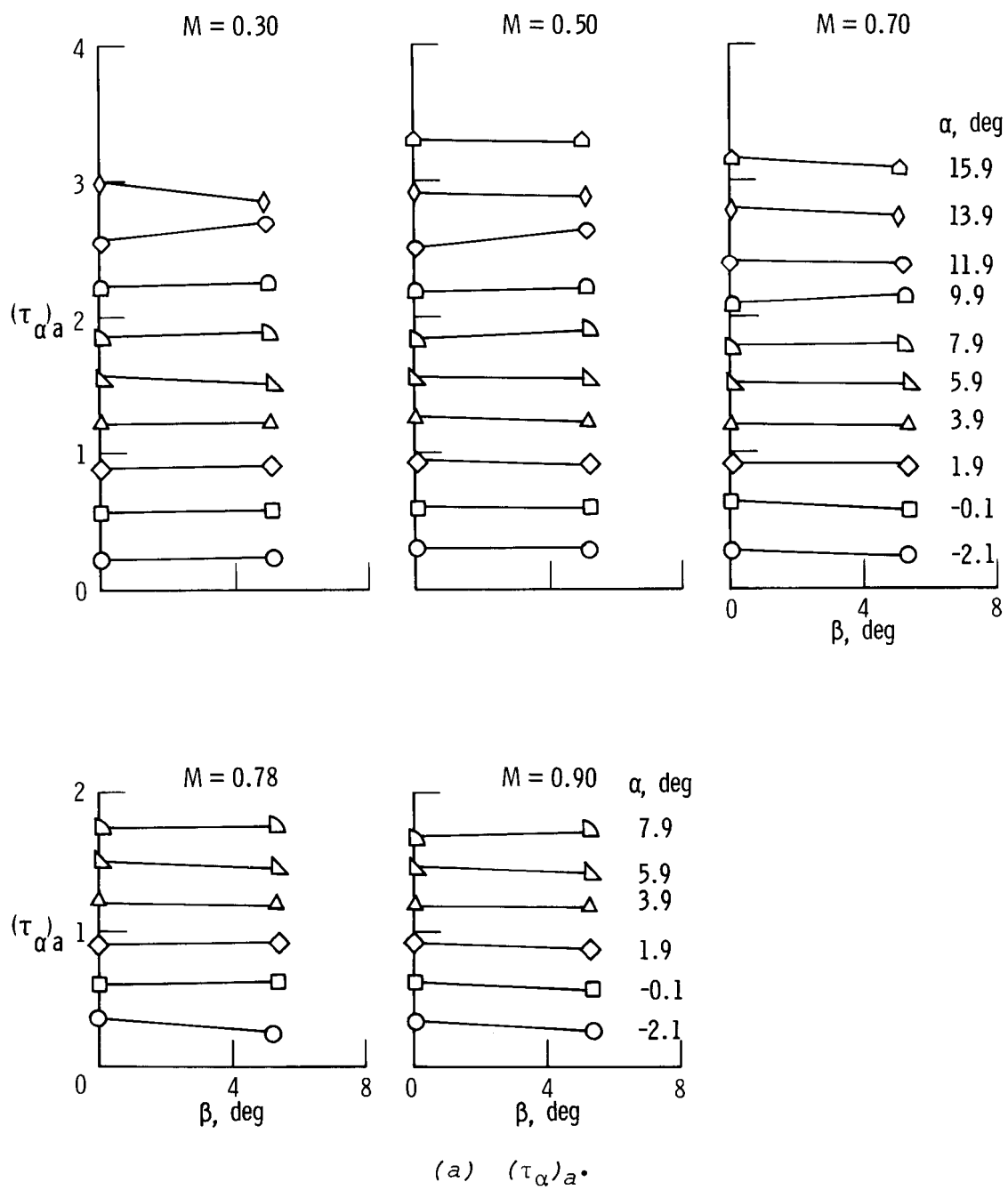
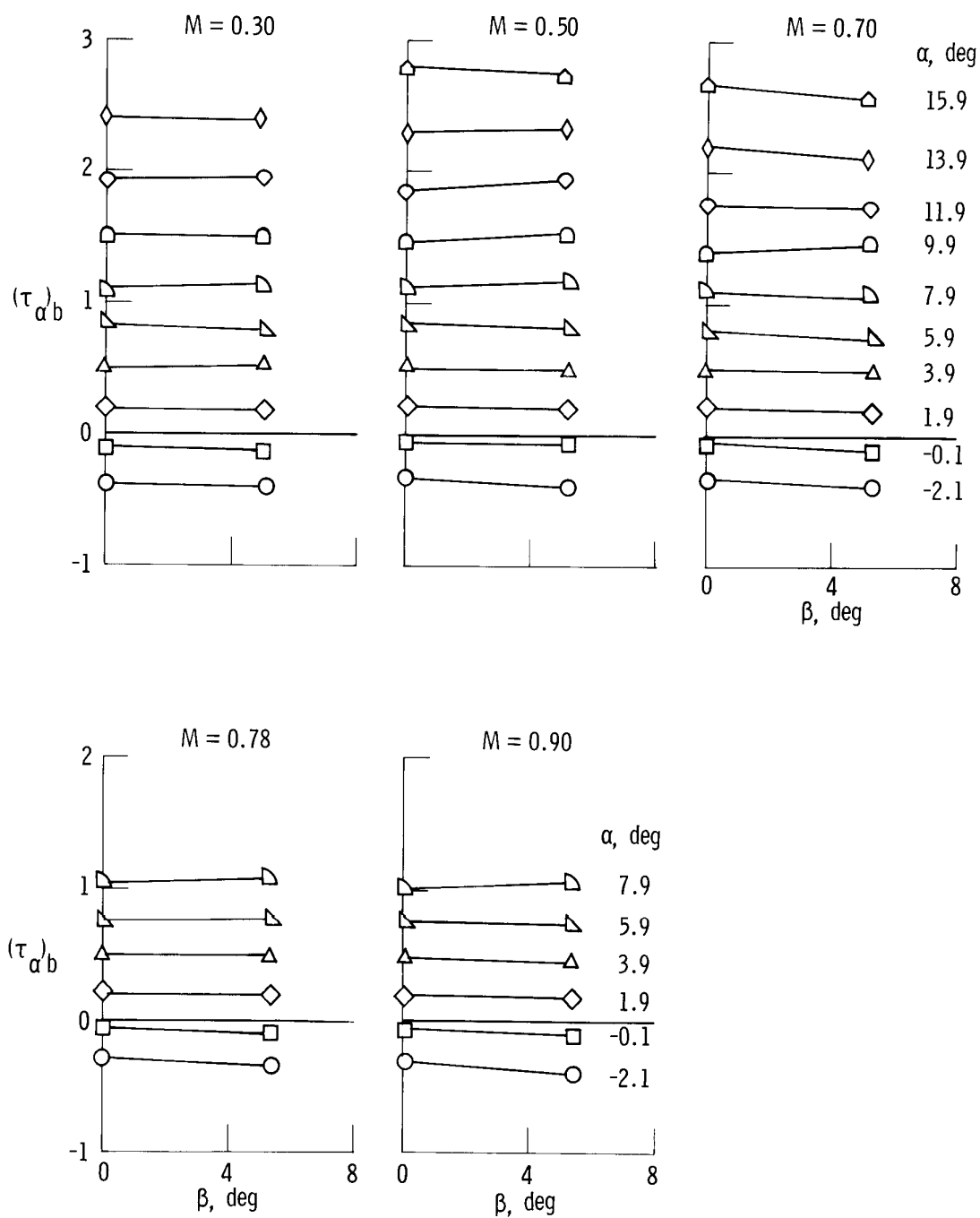
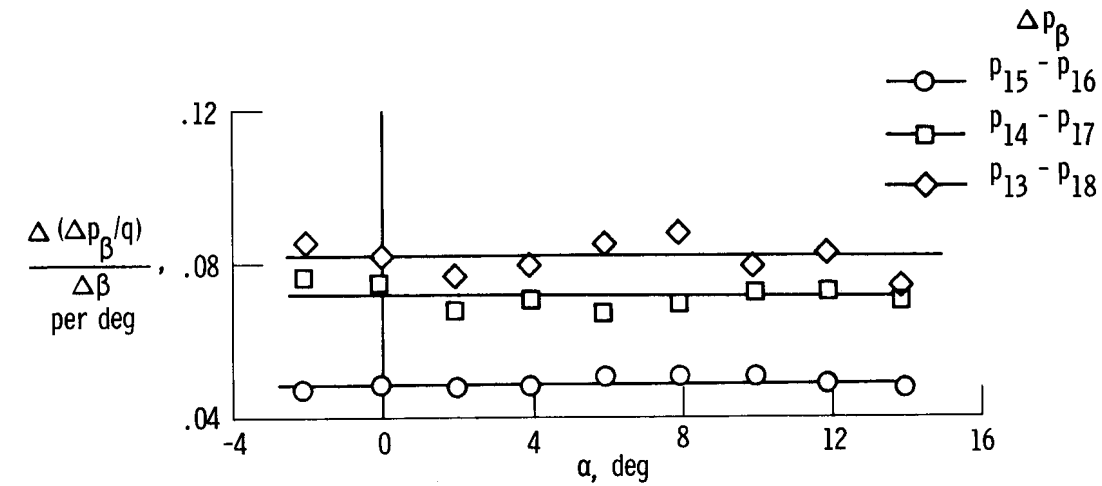


Figure 15.  $(\tau_\alpha)_a$  and  $(\tau_\alpha)_b$  plotted against angle of sideslip.

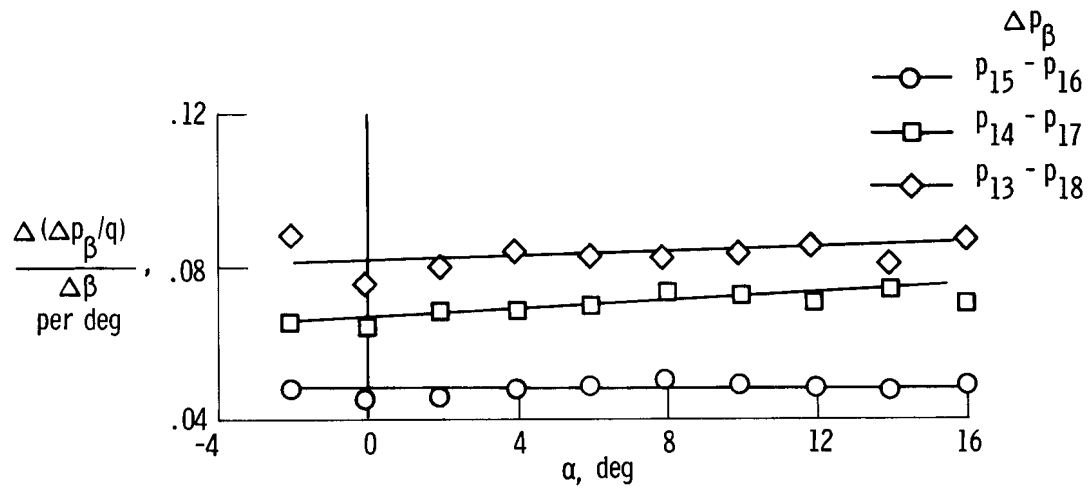


(b)  $(\tau_\alpha)_b$ .

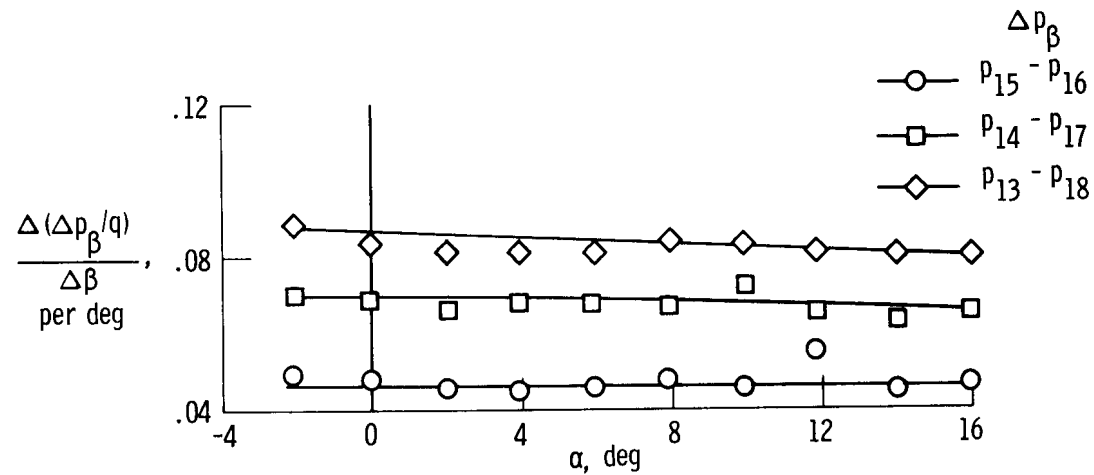
Figure 15. Concluded.



(a)  $M = 0.30$ .



(b)  $M = 0.50$ .



(c)  $M = 0.70$ .

Figure 16. Angle of sideslip parameter sensitivity for three pressure orifice pairs plotted against angle of attack.

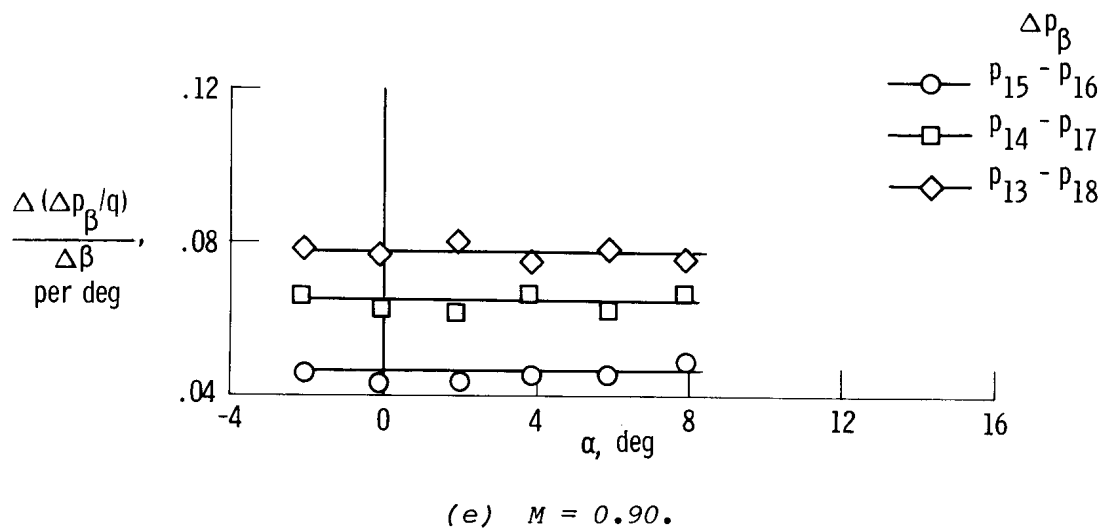
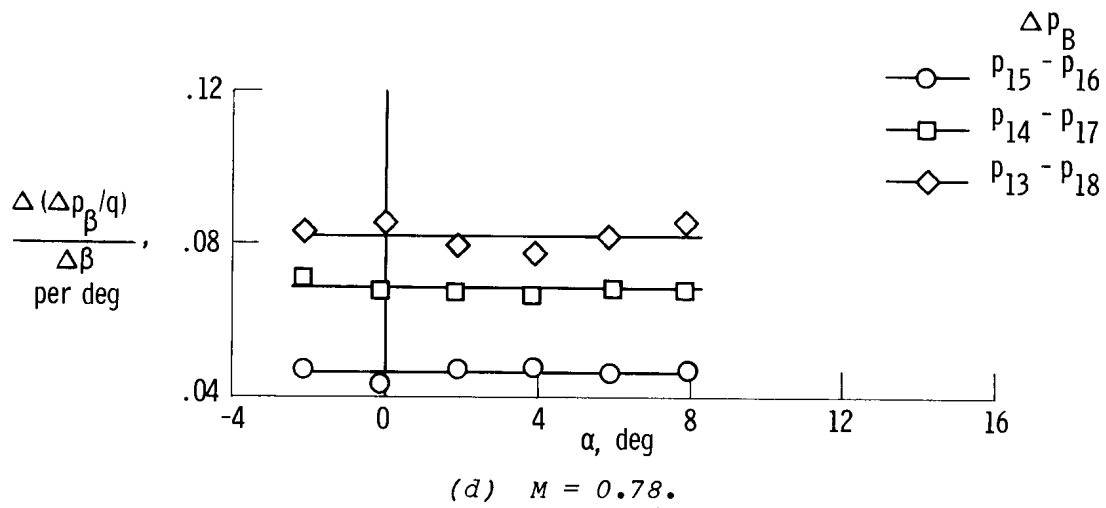
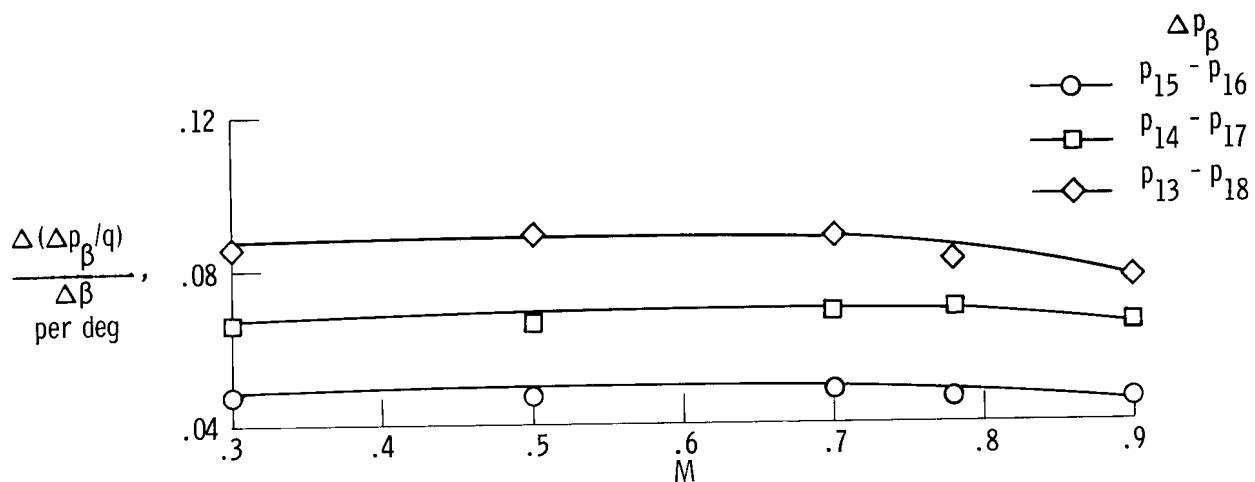
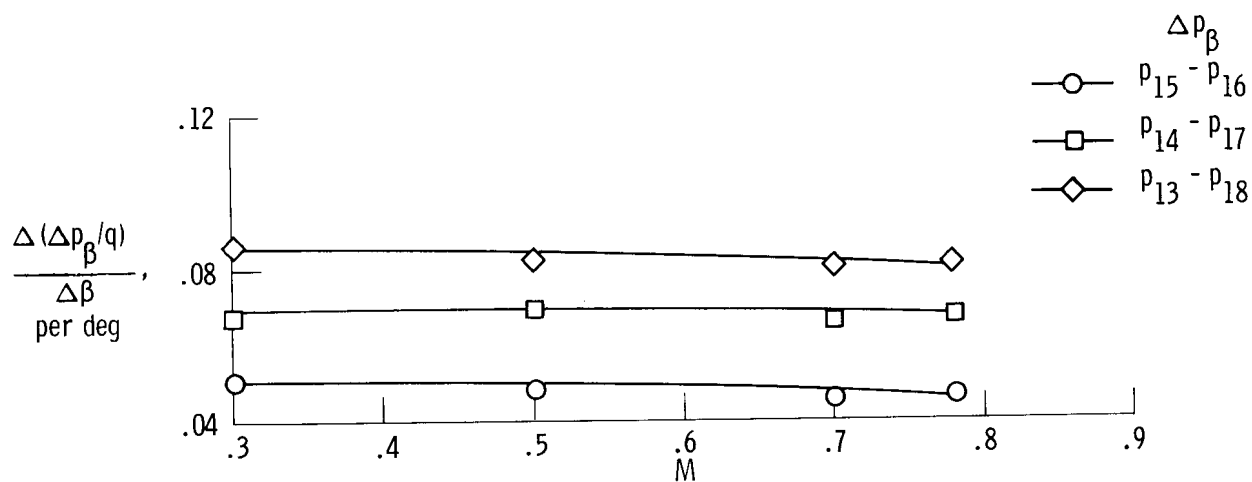


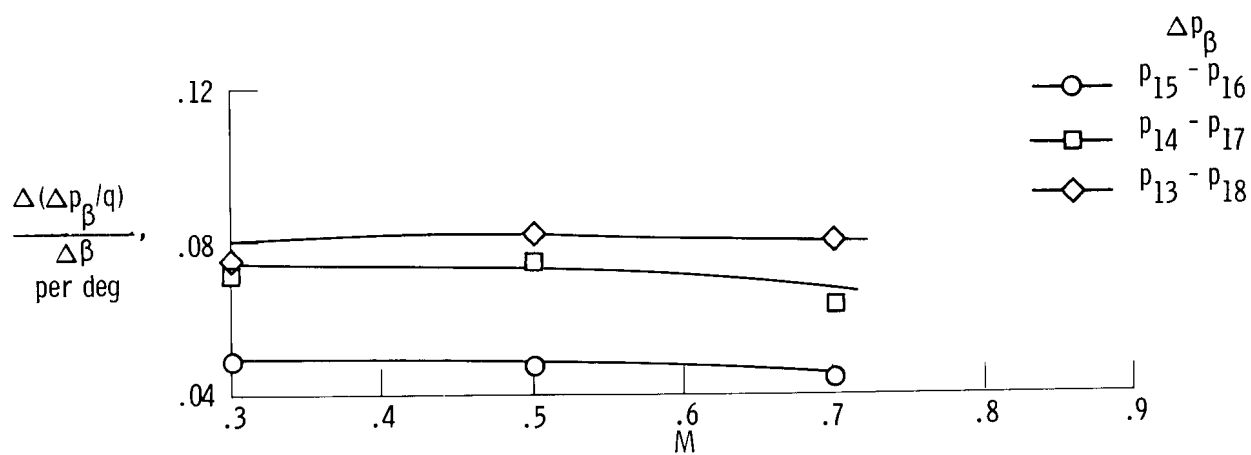
Figure 16. Concluded.



(a)  $\alpha = -2.1^\circ$ .



(b)  $\alpha = 5.9^\circ$ .



(c)  $\alpha = 13.9^\circ$ .

Figure 17. Angle of sideslip parameter sensitivity for three pressure orifice pairs plotted against Mach number.

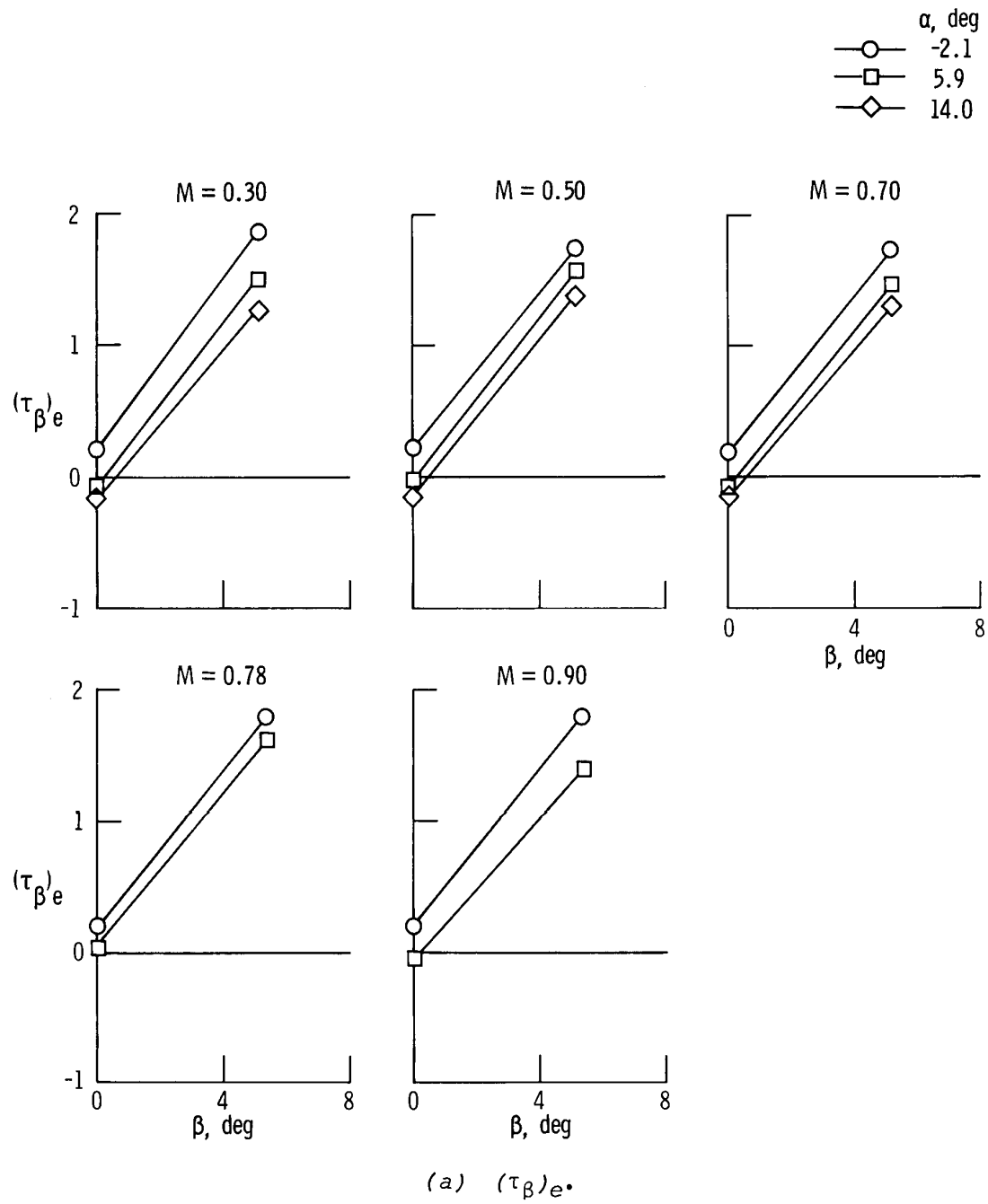
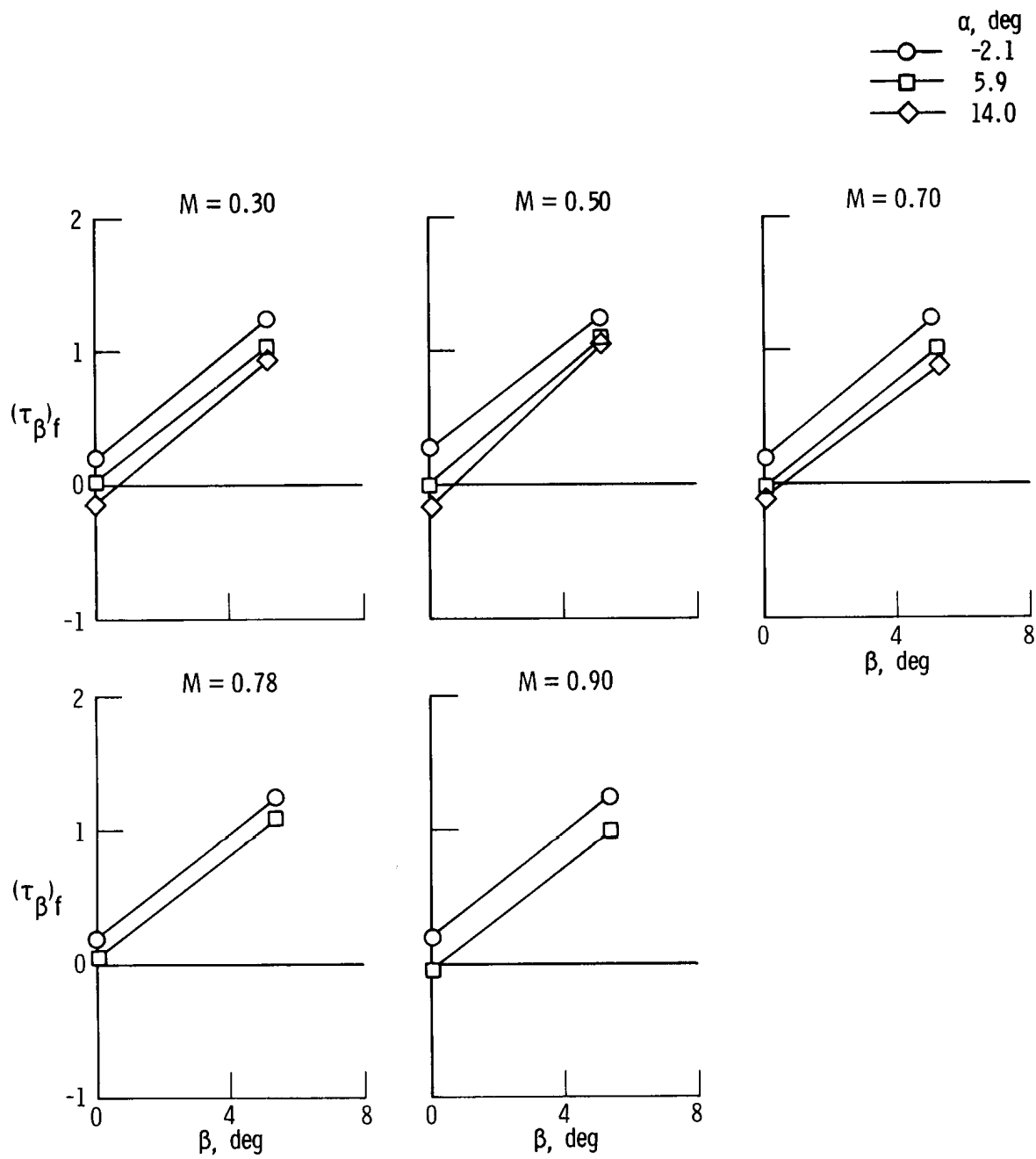


Figure 18.  $\tau_\beta$  parameters  $(\tau_\beta)_e$ ,  $(\tau_\beta)_f$ , and  $(\tau_\beta)_g$  plotted against angle of sideslip.



(b)  $(\tau_\beta)_f$ .

Figure 18. Continued.



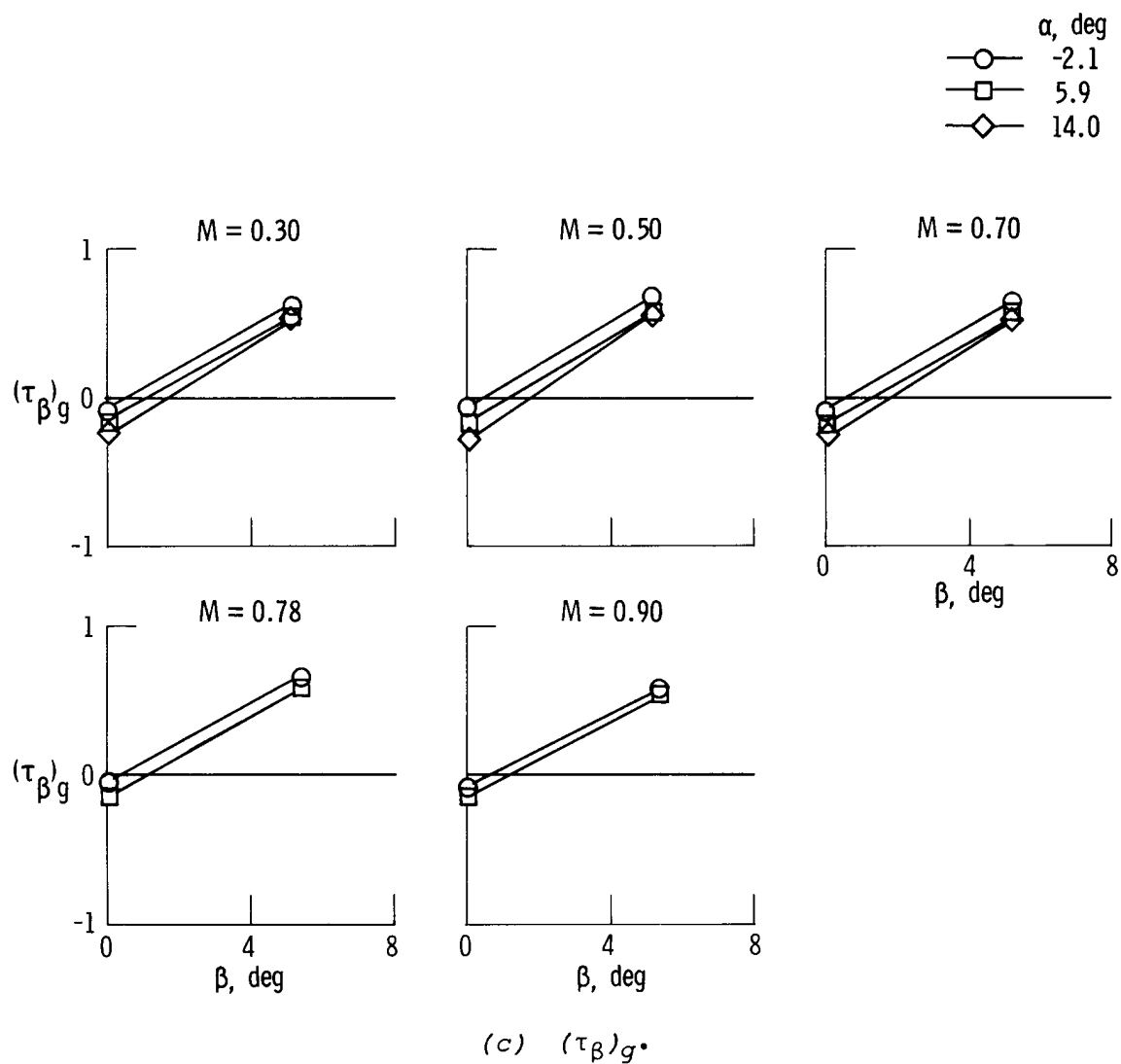
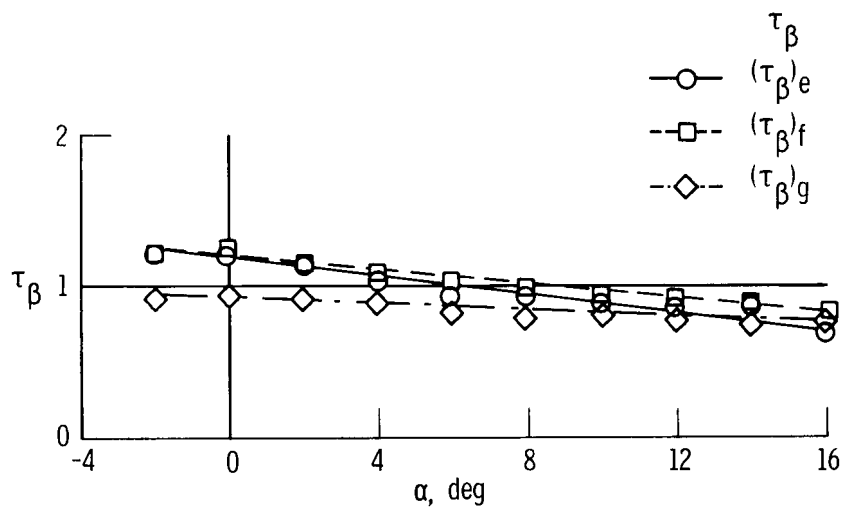
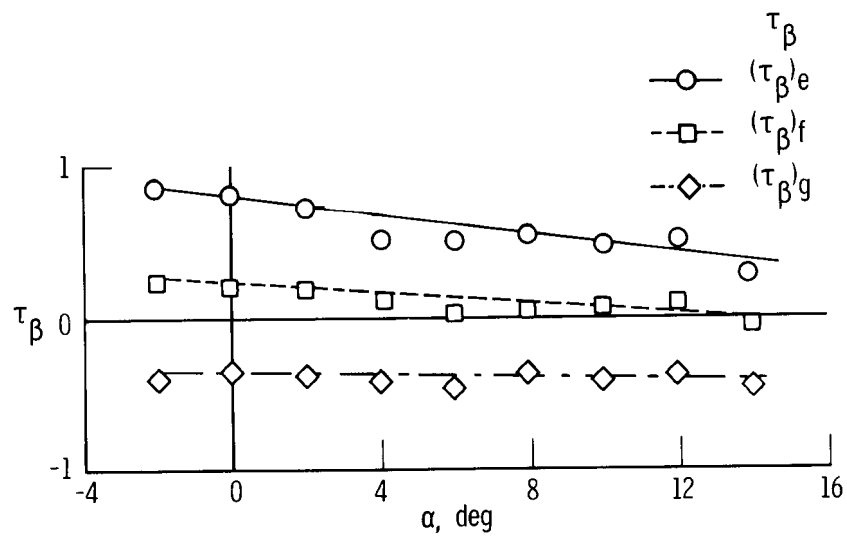


Figure 18. Concluded.

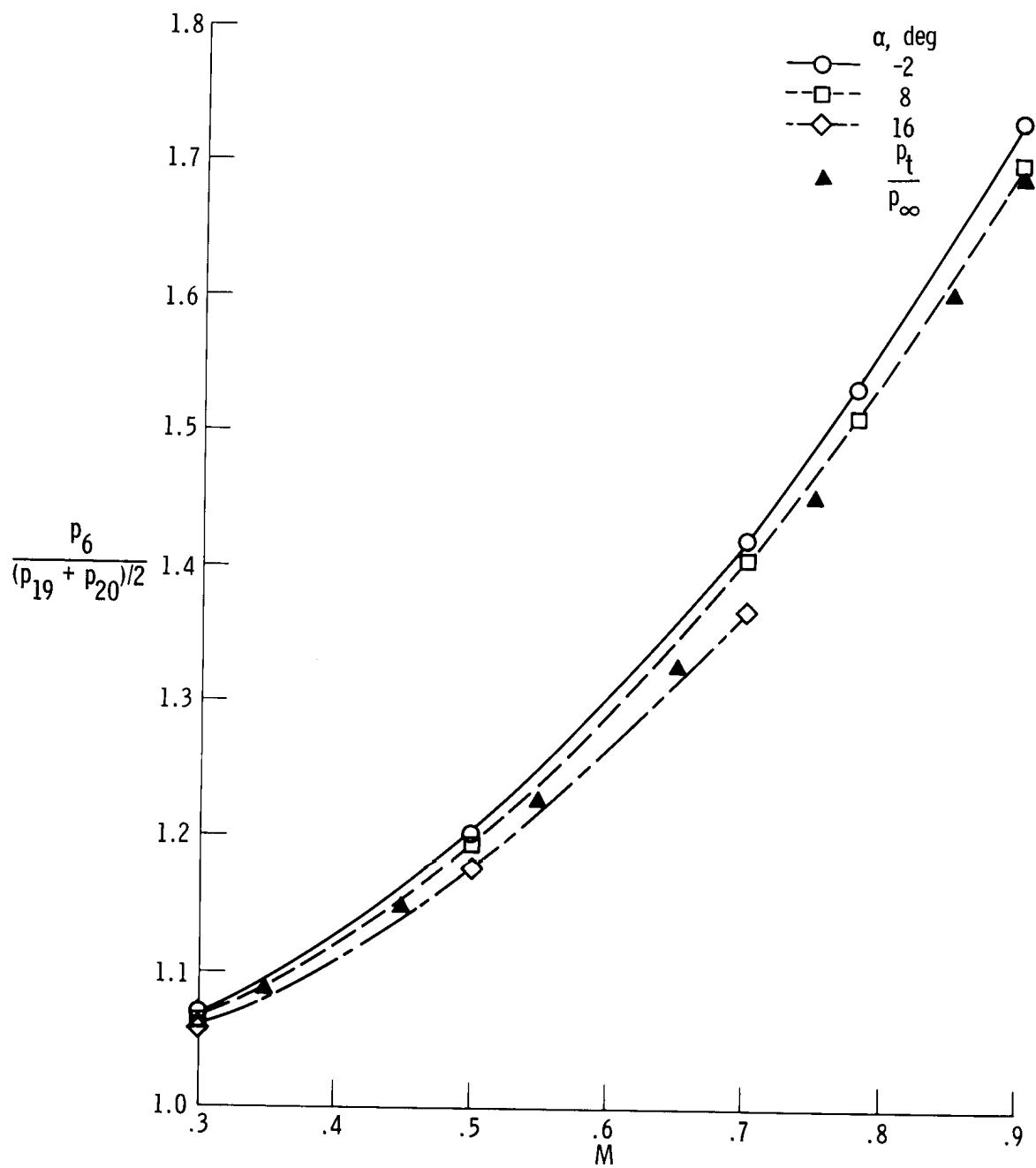


(a)  $\beta = 0^\circ$ .



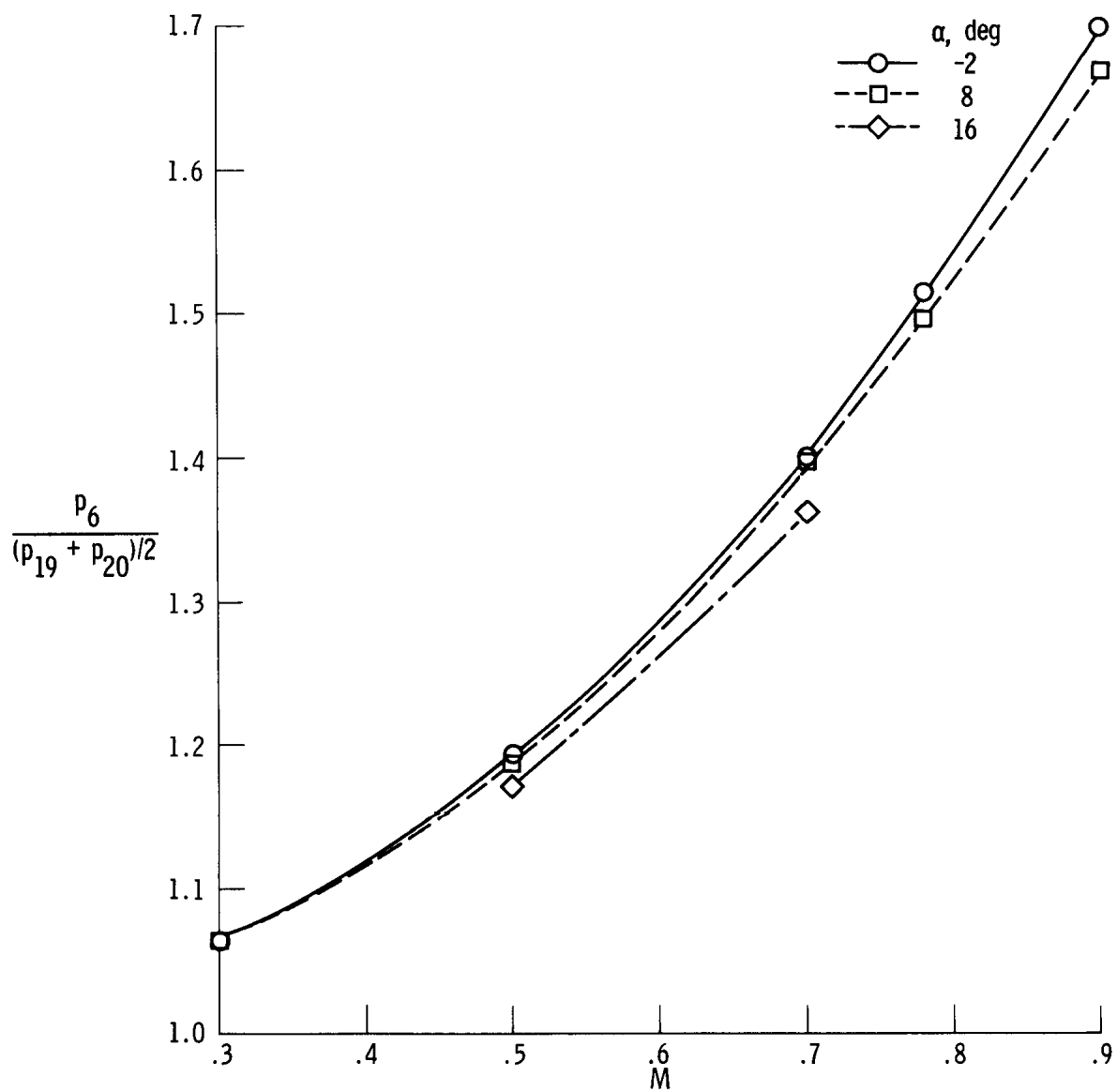
(b)  $\beta = 5^\circ$ .

Figure 19.  $\tau_\beta$  parameter plotted against angle of attack.  $M = 0.30$ .



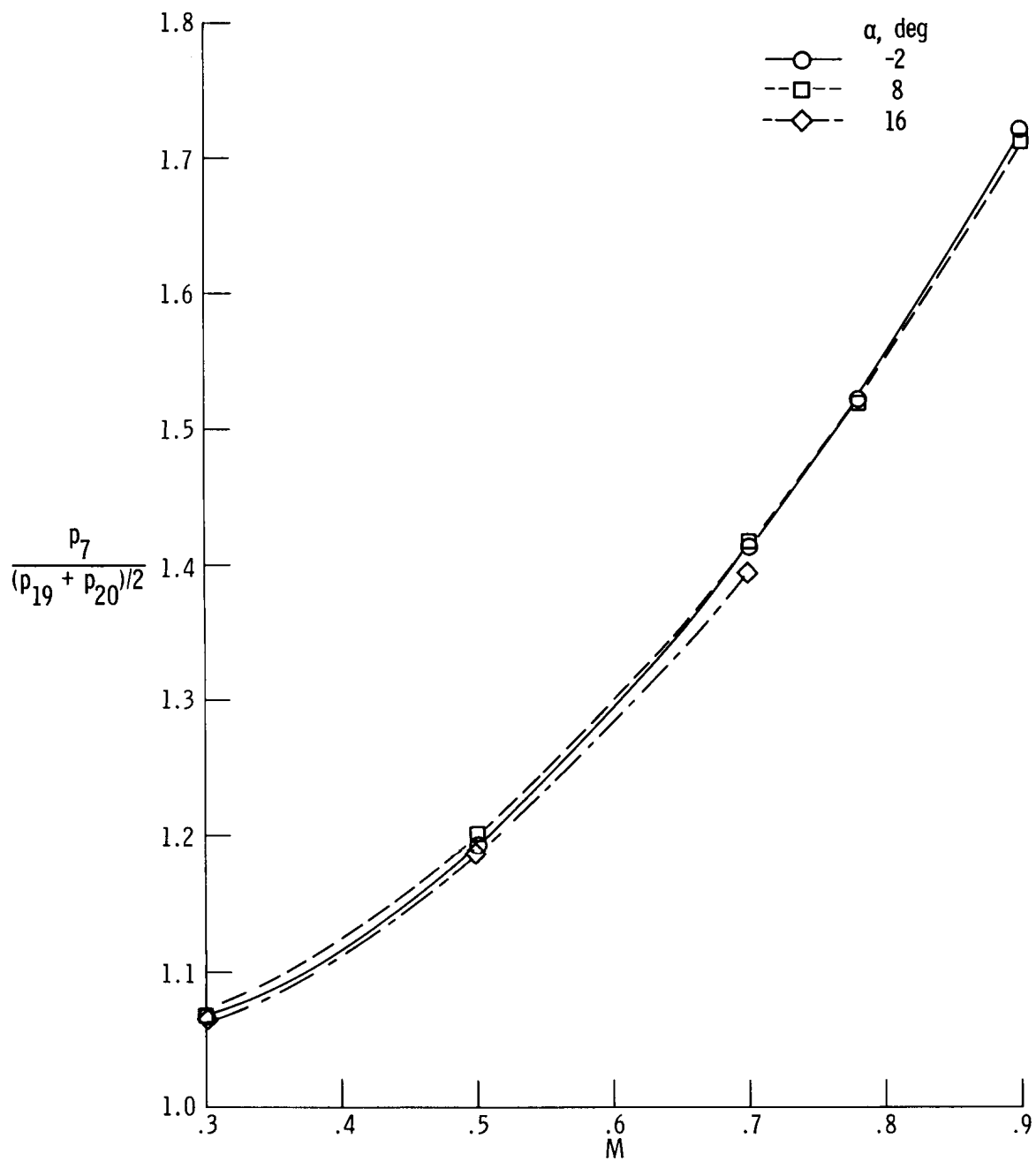
(a)  $\beta = 0^\circ$ .

Figure 20. Pressure ratio for determination of Mach number for a combination of nose and fuselage pressure orifices. Orifices 6, 19, and 20.



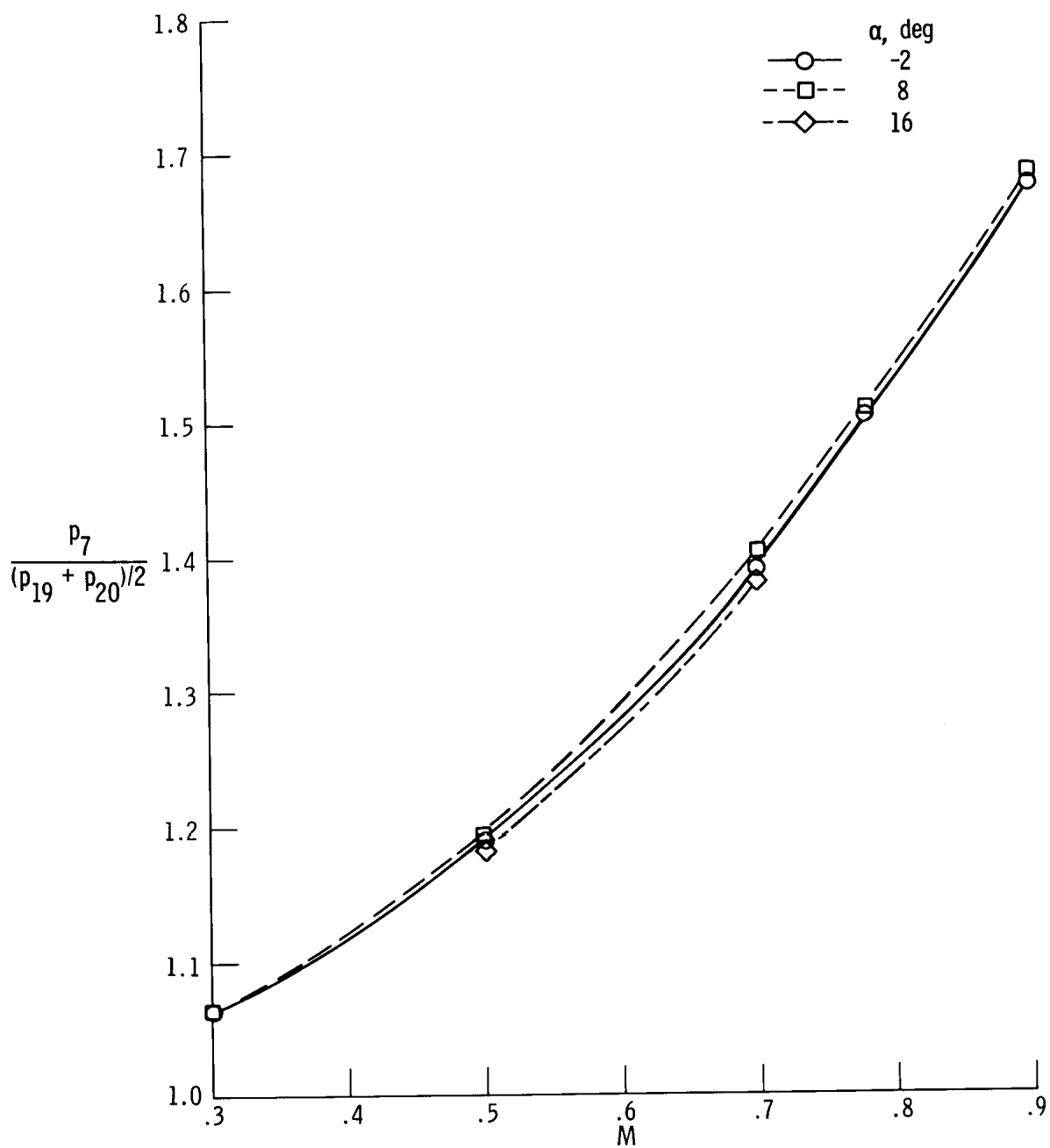
(b)  $\beta = 5^\circ$ .

Figure 20. Concluded.



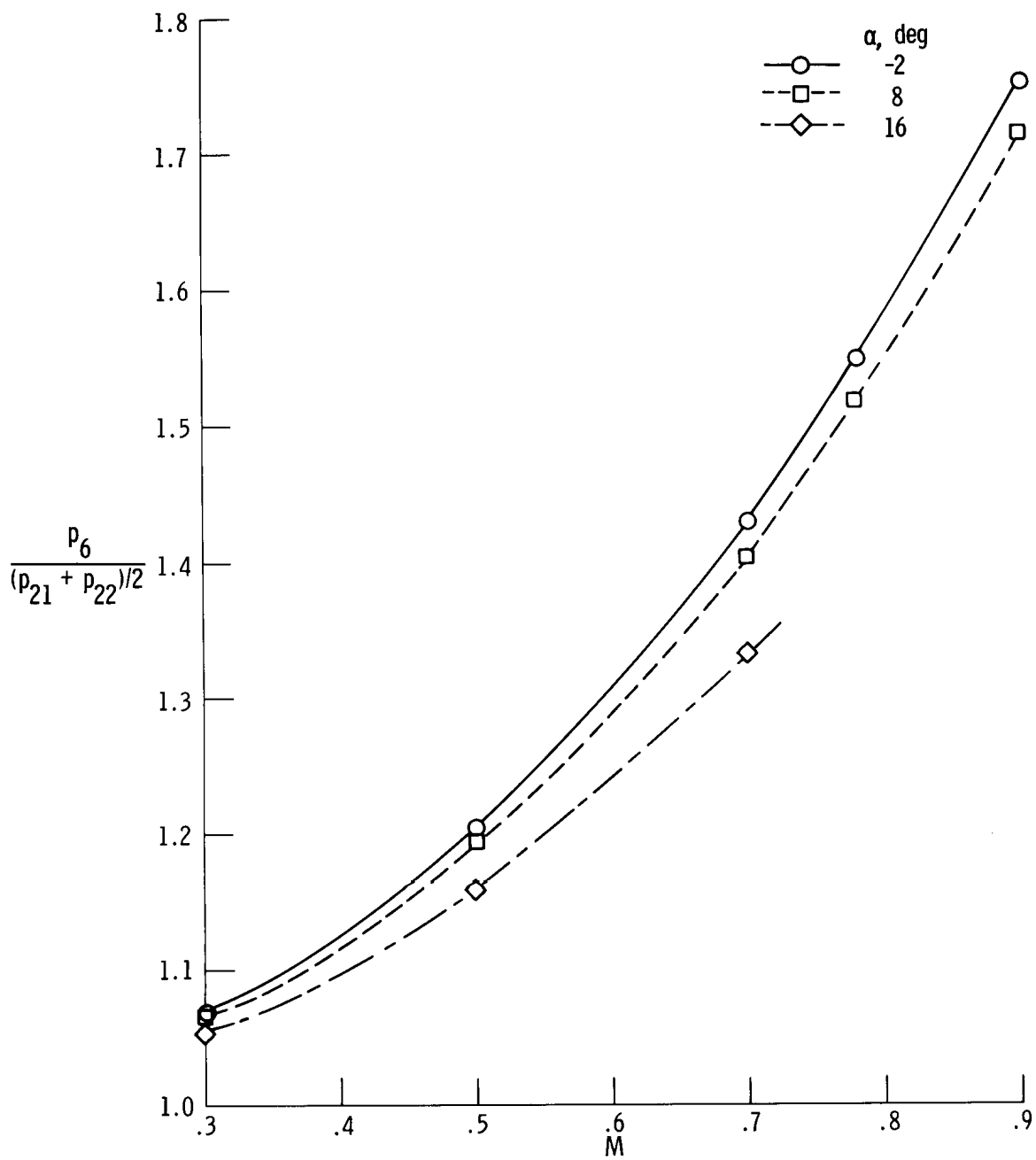
(a)  $\beta = 0^\circ$ .

Figure 21. Pressure ratio for determination of Mach number for a combination of nose and fuselage pressure orifices. Orifices 7, 19, and 20.



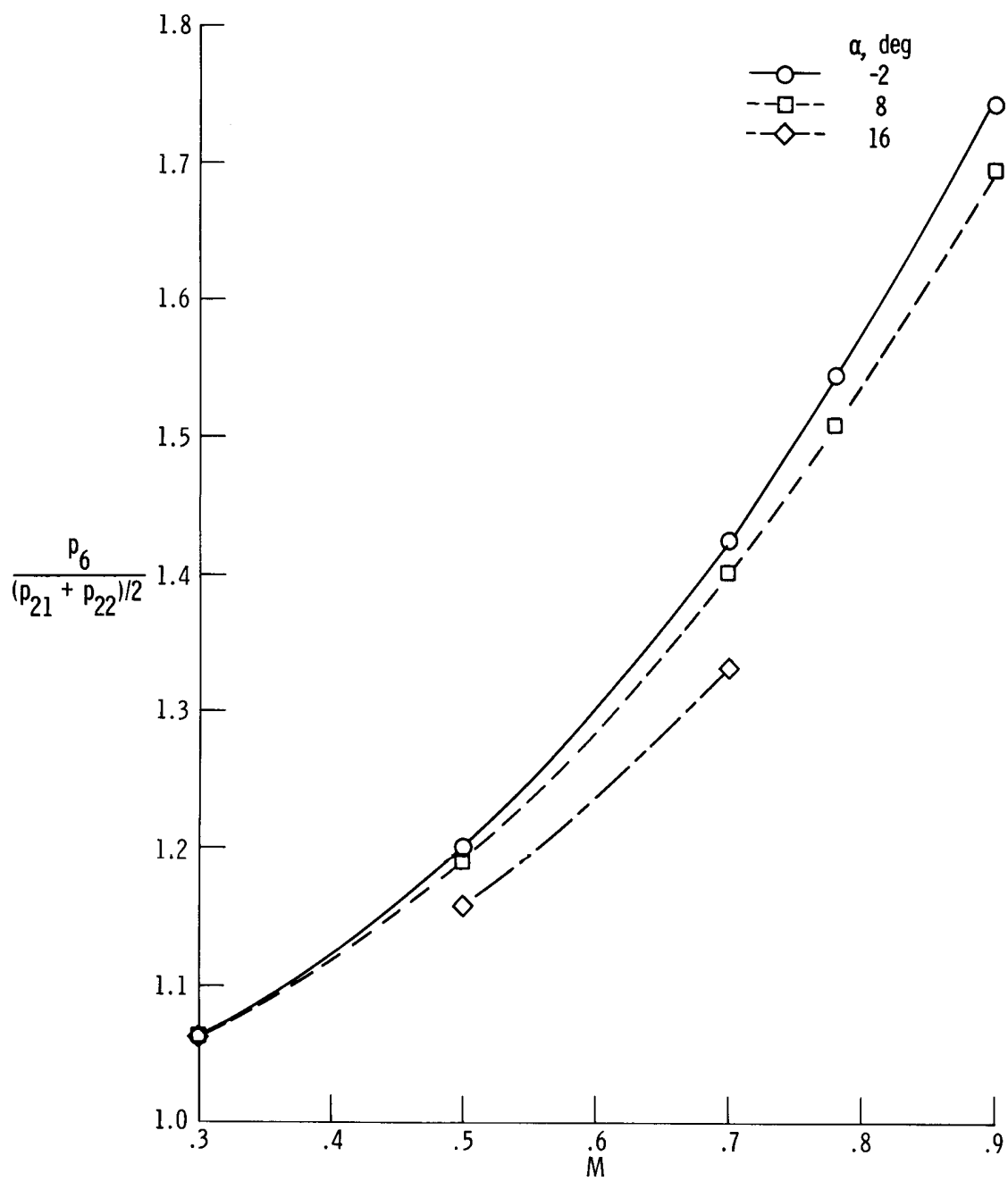
(b)  $\beta = 5^\circ$ .

Figure 21. Concluded.



(a)  $\beta = 0^\circ$ .

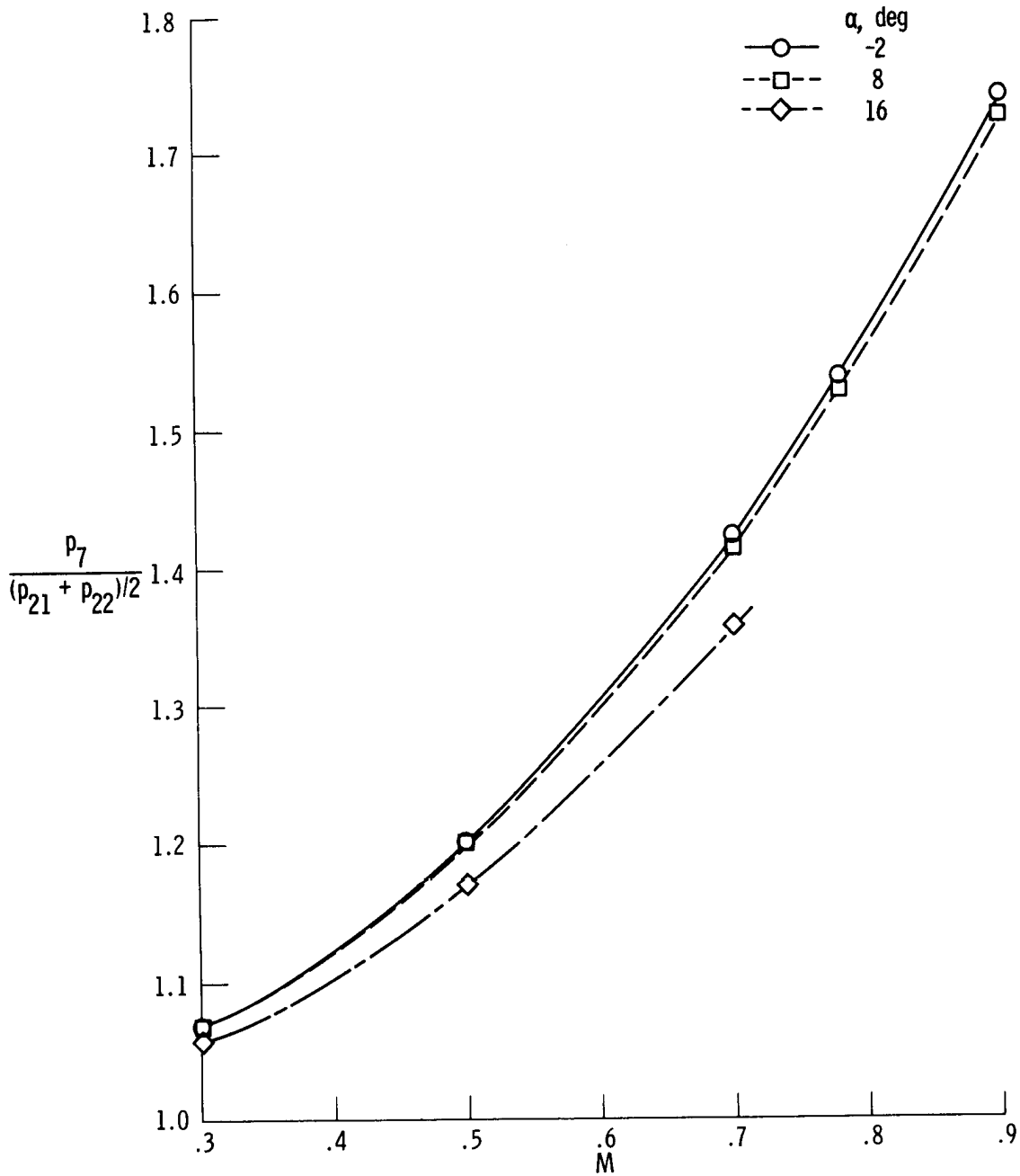
Figure 22. Pressure ratio for determination of Mach number for a combination of nose and fuselage pressure orifices. Orifices 6, 21, and 22.



(b)  $\beta = 5^\circ$ .

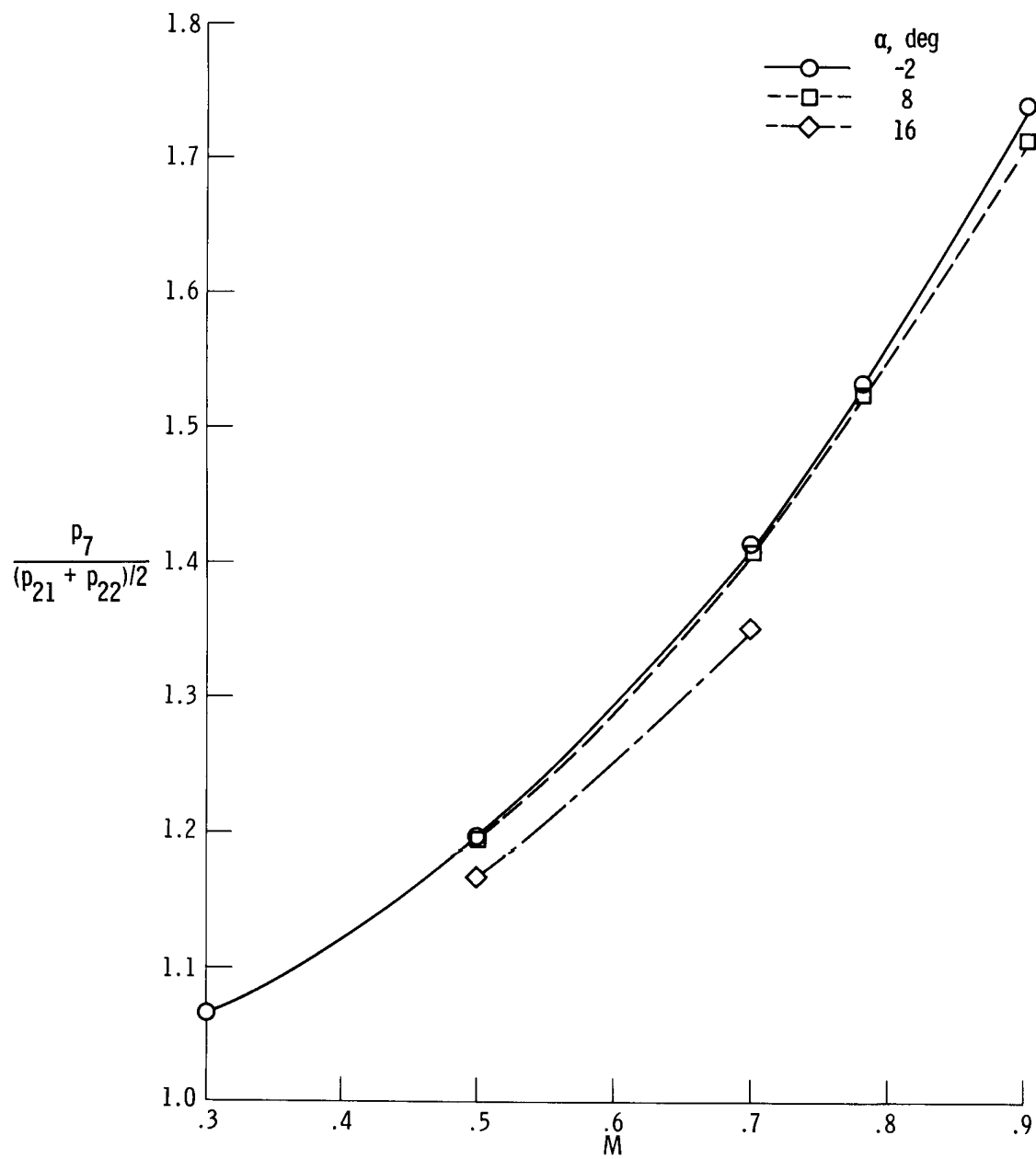
Figure 22. Concluded.





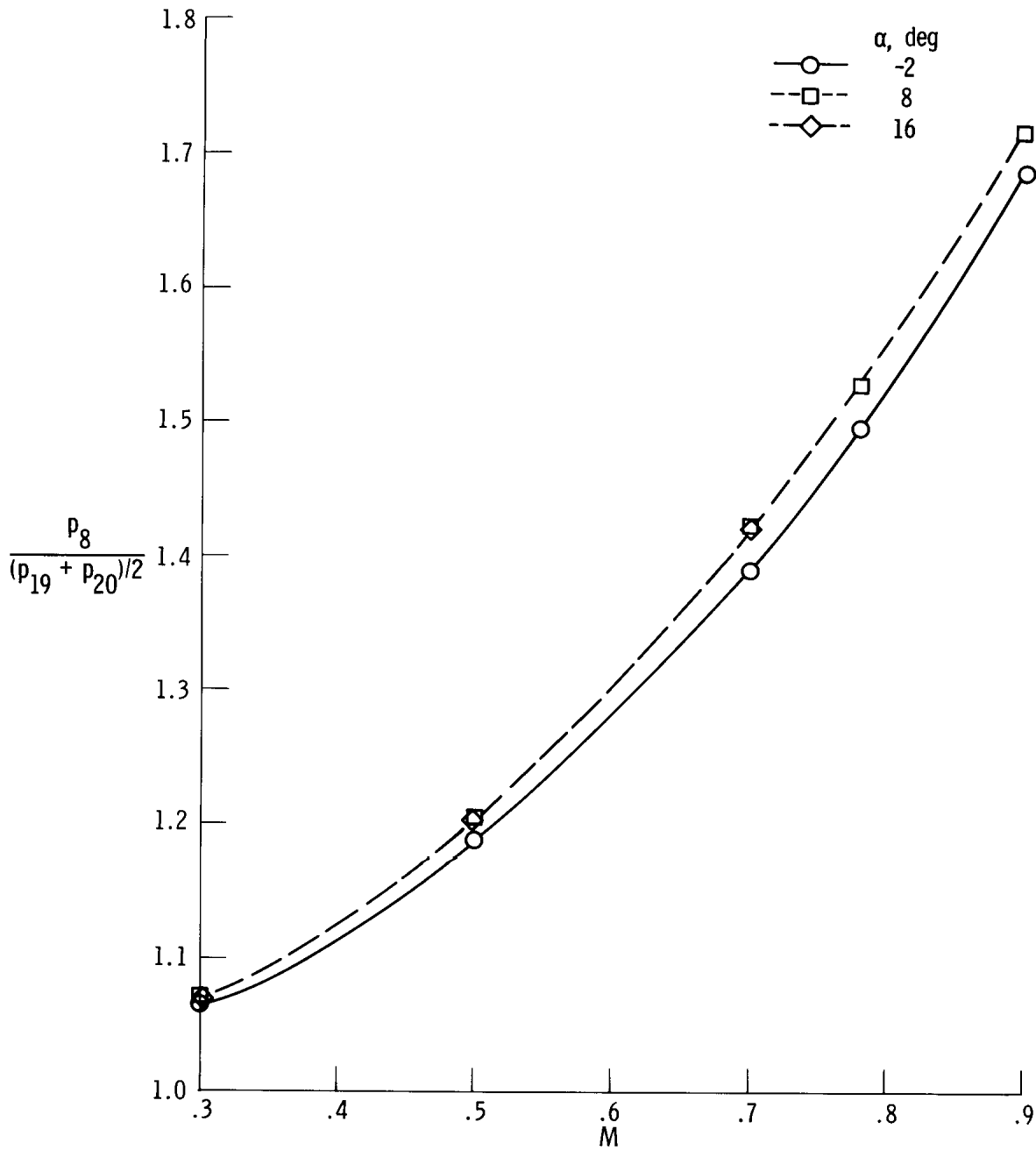
(a)  $\beta = 0^\circ$ .

Figure 23. Pressure ratio for determination of Mach number for a combination of nose and fuselage pressure orifices. Orifices 7, 21, and 22.



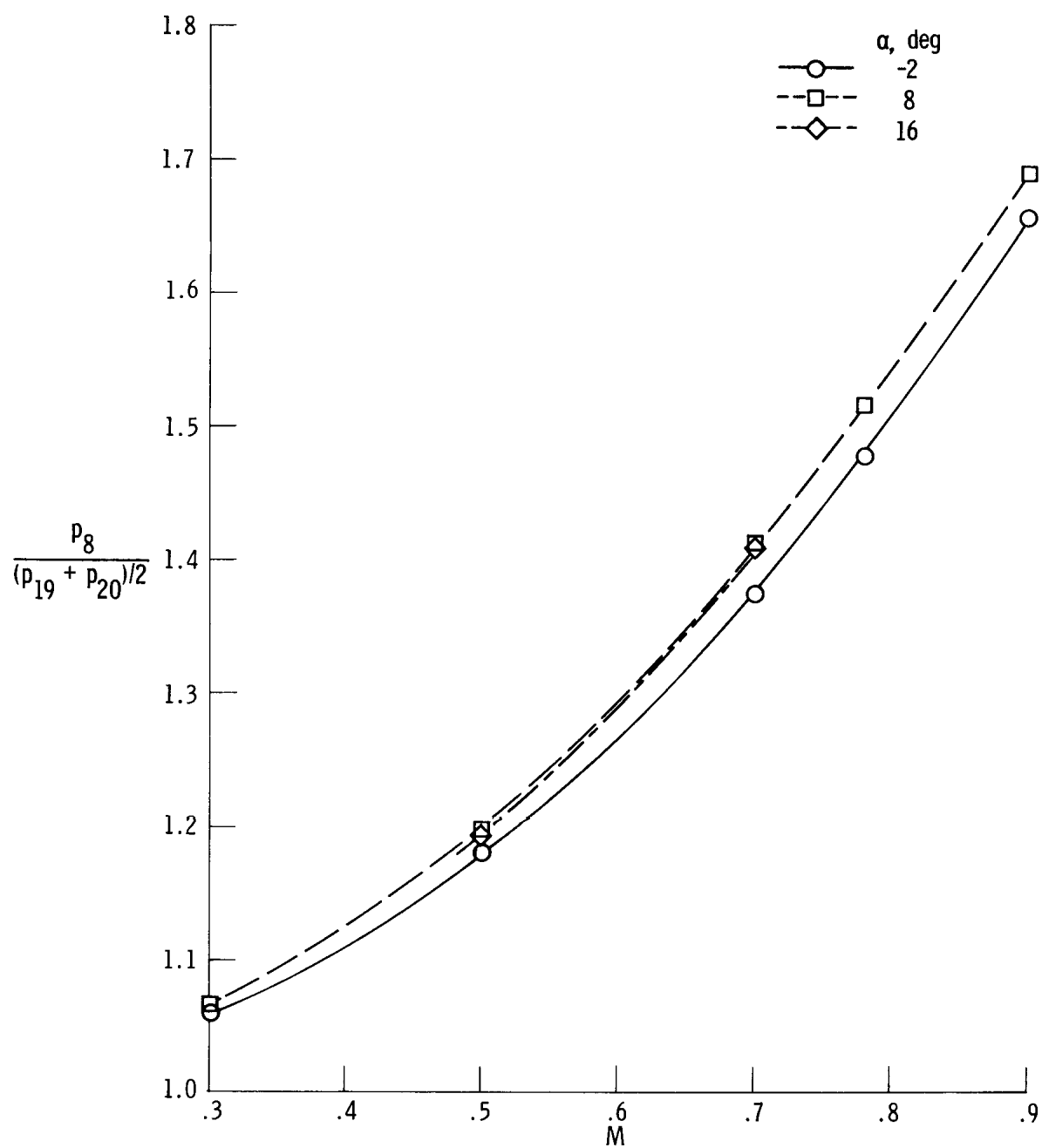
(b)  $\beta = 5^\circ$ .

Figure 23. Concluded.



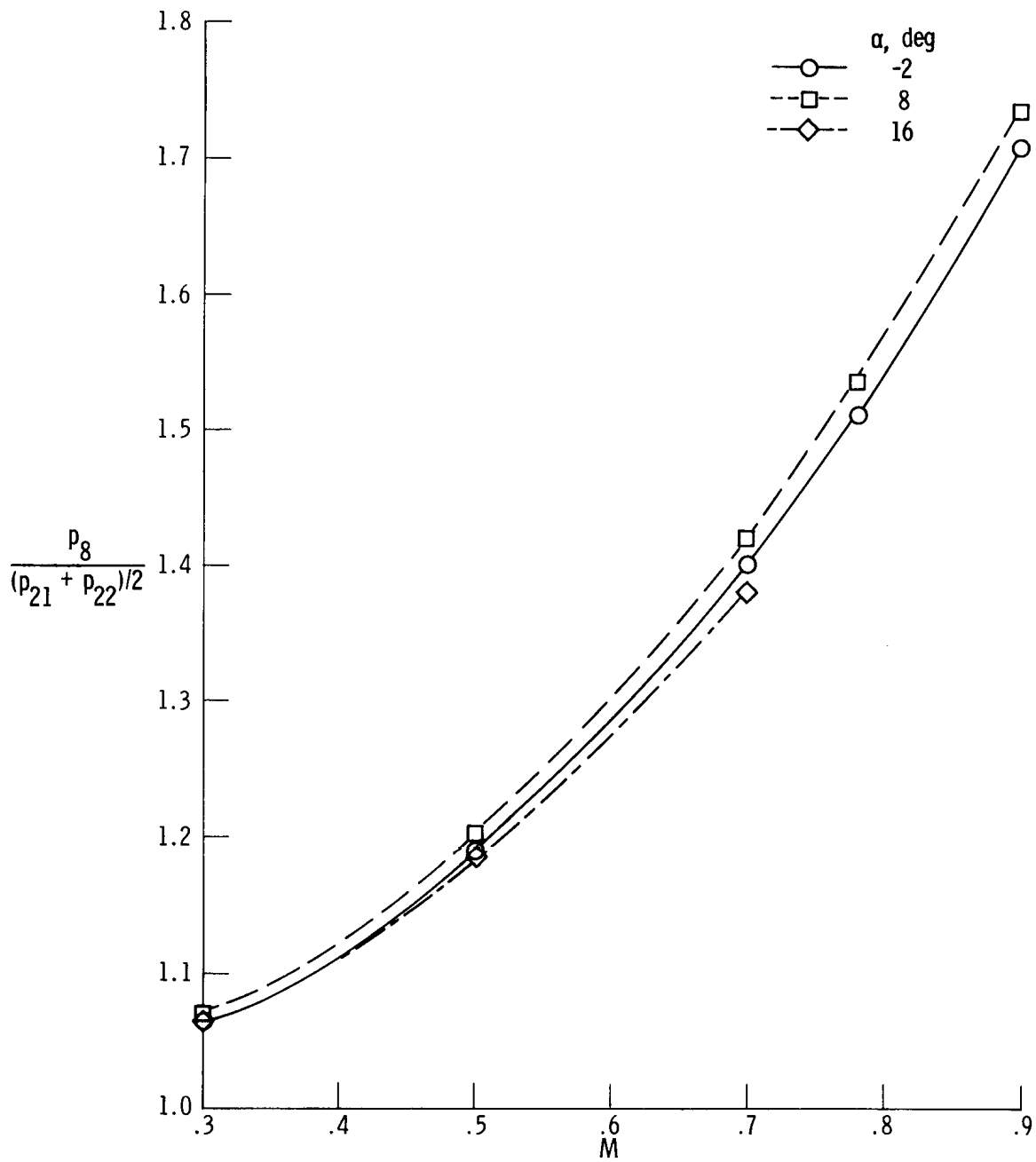
(a)  $\beta = 0^\circ$ .

Figure 24. Pressure ratio for determination of Mach number for a combination of nose and fuselage pressure orifices. Orifices 8, 19, and 20.



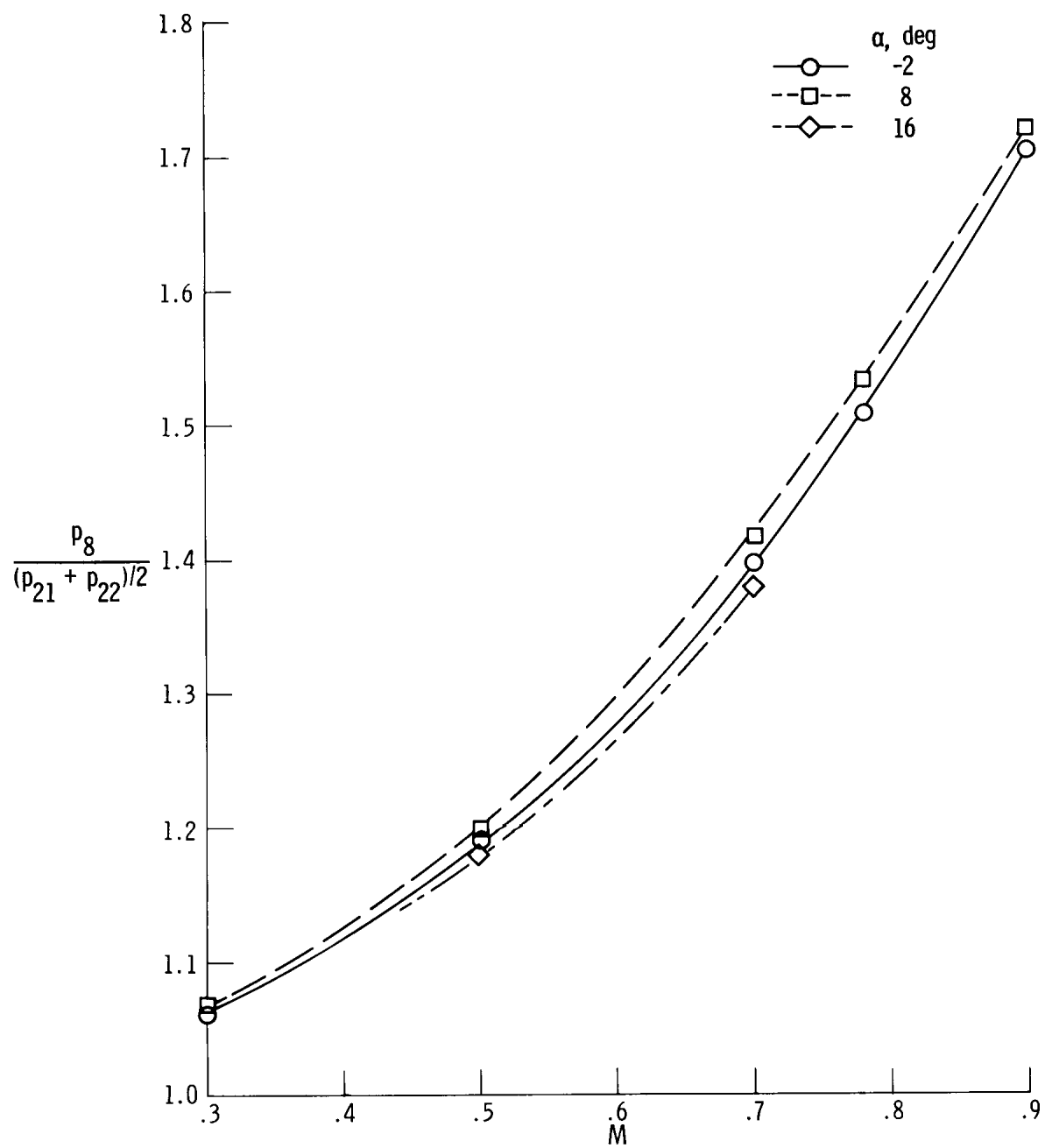
(b)  $\beta = 5^\circ$ .

Figure 24. Concluded.



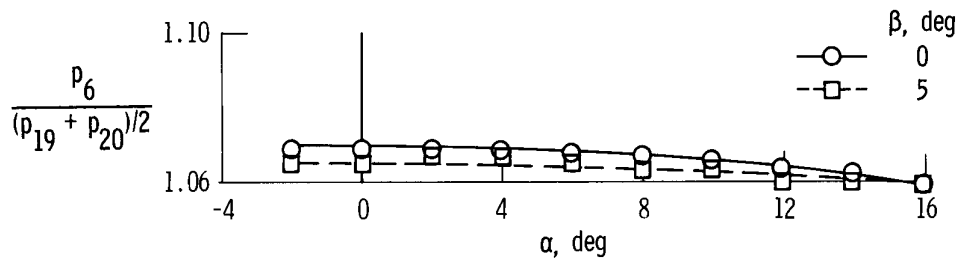
(a)  $\beta = 0^\circ$ .

Figure 25. Pressure ratio for determination of Mach number for a combination of nose and fuselage pressure orifices. Orifices 8, 21, and 22.

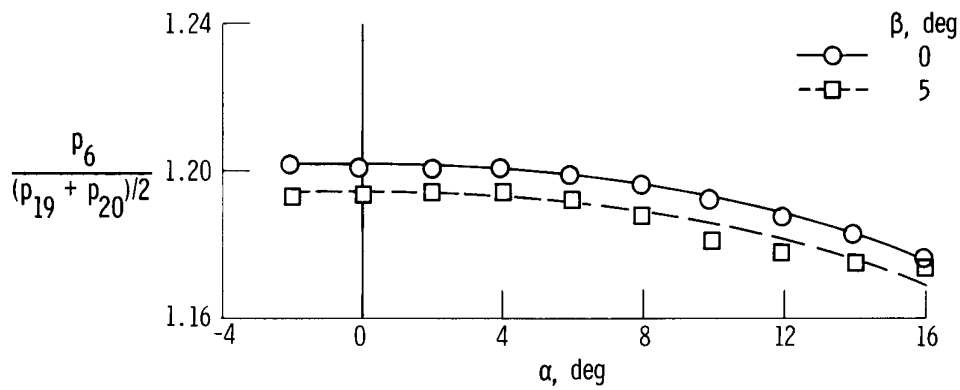


(b)  $\beta = 5^\circ$ .

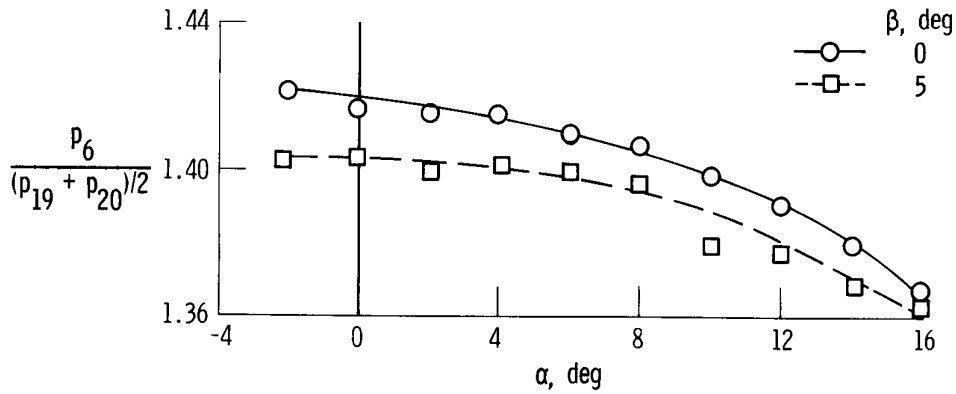
Figure 25. Concluded.



(a)  $M = 0.30$ .

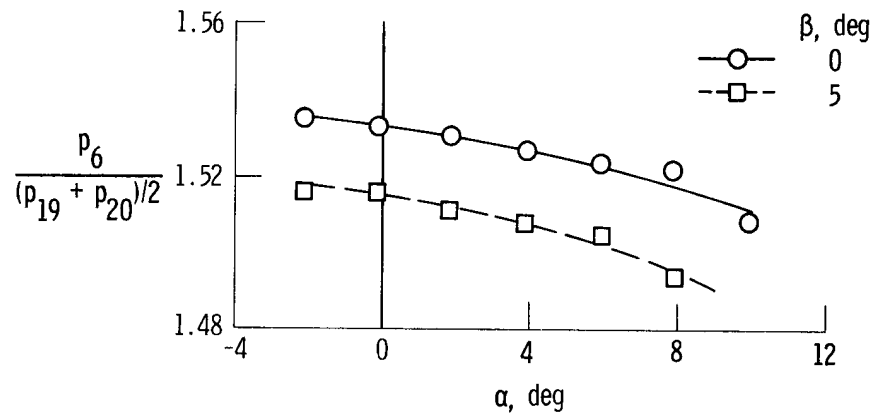


(b)  $M = 0.50$ .

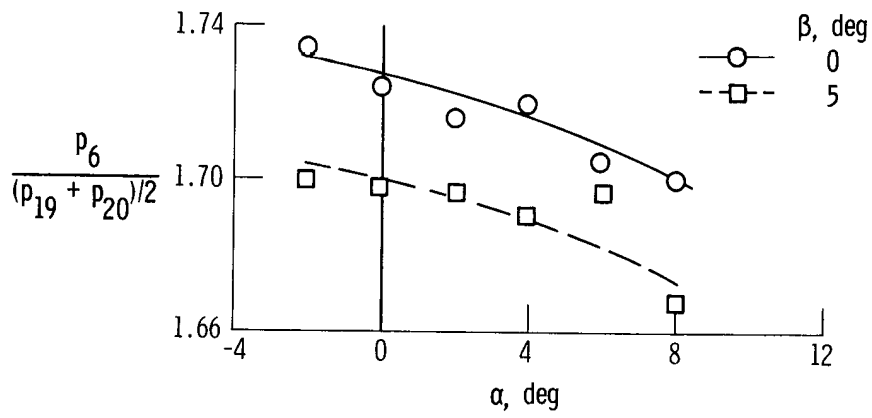


(c)  $M = 0.70$ .

Figure 26. Pressure ratio for determination of Mach number plotted against angle of attack using a combination of nose and fuselage orifices. Orifices 6, 19, and 20.



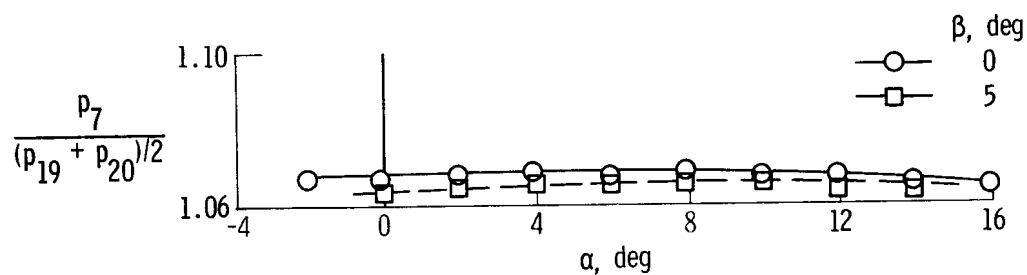
(d)  $M = 0.78$ .



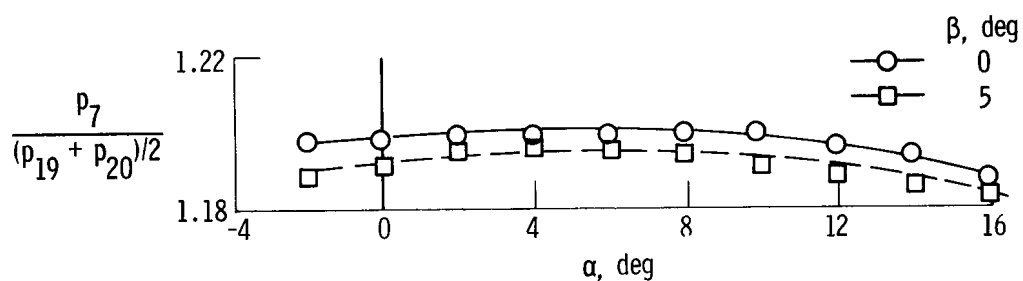
(e)  $M = 0.90$ .

Figure 26. Concluded.

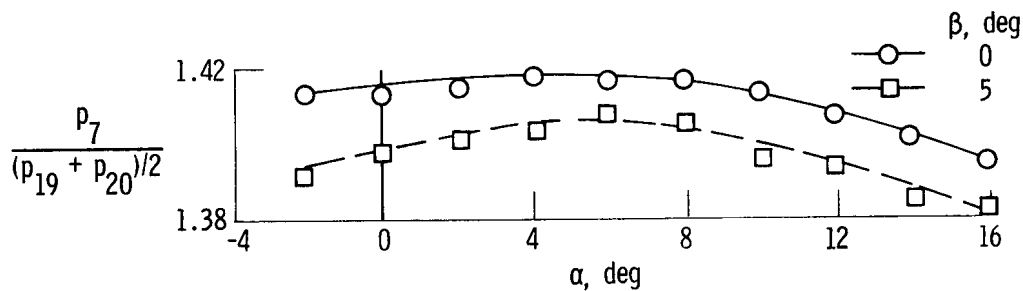




(a)  $M = 0.30$ .

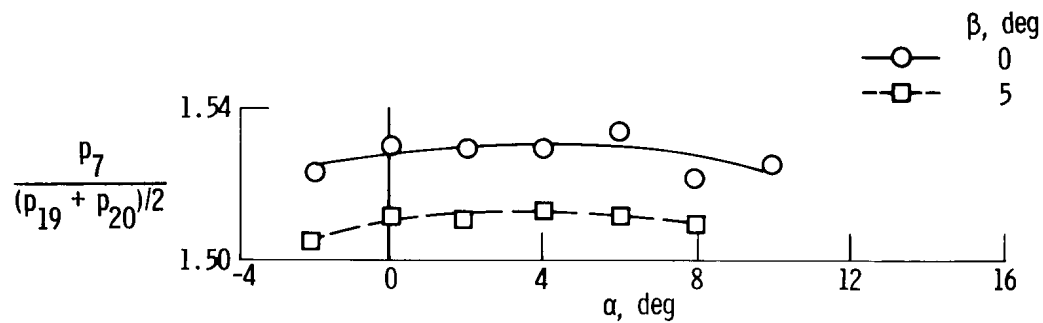


(b)  $M = 0.50$ .

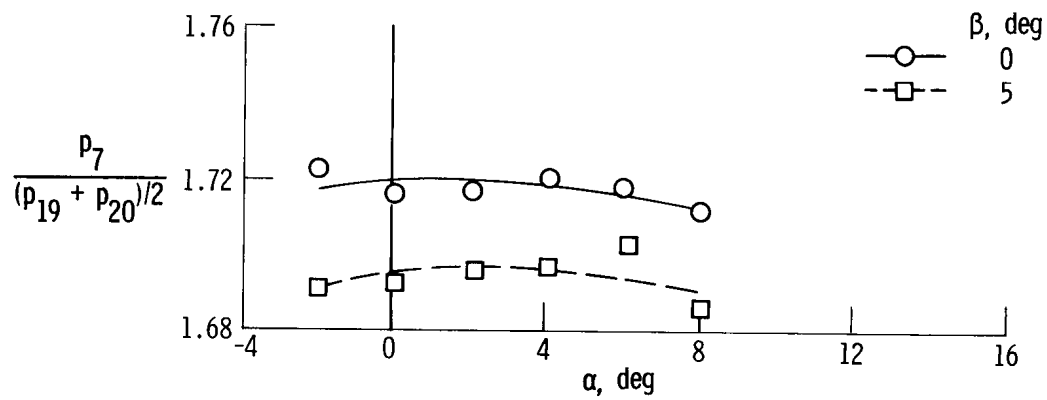


(c)  $M = 0.70$ .

Figure 27. Pressure ratio for determination of Mach number plotted against angle of attack using a combination of nose and fuselage orifices. Orifices 7, 19, and 20.

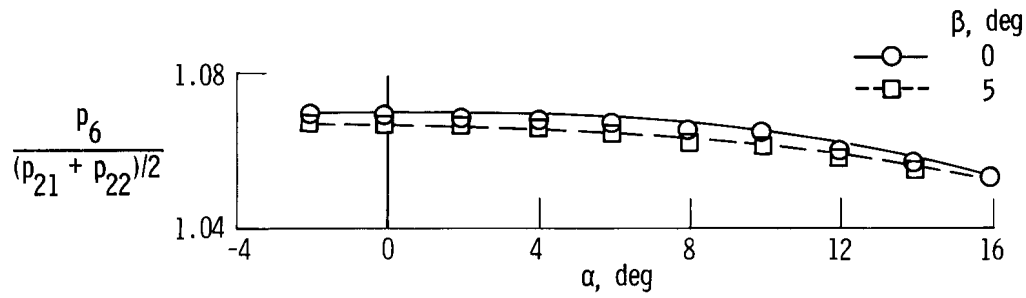


(d)  $M = 0.78$ .

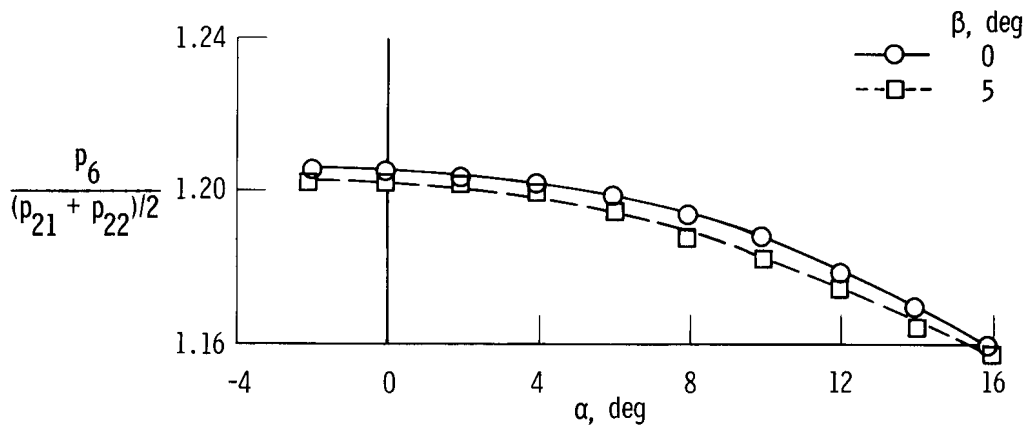


(e)  $M = 0.90$ .

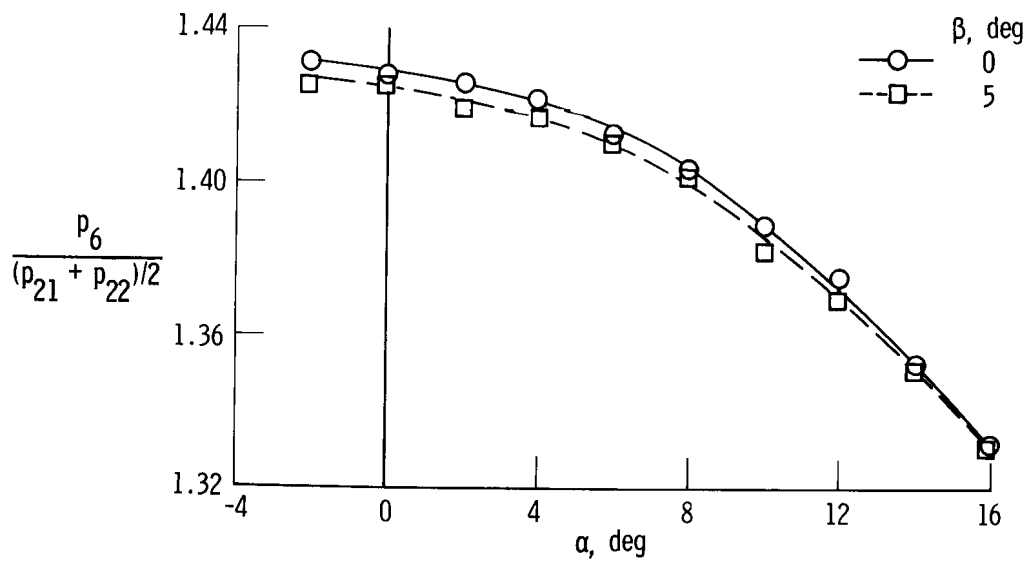
Figure 27. Concluded.



(a)  $M = 0.30$ .

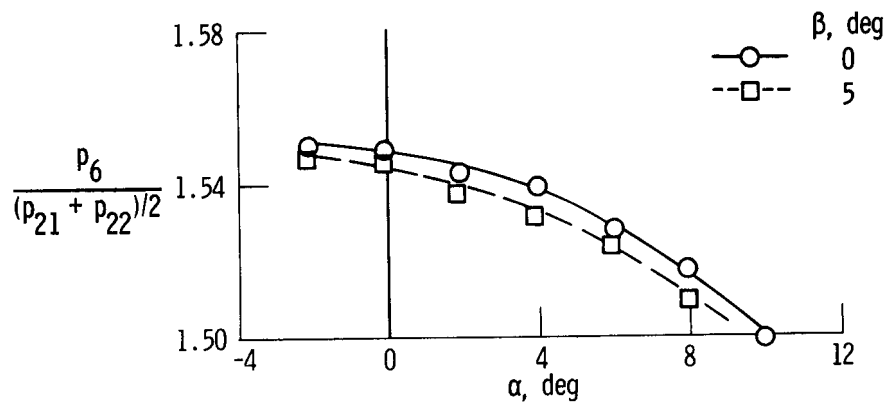


(b)  $M = 0.50$ .

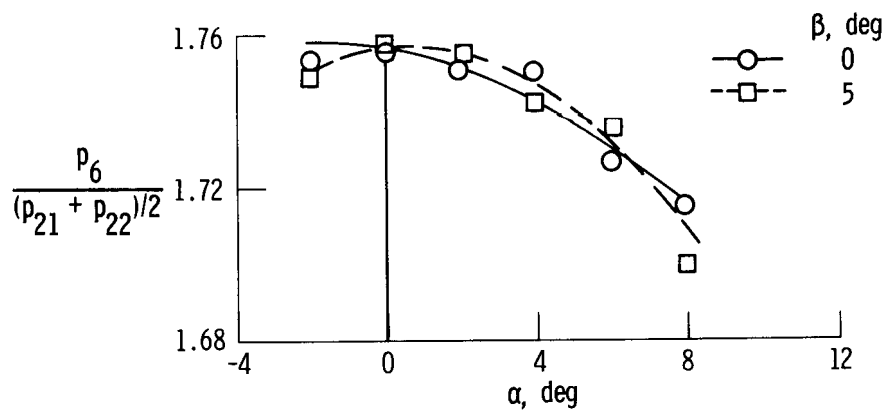


(c)  $M = 0.70$ .

Figure 28. Pressure ratio for determination of Mach number plotted against angle of attack using a combination of nose and fuselage orifices. Orifices 6, 21, and 22.

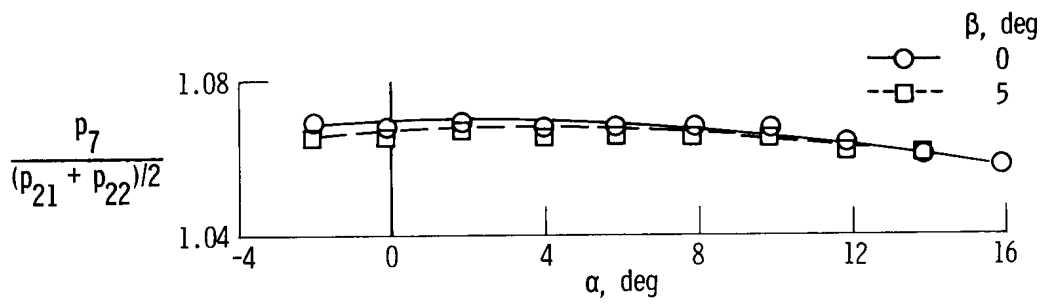


(d)  $M = 0.78$ .

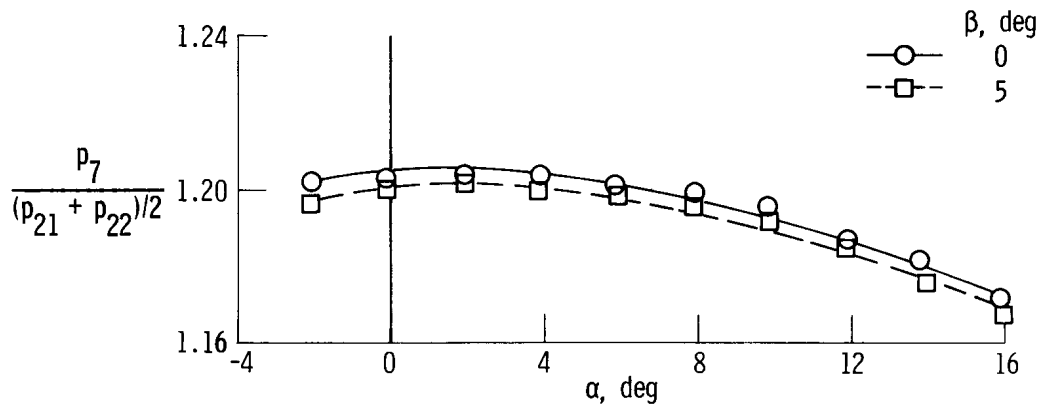


(e)  $M = 0.90$ .

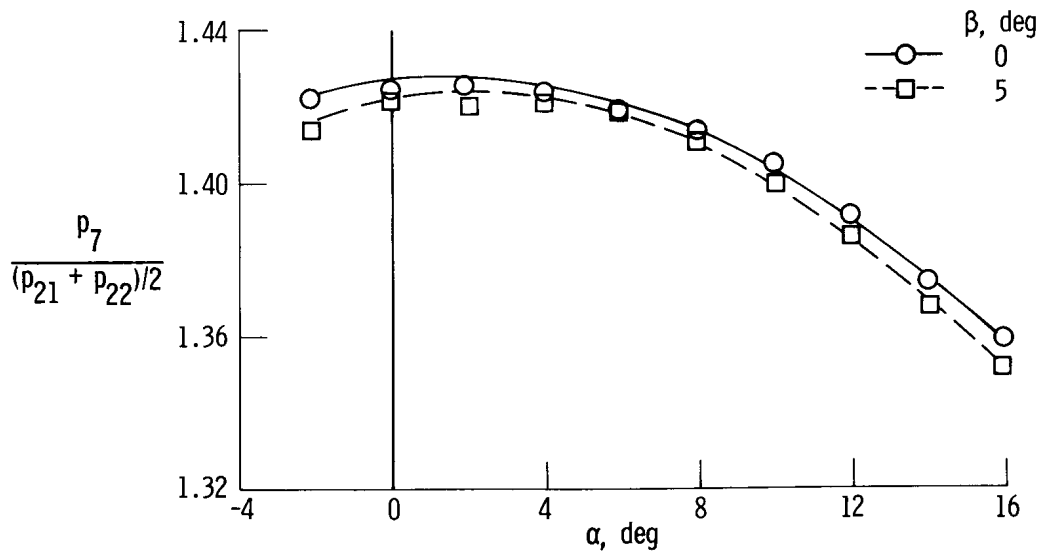
Figure 28. Concluded.



(a)  $M = 0.30$ .

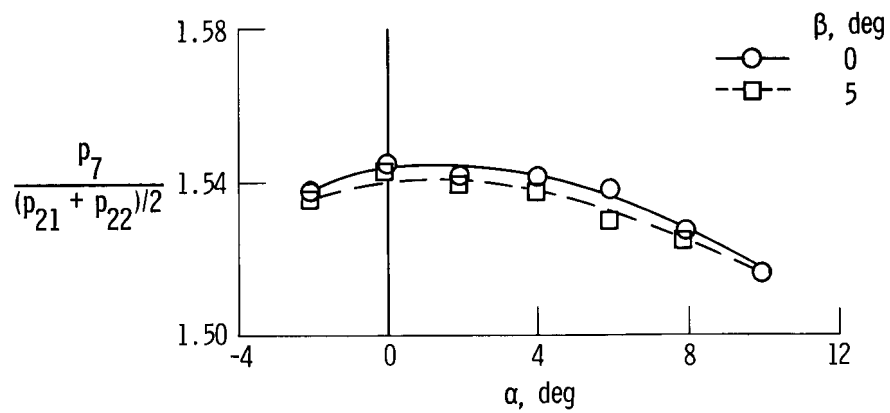


(b)  $M = 0.50$ .

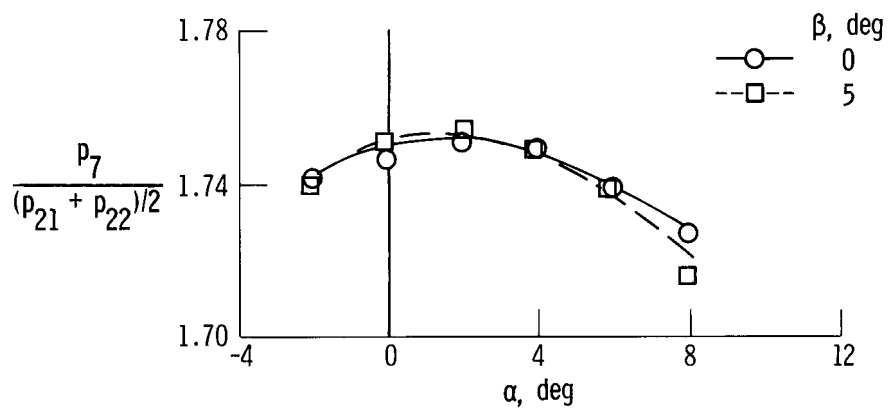


(c)  $M = 0.70$ .

Figure 29. Pressure ratio for determination of Mach number plotted against angle of attack using a combination of nose and fuselage orifices. Orifices 7, 21, and 22.

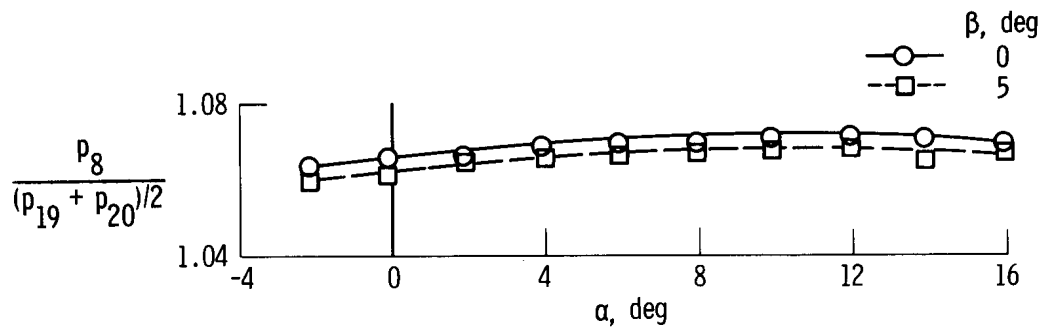


(d)  $M = 0.78$ .

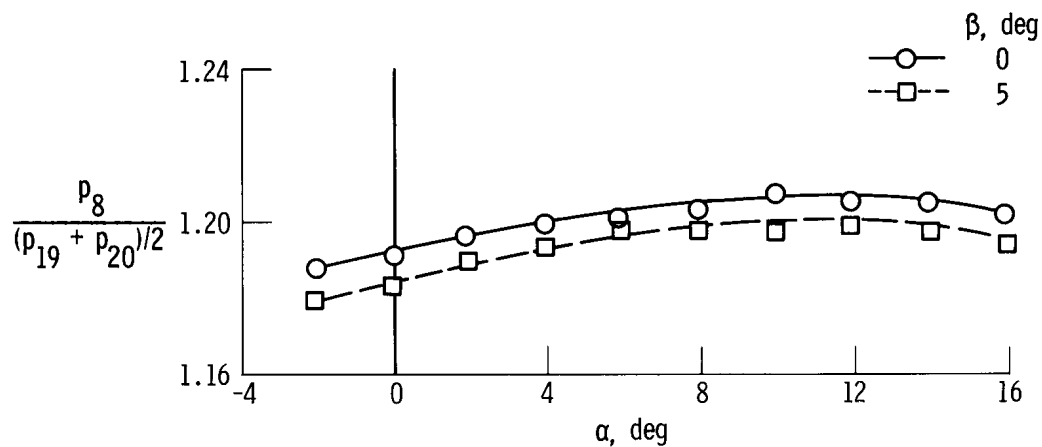


(e)  $M = 0.90$ .

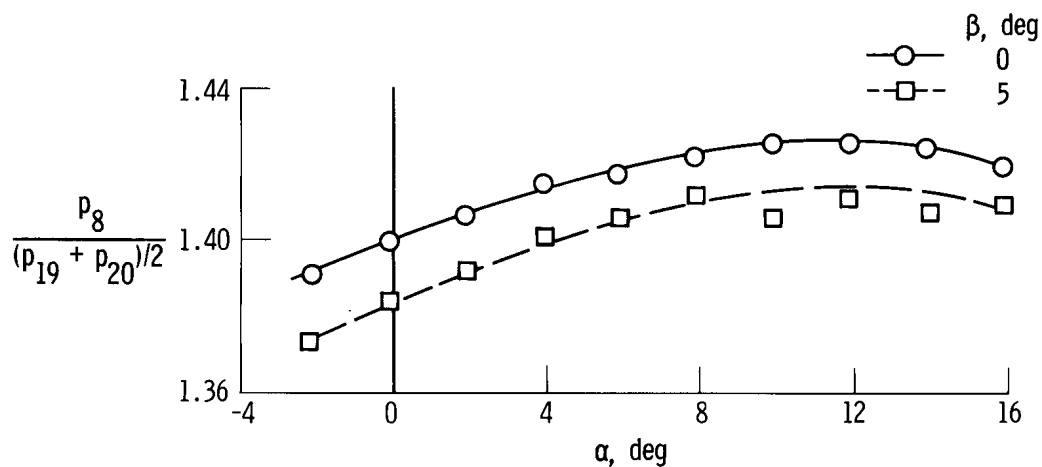
Figure 29. Concluded.



(a)  $M = 0.30$ .

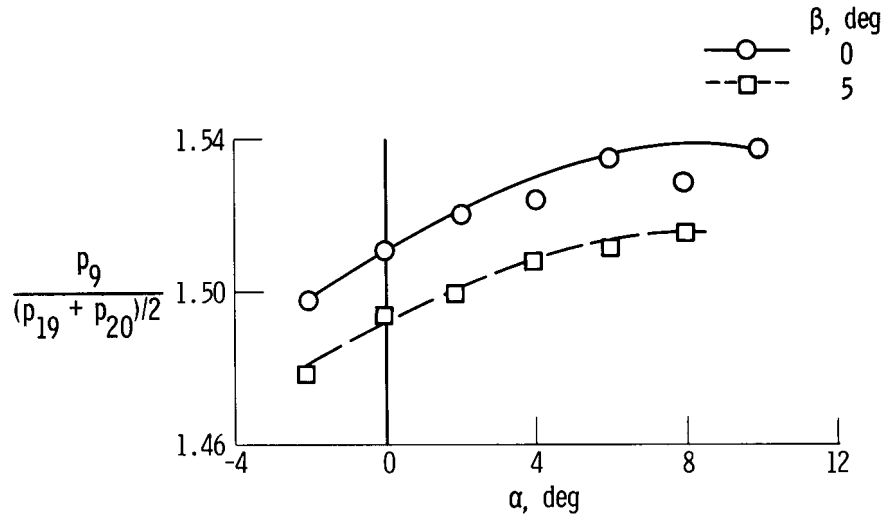


(b)  $M = 0.50$ .

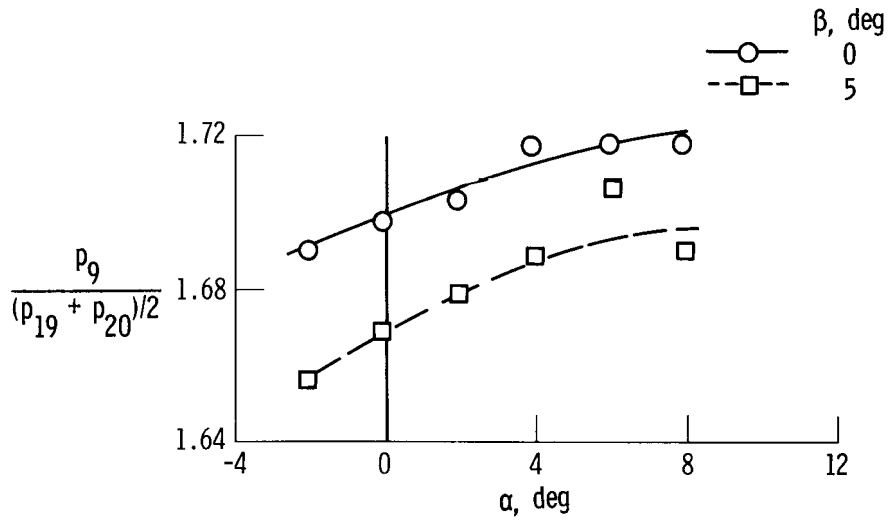


(c)  $M = 0.70$ .

Figure 30. Pressure ratio for determination of Mach number plotted against angle of attack using a combination of nose and fuselage orifices. Orifices 8, 19, and 22.



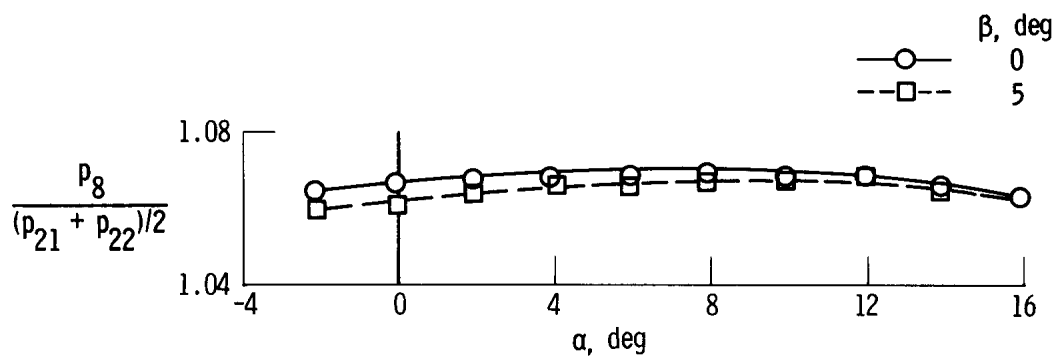
(d)  $M = 0.78$ .



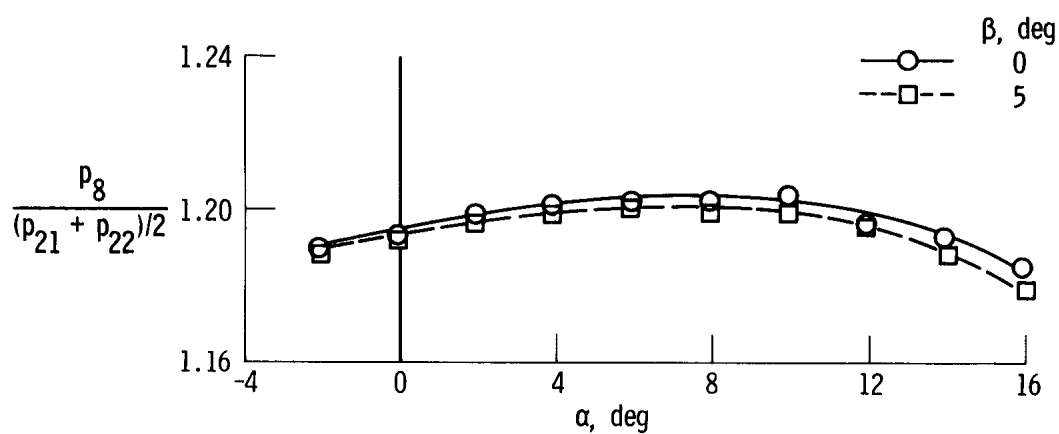
(e)  $M = 0.90$ .

Figure 30. Concluded.

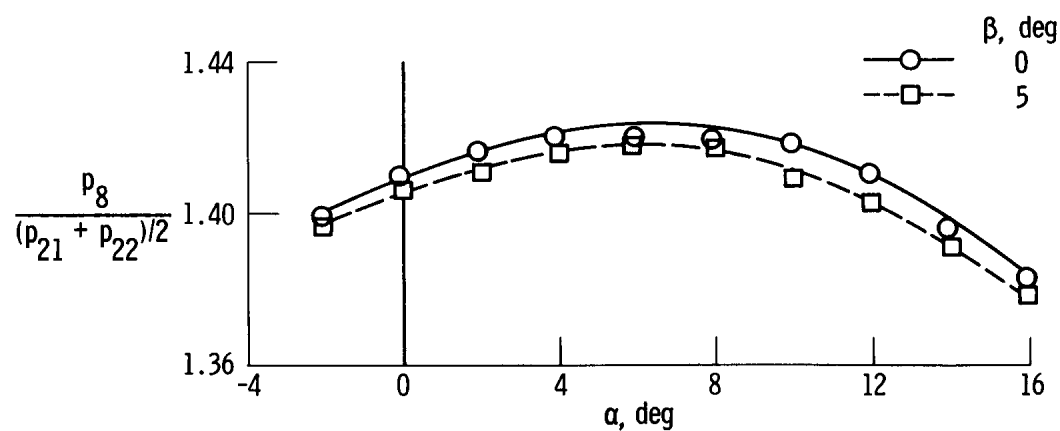




(a)  $M = 0.30$ .

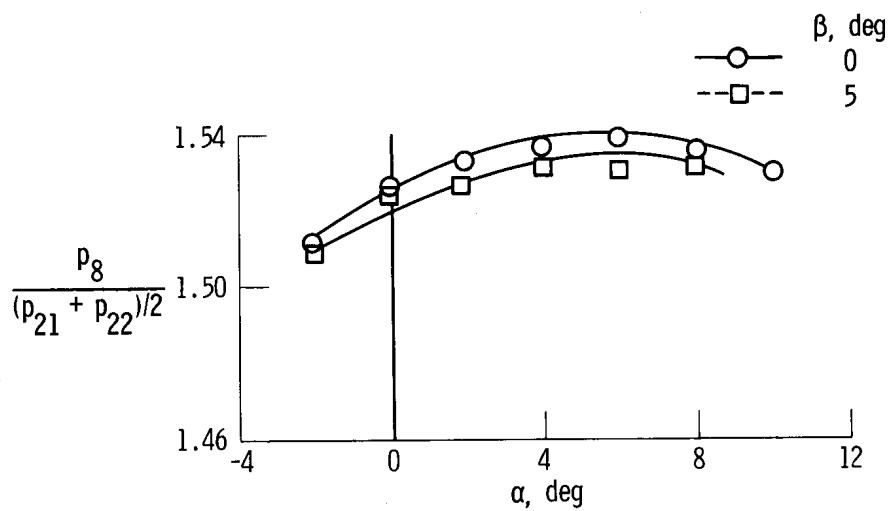


(b)  $M = 0.50$ .

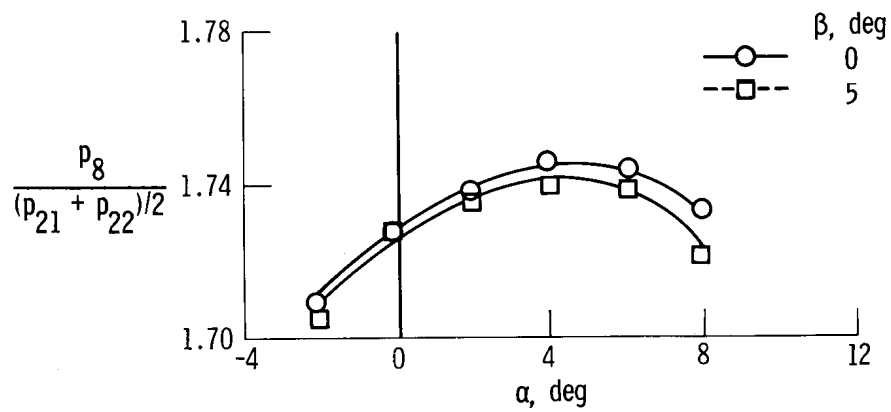


(c)  $M = 0.70$ .

Figure 31. Pressure ratio for determination of Mach number plotted against angle of attack using a combination of nose and fuselage orifices. Orifices 8, 21, and 22.

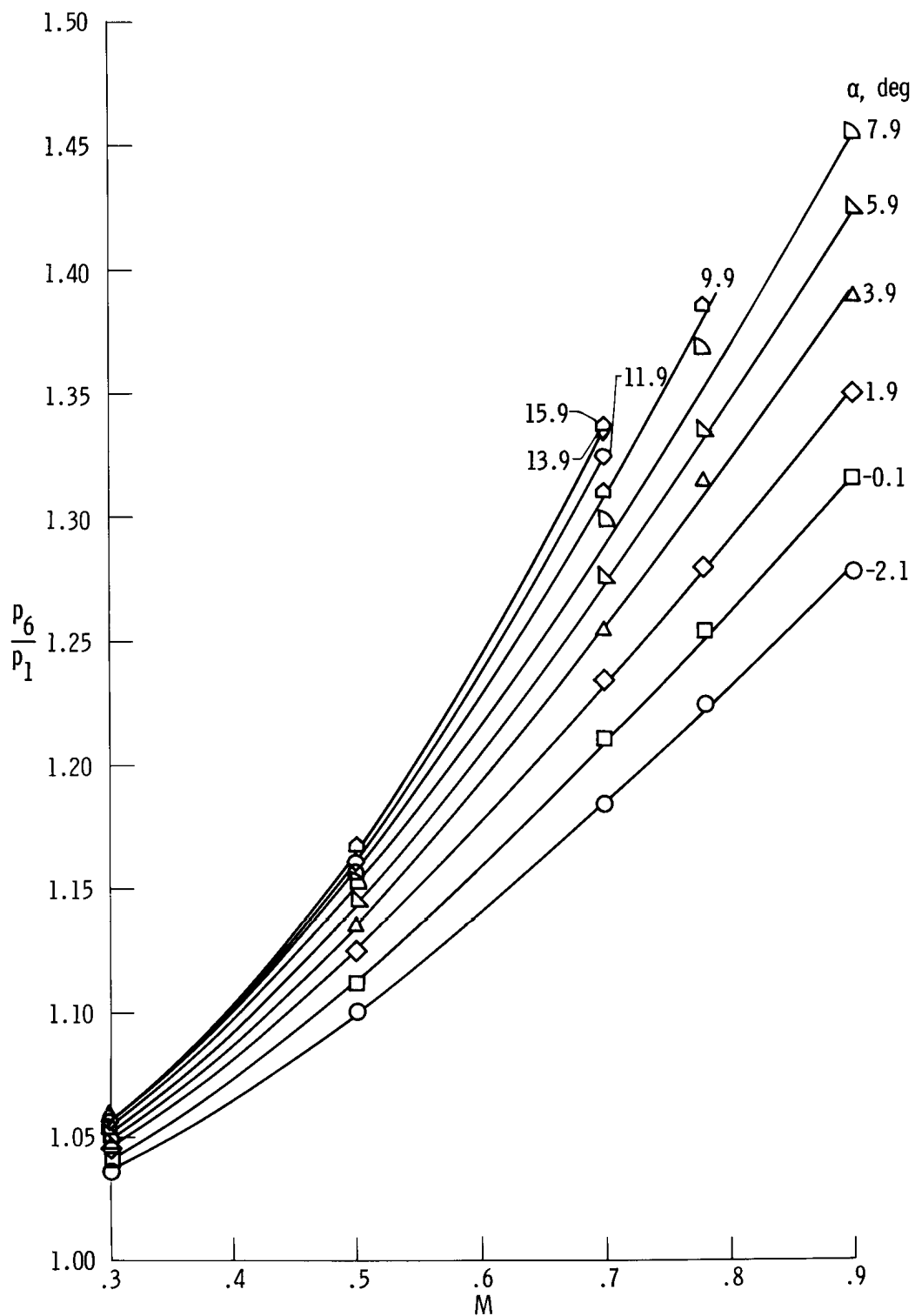


(d)  $M = 0.78$ .



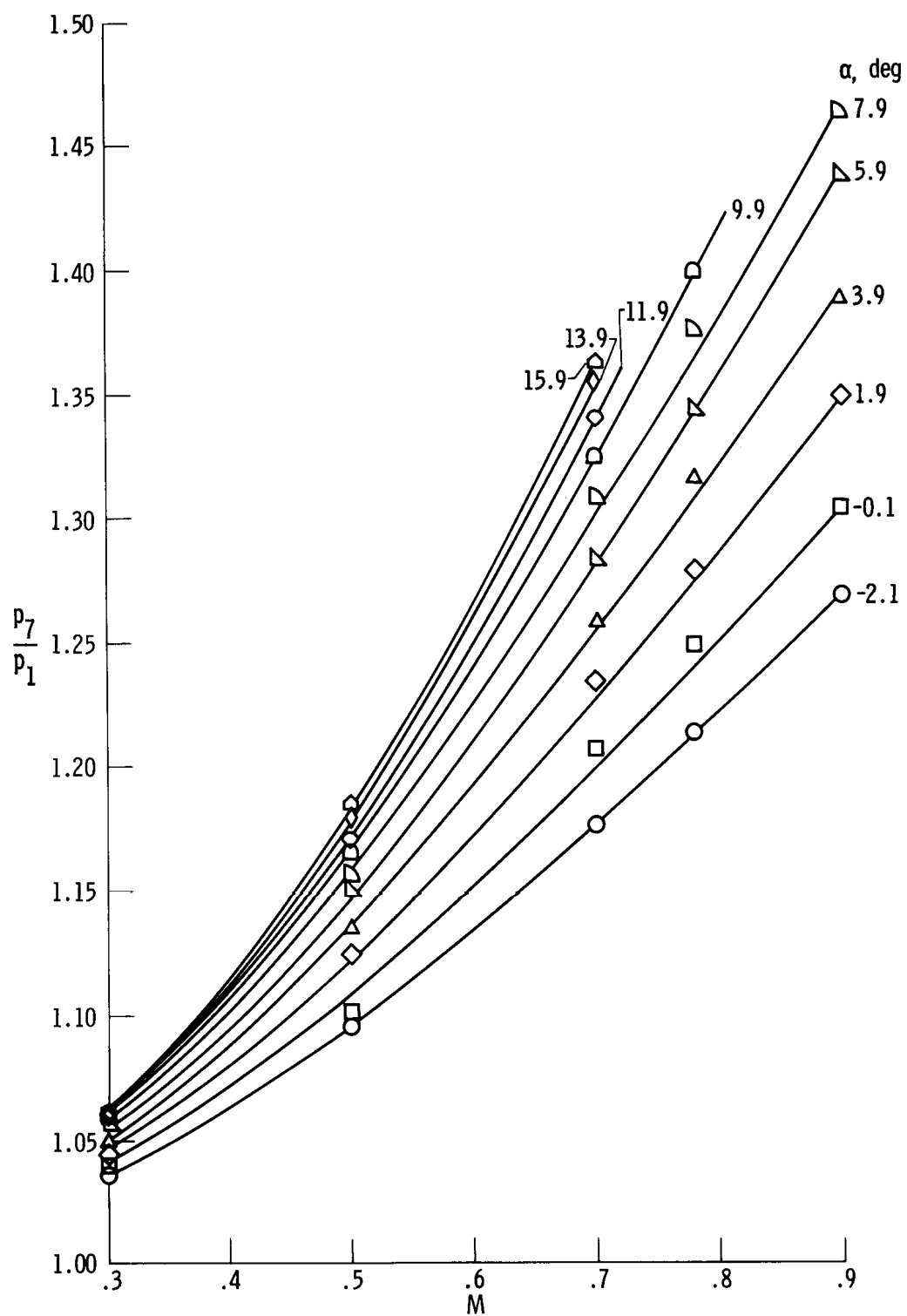
(e)  $M = 0.90$ .

Figure 31. Concluded.



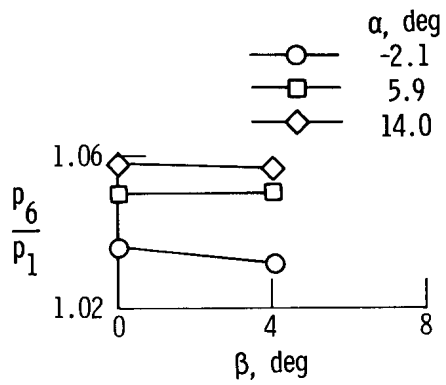
(a) Orifices 1 and 6.

Figure 32. Pressure ratio for determination of Mach number using only orifices on nose.  $\beta = 0^\circ$ .

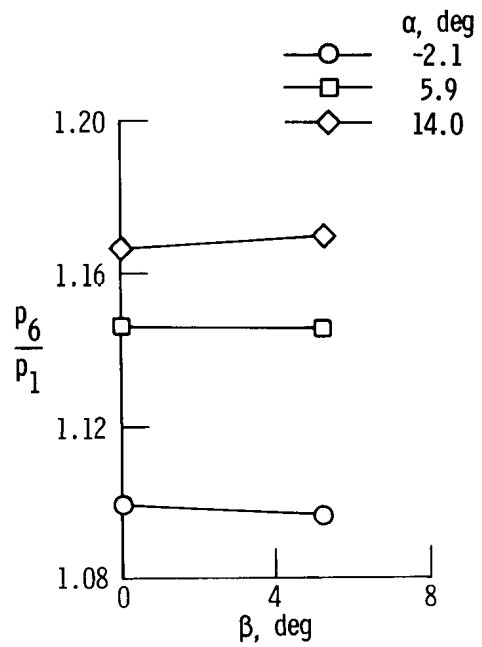


(b) Orifices 1 and 7.

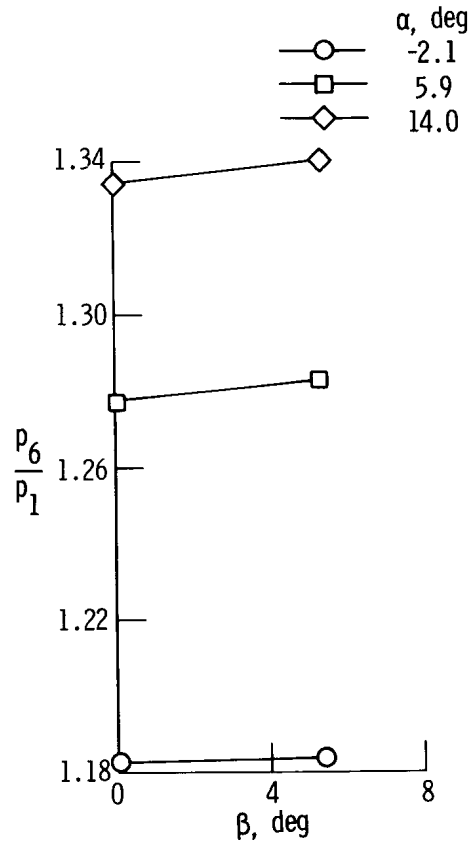
Figure 32. Concluded.



(a)  $M = 0.30$ .



(b)  $M = 0.50$ .



(c)  $M = 0.70$ .

Figure 33. Pressure ratio for determination of Mach number plotted against angle of sideslip. Orifices 1 and 6.

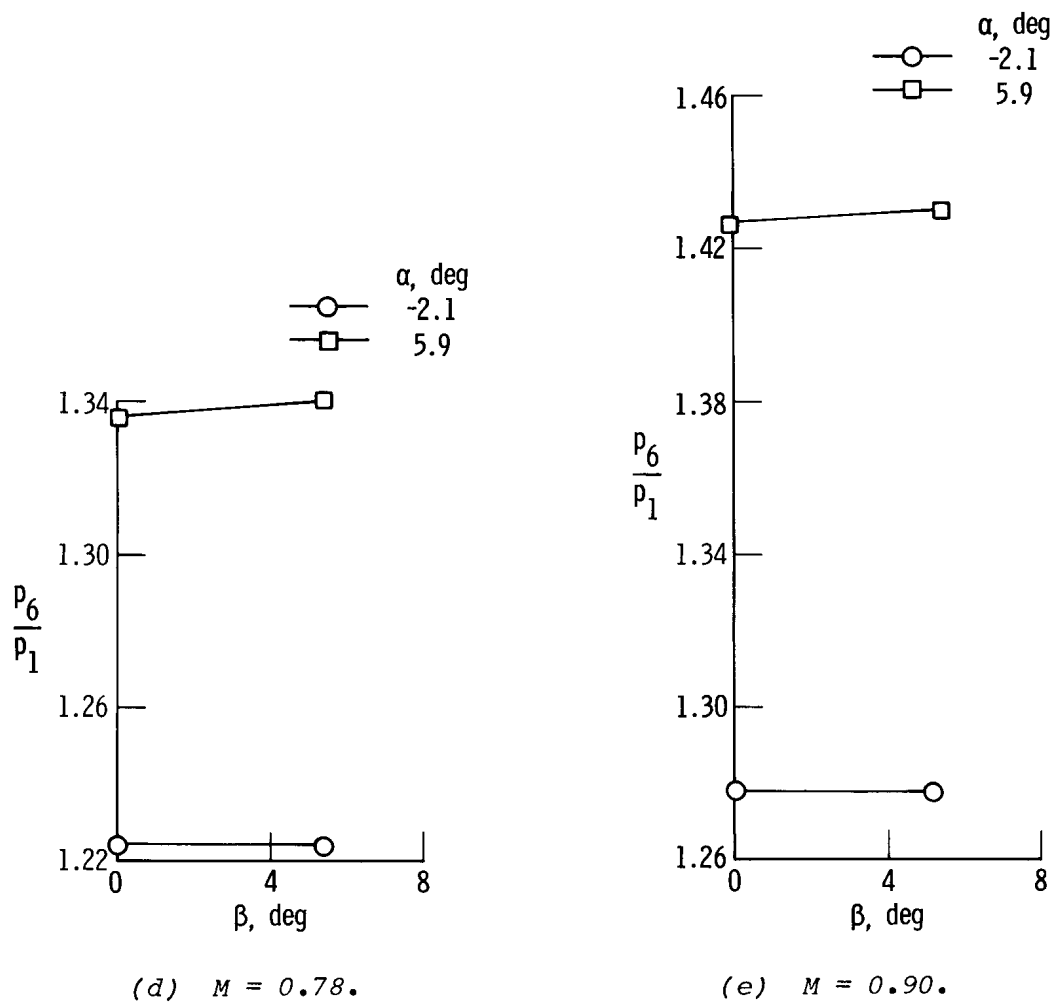
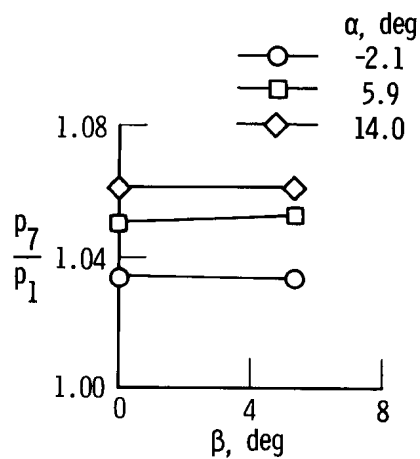
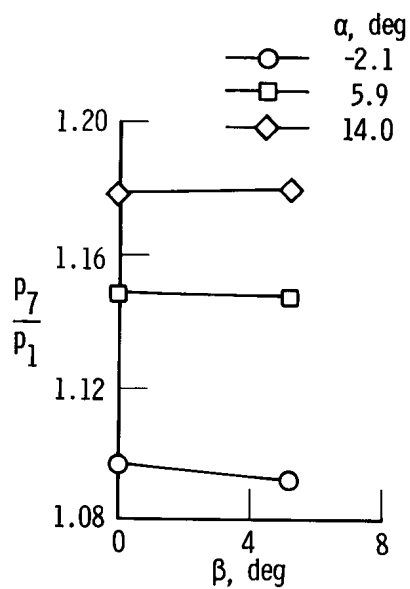


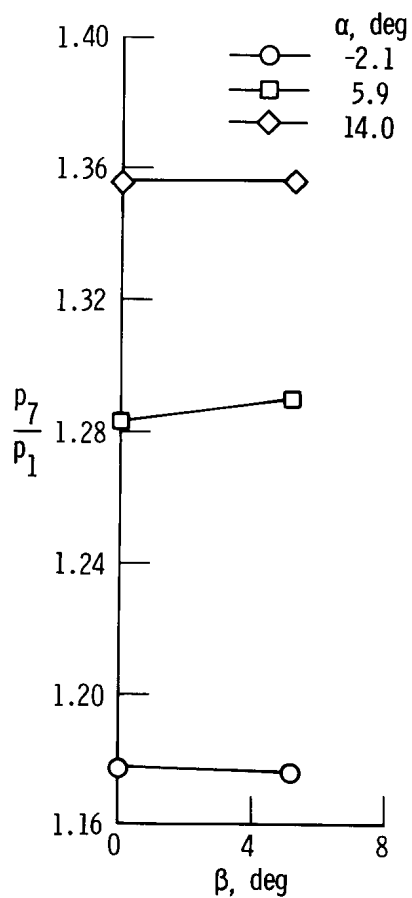
Figure 33. Concluded.



(a)  $M = 0.30$ .

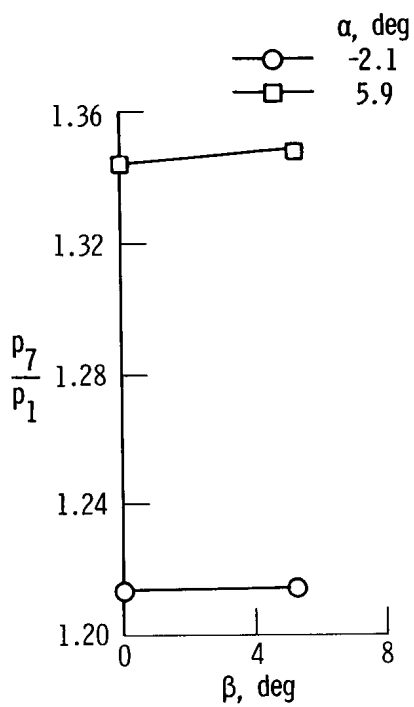


(b)  $M = 0.50$ .

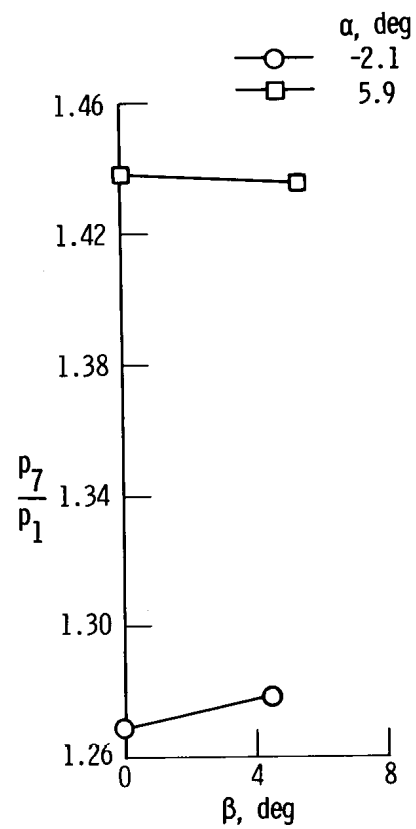


(c)  $M = 0.70$ .

Figure 34. Pressure ratio for determination of Mach number plotted against angle of sideslip. Orifices 1 and 7.



(d)  $M = 0.78$ .



(e)  $M = 0.90$ .

Figure 34. Concluded.



1. Report No. NASA TP-1642		2. Government Accession No.		3. Recipient's Catalog No.	
4. Title and Subtitle WIND TUNNEL INVESTIGATION OF AN ALL FLUSH ORIFICE AIR DATA SYSTEM FOR A LARGE SUBSONIC AIRCRAFT				5. Report Date May 1980	
				6. Performing Organization Code	
7. Author(s) Terry J. Larson, Stuart G. Flechner, and Paul M. Siemers III				8. Performing Organization Report No. H-1085	
				10. Work Unit No. 989-10-00	
9. Performing Organization Name and Address  Dryden Flight Research Center P.O. Box 273 Edwards, CA 93523				11. Contract or Grant No.	
				13. Type of Report and Period Covered Technical Paper	
12. Sponsoring Agency Name and Address National Aeronautics and Space Administration Washington, D.C. 20546				14. Sponsoring Agency Code	
15. Supplementary Notes Terry J. Larson: Dryden Flight Research Center Stuart G. Flechner and Paul M. Siemers III: Langley Research Center, Hampton, VA 23665					
16. Abstract  <p>The results of a wind tunnel investigation on an all flush orifice air data system for use on a KC-135A aircraft are presented. The investigation was performed to determine the applicability of fixed all flush orifice air data systems that use only aircraft surfaces for orifice installation to conventional subsonic aircraft. The tests covered a Mach number range of 0.30 to 0.90, an angle of attack range from -2° to 16°, and an angle of sideslip range from 0° to 5°.</p> <p>It was found that certain combinations of orifices on the nose of the model (in a configuration similar to that of the shuttle entry air data system) provided the measurements required for the determination of stagnation pressure, angle of attack, and angle of sideslip. For the measurement of static pressure, additional flush orifices in positions on the sides of the fuselage corresponding to those in a standard pitot-static system were required. An acceptable but less accurate system, consisting of orifices only on the nose of the model, is defined and discussed. The results of the investigation are believed to warrant the evaluation of the concept in flight with a full scale airplane.</p>					
17. Key Words (Suggested by Author(s))  Air data Airspeed and altitude measurements Flow angularity measurements			18. Distribution Statement  Unclassified - Unlimited   STAR category: 06		
19. Security Classif. (of this report) Unclassified		20. Security Classif. (of this page) Unclassified		21. No. of Pages 98	
				22. Price* \$6.00	

\*For sale by the National Technical Information Service, Springfield, Virginia 22161

NASA-Langley, 1980